Advanced Hybrid Solar Cell Approaches for Future Generation Ultra-High Efficiency Photovoltaic Devices

by

Jongwon Lee

A Dissertation Presented in Partial Fulfillment
of the Requirements for the Degree
Doctor of Philosophy

Approved April 2014 by the
Graduate Supervisory Committee:

Christiana Honsberg, Chair
Stuart Bowden
Ronald Roedel
Stephen Goodnick
Dieter Schroder

ARIZONA STATE UNIVERSITY

May 2014

ABSTRACT

Increasing the conversion efficiencies of photovoltaic (PV) cells beyond the single junction theoretical limit is the driving force behind much of third generation solar cell research. Over the last half century, the experimental conversion efficiency of both single junction and tandem solar cells has plateaued as manufacturers and researchers have optimized various materials and structures.

While existing materials and technologies have remarkably good conversion efficiencies, they are approaching their own limits. For example, tandem solar cells are currently well developed commercially but further improvements through increasing the number of junctions struggle with various issues related to material interfacial defects. Thus, there is a need for novel theoretical and experimental approaches leading to new third generation cell structures.

Multiple exciton generation (MEG) and intermediate band (IB) solar cells have been proposed as third generation alternatives and theoretical modeling suggests they can surpass the detailed balance efficiency limits of single junction and tandem solar cells. MEG or IB solar cell has a variety of advantages enabling the use of low bandgap materials. Integrating MEG and IB with other cell types to make novel solar cells (such as MEG with tandem, IB with tandem or MEG with IB) potentially offers improvements by employing multi-physics effects in one device.

This hybrid solar cell should improve the properties of conventional solar cells with a reduced number of junction, increased light-generated current and extended material selections. These multi-physics effects in hybrid solar cells can be achieved through the use of nanostructures taking advantage of the carrier confinement while using existing solar cell materials with excellent characteristics. This reduces the additional cost to develop novel materials and structures.

In this dissertation, the author develops thermodynamic models for several novel types of solar cells and uses these models to optimize and compare their properties to those of existing PV cells. The results demonstrate multiple advantages from combining MEG and IB technology with existing solar cell structures.

DEDICATION

To beloved my parents and a little sister

And, to my committee member Dr. Dieter Schroder.

I am grateful for the encouragement and understanding as well as support from my parents, sister and all of my friends. Especially, I am grateful to my parents and my sister, Whanbok Lee (Father), Jungsook Kwon (Mother) and Soojin Lee (Sister) for their love, encouragement, patience and sacrifice. I couldn’t have successively finished this long journey without them.

Furthermore, Dr. Dieter Schroder was my admirable committee member until my comprehensive examination. And, unfortunately, we have lost one of the greatest academic honor two years ago.

His energetic and straightforward activities showed me the best example what a professor should do in the university. His simple and clear directions gave me a manifest way that I will follow as a way of researcher.

Even though I was regret to finish my journey with him, I want to say “extremely thank you” to become my committee member for this dissertation.

ACKNOWLEDGMENTS

First of all, I would like to express my sincere gratitude to my advisor, Dr. Christiana B. Honsberg, for her support and guidance throughout my graduate studies at Arizona State University. I greatly benefited from her deep intuition and strong knowledge in the thermodynamic limit modeling for third generation photovoltaic devices and solar cell design. I also want to thank my PhD committee members, Dr. Stuart Bowden, Dr. Ronald Roedel and Dr. Stephen Goodnick, for agreeing to serve on my committee and for their time spent on my committee. Also, special thanks to Dr. Dieter Schroder, for his intuitive and great guidance and encouragement until my comprehensive examination. I am really regretted that I could not finish my journey with him. It was wonderful moments with him in Arizona State University.

I also would like to show my sincere gratitude to Dr. Kwangseok Seo in Seoul National University and Dr. Weongook Jeong in Sung Kyun Kwan University as my mentors and advisors. Without their deep and meaningful advices while I have struggled in U.S, I could not finish my journey.

I would like to show my sincere gratitude to Dr. Jaechan Lee and Dr. Kangmin Chung in Sung Kyun Kwan University who they have advised about study in US.

I would like to thank the graduate students and my friends who worked with me on my research projects and enjoyed life at Arizona State University; namely, Korean Brothers (Yeongho Kim (Hozzang), Jaewon Oh, Jaeyoung Choi, Sangpyung Kim, Jaewoong Chung, Junghoon Lee, Keebeom Kim, Jaehee Park, Sungchan Lim, Hanjoe Kim) and Younghoon Song who has been my best friend more than eight years in United States.

I also want to express my appreciation to all my colleagues in the Arizona State University Solar Power Laboratory for helpful conversations regarding research; especially to Mr. Bill Dauksher, Dr. Nikolai Faleev and Dr. Clarence Tracy. Furthermore, special thanks goes to the secretary of QESST, Michele Nobles, Regina Sanborn and Rebecca Davis for her kind help.

TABLE OF CONTENTS

Page

APPENDIX

LIST OF TABLES

Table Page

Table Page

LIST OF FIGURES

Figure Page

CHAPTER 1

INTRODUCTION

1.1 Solar Energy

The development of energy technologies is important to modernized societies with benefits that will improve quality of life for generations to come. After the mid-20th century, electric or power was considered a major gift to civilization. Until the early 21st century, fossil fuel and nuclear technologies were the leading energy sources to provide benefits to world. However, fossil fuels and nuclear power have major issues due to both a dwindling work force and leak potential for nuclear plants (magnified by the 2011 Fukushima Daiichi disaster) as well as a limited coal supply due to be depleted within the next 200 years plus the environmental contamination of carbon dioxide emissions and ash disposal practices of coal-fired power plants. Currently, solar energy is the most promising future generation energy resource because of it is clean and permanent. However, existing energy resources are still the dominant providers of electricity for both industrial and commercial purposes. Furthermore, energy consumption has been extensively increased due to the demands of diverse fields, which are deeply related to the industrial and economic status of countries worldwide. Thus, the implementation of nuclear energy has tremendously increased in that past 50 years. Practically, the energy consumption is expected to increase by 56% between 2010 and 2040. Fig. 1.1 shows world energy consumption going from 524 quadrillion British thermal units (Btu) in 2010 to 630 quadrillion Btu in 2030 and to 820 quadrillion Btu in 2040 [1]. Energy consumption from Non-Organization for Economic Co-operation and Development (OECD) nations is expected to dramatically increase after 2020 compared to OECD countries. Non-OECD countries are still developing their infrastructures and enhancing their novel technologies based on investments from the global companies in OECD countries. Thus, it may require more time and money to develop their countries.

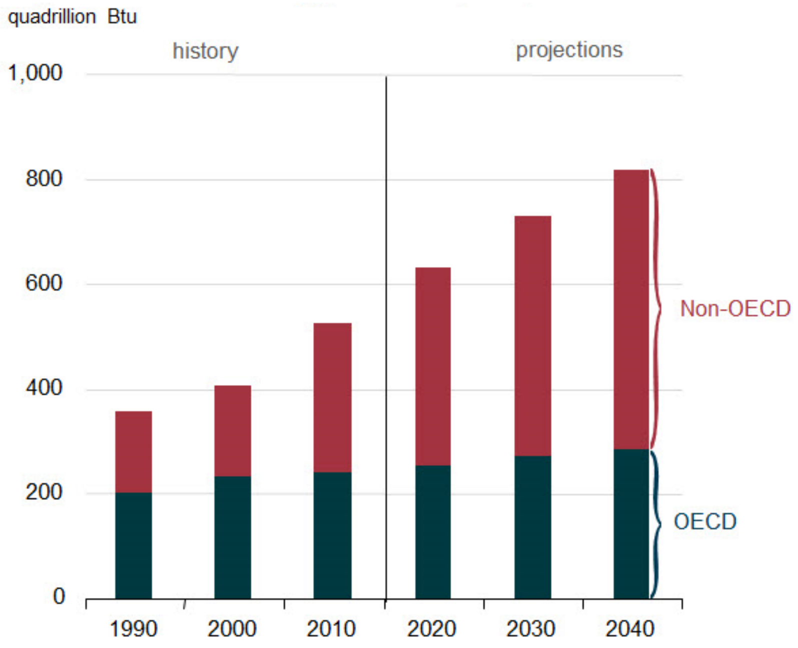

Fig.1.1. World energy consumption, 1990-2040, [U.S. Energy Information Administration ,July 2013] [1] (see Appendix. A)

In other words, even though energy consumption will increase more than 50% in the future, it is still dependent on the oil and nuclear power to maintain their facilities [1]. Due to limited usages and environmental contamination from both coal and nuclear plants, utilization of these sources should decrease as in favor of renewable alternatives. According to the “Annual Energy Outlook 2013 with Projections to 2040,” Executive Summary: “Electricity generation from solar and, to a lesser extent, wind energy sources grows as their costs decline, making them more economical in the later years of the projection.” [U.S. Energy Information Administration, July 2013] [2].

Even if the future of solar energy is bright, the lack of solar energy infrastructure and cost of installation hinders development. Even though the solar cell is popular energy resource, electricity suppliers are still focused on providing solar cells based on income analysis and regional differences. In other words, solar energy use is still restricted for the most part to individuals who can afford solar cells.

Therefore, to satisfy rapidly increasing demands for green energy and to relieve the problems of economic status, an urgent need exists to increase the efficiency and reduce the cost of electricity (COE) in $/kWh [3],[4]. But, solar energy still shows relatively high COE compared to the existing energy sources so that increasing the conversion efficiency is a key to reducing COE of photovoltaic (PV) devices. Furthermore, the national energy policies should also support an increase in the general use of solar energy.

Even though researchers are focused on increasing the conversion efficiency of PV devices by investigating semiconductor materials from periodic table of the element such as silicon, group III-V and group II-V, existing methods like thin-film solar cells or tandem solar cells are going to meet limitations due to their own material properties.

For instance, the II-VI material-based thin film solar cell shows about 10% range of conversion efficiency due to organic material properties. Tandem solar cells present the greatest improvement of solar cell efficiency, but their material properties are problematic due to the need for increasing the number of carriers.

To overcome these issues, new or innovative concepts are still needed to enhance PV conversion efficiency by both theoretical and experimental approaches. In Fig. 1.2, the wafer and thin film based first and second generation solar cells display high cost and low conversion efficiency [4]. But, third generation solar cells like tandem, multiple exciton generation, hot carrier, and intermediate band solar cells can reduce cost and increase efficiency (see Fig. 1.2) [4].

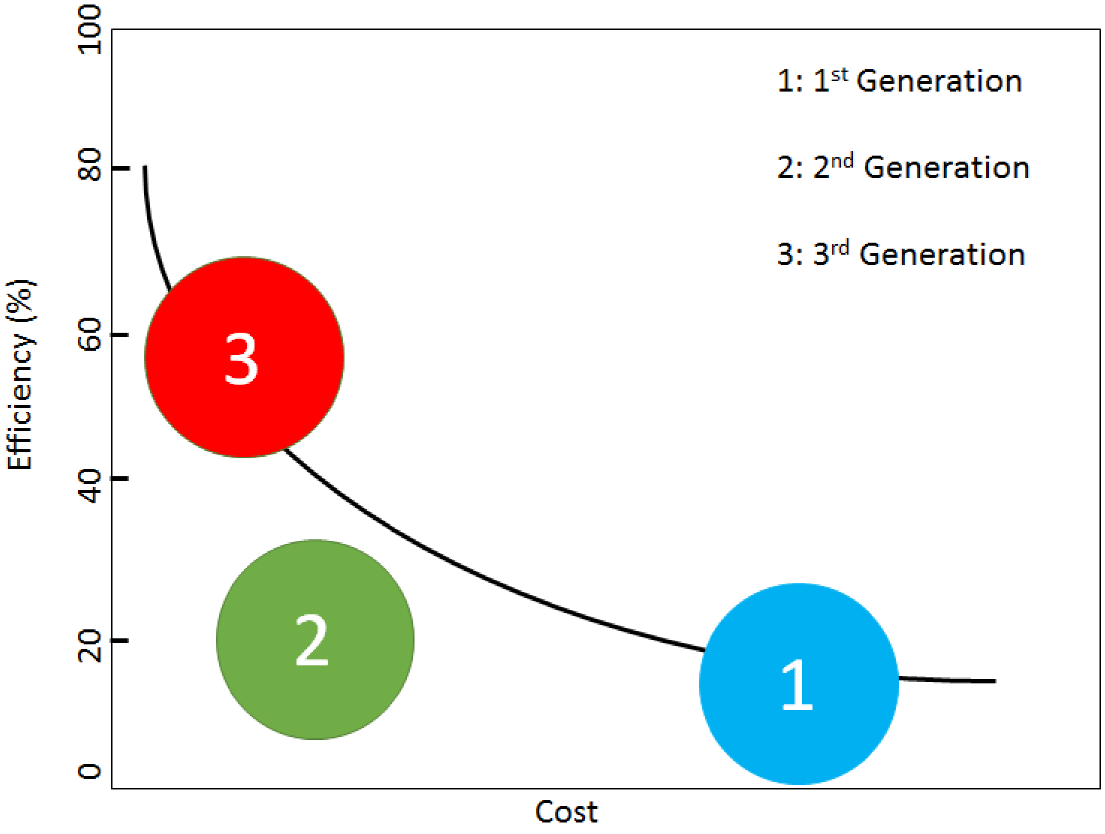

Fig 1.2. Efficiency vs cost of 1st, 2nd, and 3rd generation solar cells [4].

In Fig. 1.3, the current efficiency records of solar cells have dramatically increased to the point that tandem solar cells are leading PV devices with concentrators to achieve 50% conversion efficiency [5],[6]. Further, the single junction silicon PV, Heterojunction with Intrinsic Thin-layer and GaAs-based III-V solar cell are also approaching 30% conversion efficiency [5],[6].

In Fig. 1.2, 30% of single junction solar cells' efficiencies are the range of first and second generation PV devices, which show high COE. Even if the efficiency of tandem solar cells display the range of third generation PV devices, it has to increase the number of junctions or stacks to enhance efficiency, and it has shown some drawbacks such as material defects between layers and cost effectiveness.

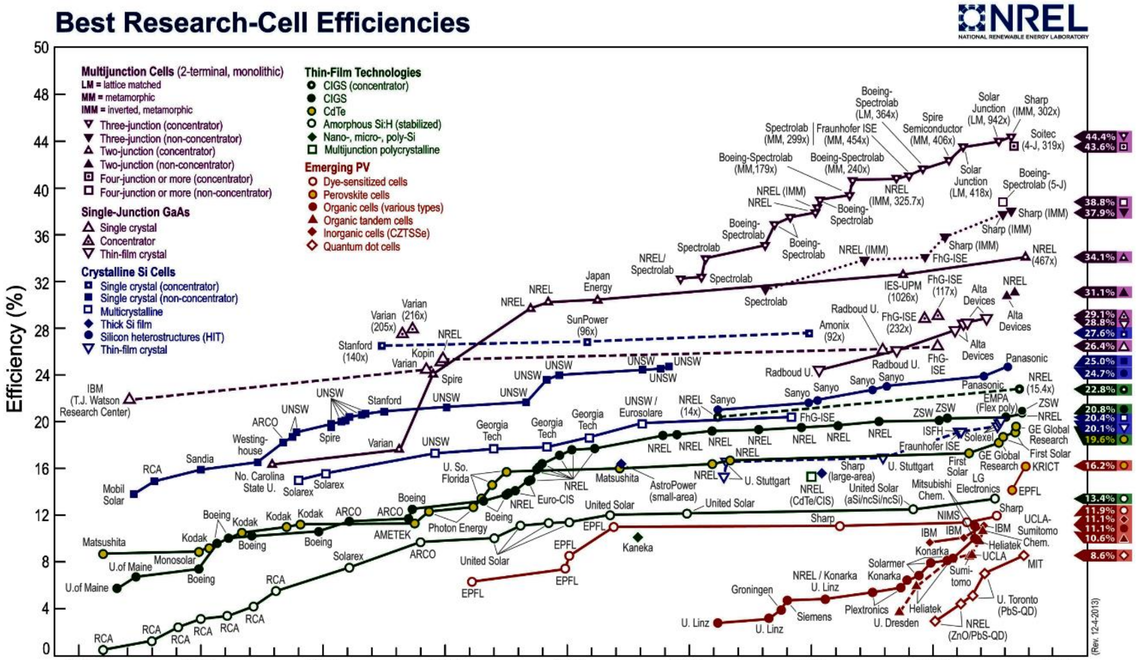

Fig. 1.3. Solar cell efficiency chart from 1975 to 2013 [National Renewable Energy Laboratory (NREL), Golden, CO., 2013] [5] (see Appendix A)

1.2 The Current Issues for Solar Cells for Future Generation PV

Among the renewable energy resources, solar energy is expanding as a popular energy alternative to replace existing energy sources. Using solar cells or PV devices is an eco-friendly way to generate electrical power without any pollution since solar energy is directly converted into electricity. The solar energy operation principle is the same as the theory of p-n junction diode wherein the excitation source is the Sun instead of temperature or electrical bias. Fig.1.4 provides information of solar cell operation wherein once photons from the Sun enter a solar cell, there is an electron and hole pair generation at the emitter. A hole flows through the front contact, and an electron travels into the base [7].

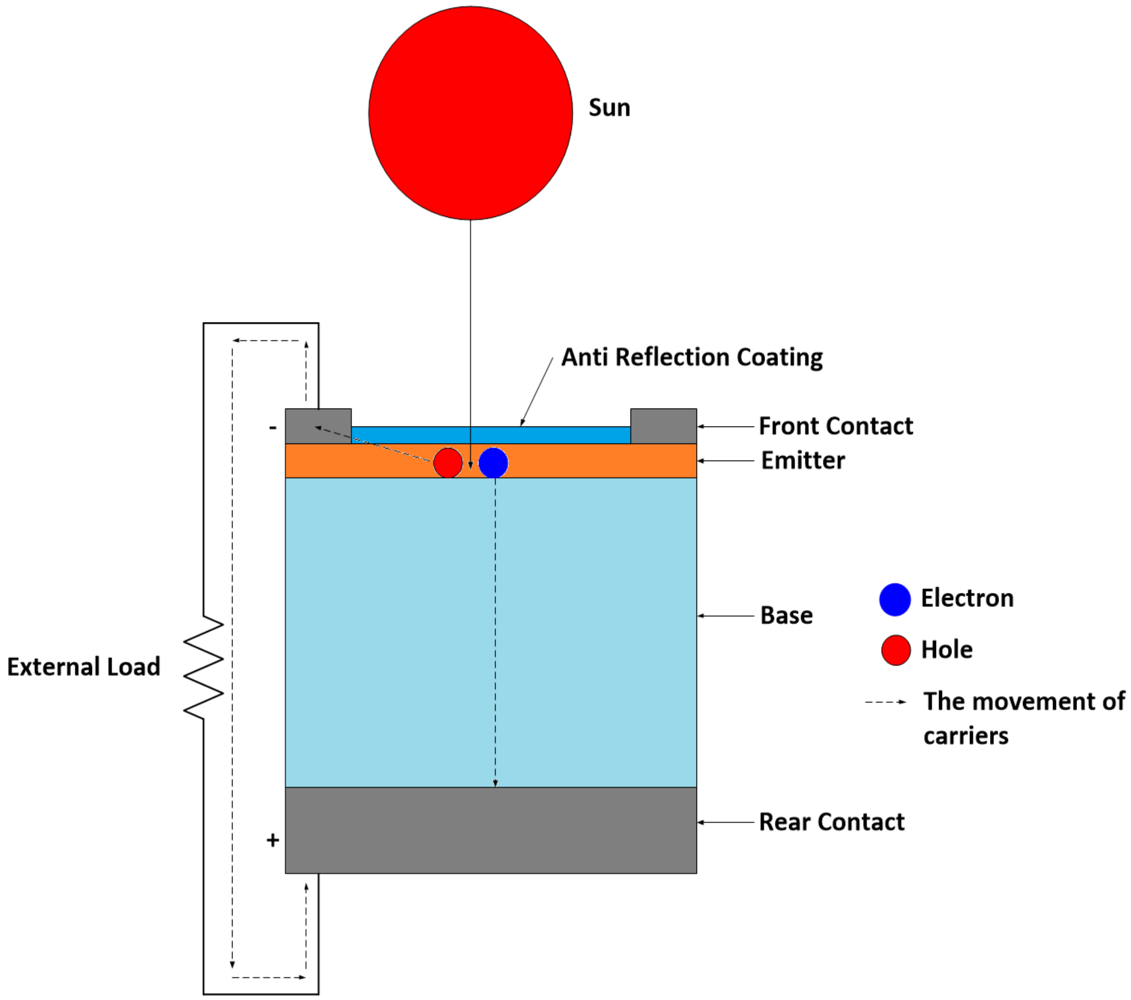

Fig. 1.4. The operation of a solar cell [7]

As carriers traverse the devices, they can experience losses of solar cells such as (1) thermalization loss, (2) recombination loss, (3) photon energy loss and (4) contact losses [4]. Typically, (2) and (4) are process dependent parameters that can be experimentally reduced. However, the theoretical approach of resolving (1) and (3) is necessary for third generation PV devices. For instance, the thermalization of hot carriers at a conduction band is the dominant loss in the PV devices that can be reduced by multiple EHPs of single junction solar cells. Furthermore, (3) can be managed by splitting solar spectrum through tandem and intermediate band solar cells.

The recent records of solar cells in Fig 1.3 have indicated that the existing technologies will approach its material induced limit. For example, the recent world records for using the most single junction solar cells indicate that UNSW reported using about 25% Si solar cells and Alta Devices claimed using 28.2% AlGaAs/GaAs cascade materials [5],[6],[8],[9]. And, the current report of thin-film amorphous silicon solar cells has indicated 25.6%. [10]. These records have approached to the ideal single junction limit as 31%.

Tandem solar cells are well-commercialized PV devices due to high conversion efficiency with light-concentrators. Current world records of tandem solar cells have been presented at 3J and 4J junction tandem solar cells. In a triple junction tandem solar cells, InGaAs (=1.00 eV)/GaAs (=1.42 eV)/InGaP (=1.89 eV) inverted metamorphic growth show 44.4% at 302 suns [6]. It is also shown 44.7% of four junction tandem solar cells from Fraunhofer ISE, Soitec, CEA-Leti and Helmholtz Center Berlin. This approach is composed of a wafer bonding structure with two dual junctions which its material composition is (InGaP(1.89 eV)/ GaAs (1.42 eV)// InGaAsP (1.05 eV) / InGaAs (0.73eV), 297 Suns) [11]. But, its theoretical efficiencies from the detailed balance limit indicate 54.8% of 3J, and 59.4% of 4J from the same configurations. There is also more than 10% difference between theoretical and experimental efficiencies so that it is still necessary further developments to improve the entire properties of tandem solar cells.

The clear ways to enhance tandem solar cells are increasing the number of junctions and develop its corresponding materials. But, the current methods can face to approach to the theoretical limit of tandem solar cells due to defect issues.

1.3 Thermodynamic Approaches for Nanostructured Solar Cells

The thermodynamics limit or detailed balance limit of solar cells are the general test bed for developing new concepts for PV cells. Since Shockley and Queisser (SQ) developed the detailed balance of single junction in 1961 [12], it has been strong tools to expect the theoretical limit of proposed solar cells.

In section 1.2, the author discusses the large difference between theoretical limit and experimental results of solar cells because of excluding non-radiative recombination in the detailed balance limits. Further, solar cells have their own material induced limits, for instance, silicon is an indirect bandgap materials in which there is an indirect transition. To suppress these properties, making nanostructured solar cells is a good candidate because of excellent quantum confinement and relaxed momentum conservation. And, nanostructured solar cells have a good light-control for better absorption.

There are many proposed types of third generation PV cells such as multiple exciton generation (MEG) solar cells from many electron and hole pairs per one incoming photon, intermediate band solar cell (IBSC) by three carrier transitions and hot carrier solar cells.

In the 1990s, various concepts such as multiple exciton generation (MEG) and intermediate band solar cells (IBSC) were proposed and their limiting efficiencies were also calculated to surpass the SQ limits.

MEG is a carrier multiplication solar cell per an incoming photon by impact ionization. Werner reported the limiting efficiencies of multiple exciton generation that its theoretical limit under one sun is about 45%after finding 130% of quantum efficiency in silicon and its optimum bandgaps are lowered about 0.7 eV [13], [14]. Luque and Marti proposed IBSC in 1997 and its theoretical limit is about 63% that it is similar to triple junction tandem solar cells, and active research using quantum dots of III-V materials is still being conducted in many groups with current reports about efficiencies around 20% [15],[16]. Tandem solar cells are the well-known commercialized PV cells with stacked different bandgap materials, and current reports shows over 40% utilization with concentrators [5],[6].

1.4 Motivation for Hybrid Approaches

Theoretical approaches for nanostructured solar cells have provided great impact to developing novel types of solar cells to achieve more than 50% conversion efficiency for future generations solar cells.

As described in previous sections, continual improvements in efficiency are necessary to achieve approaches in which the levelized electricity cost is low. Nanostructured approaches and advanced concept approaches have been long suggested as a means of realizing efficiencies above the SQ limit. However, nanostructures and advanced concept approaches have not achieved an improvement in efficiency, due to a combination of the fundamental concepts themselves, as well as the materials suggested for their implementation. For example, the conventional intermediate band approach has a lower theoretical efficiency that a four junction tandem, which has already been experimentally realized. Similarly, MEG approaches often utilize low band gaps and materials which have not a commercial or high efficiency experimental base. Moreover, MEG approaches, unless they use unrealistic concentration levels, and highly idealized assumptions, also have theoretical efficiencies below approaches already implemented. Thus, the overarching motivation of the thesis is to overcome these limits, primarily by developing hybrid approaches, which allow known materials to approach thermodynamic limits. In addition, for the special case of silicon, the thesis shows that the inclusion of MEG processes can realize high efficiencies.

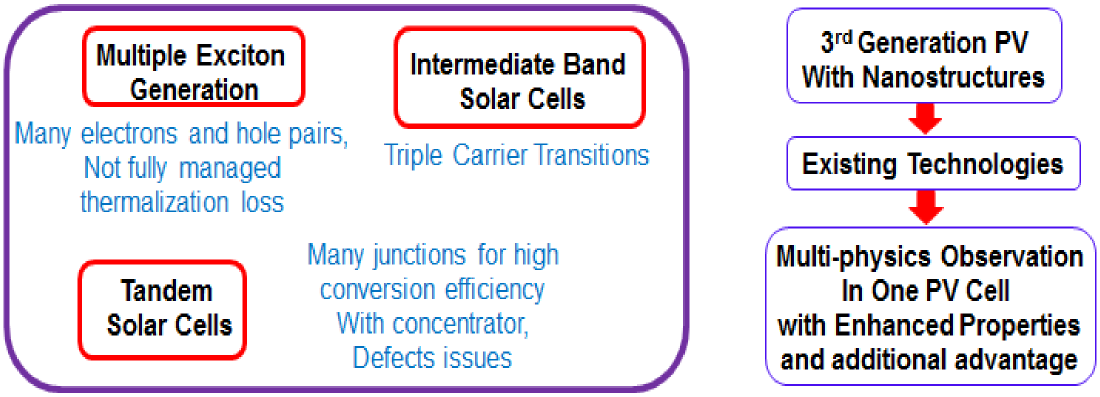

(a) The properties of solar cells

(b) Hybrid Approaches

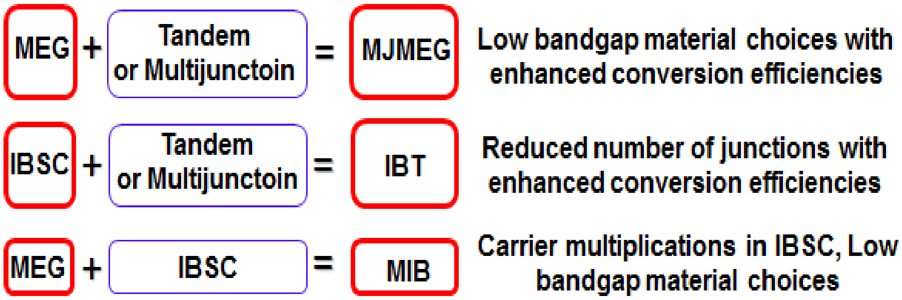

(c) Benefits of Hybrid Approaches Solar Cells

Fig.1.5. The proposed hybrid solar cells: (a) The properties of solar cells (b) Hybrid Approaches and (c) is the advantages of hybrid solar cells.

For instance, (1) combining with MEG with multijunction solar cells offers the improved conversion efficiency with low bandgap material choices, (2) integrating IBSC with tandem solar cells provides the increased theoretical conversion efficiency with reduced number of junctions and (3) carrier multiplication effect in IBSC give an advantage of material choices at low bandgap region with improved theoretical efficiency.

It is summarized in Fig 1.5 that describes (1) the properties of MEG, IBSC and tandem solar cells, (2) the combination procedures of existing technologies with 3rd generations PV of nanostructures and (3) the advantages of three proposed hybrid solar cells.

Moreover, other benefits of hybrid solar cells in thermodynamics have provided the wide selections of materials. For example, because of MEG effect of each junctions in tandem solar cells or intermediate band solar cells, the overall optimum bandgaps have reduced while comparing the existing optimum materials. And, intermediate band and tandem hybrid approaches make it possible to choose from group IV, III-V and II-V combinations.

1.5 Dissertation Outline

In this dissertation, the author proposes the hybrid concept solar cell with a combination of third generation photovoltaic cell theory to search the multi-points of benefits. The general sequence of each proposed concept is calculated by combining its detailed balance theory and investigating appropriate materials.

In Fig.1.6, process flows are presented to introduce the hybrid solar cells. The first two models are the detailed balance limit of tandem solar cells with multiple exciton generation solar cell (see Fig.1.6 (a)) and intermediate band solar cells (see Fig.1.6 (b)) to improve the characteristics of tandem or multijunction solar cells. And, the last model is the thermodynamic model of carrier multiplications of intermediate band solar cell (see Fig.1.6 (c)).

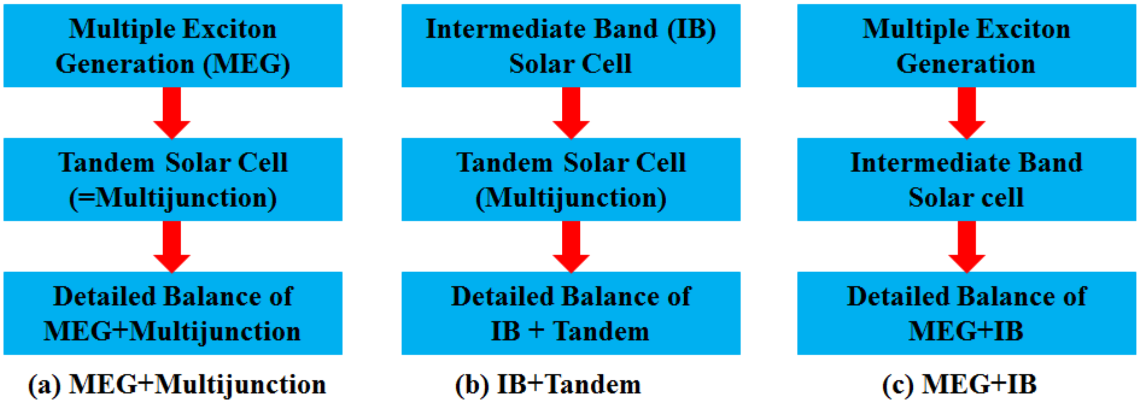

Fig. 1.6. The development of hybrid concepts of solar cells using detailed balanceshows: (a) MEG and multijunction-tandem hybrid solar cells, (b) the intermediate band and tandem hybrid solar cells and (c) MEG+IB hybrid solar cells.

The introduction explains the needs in solar cell technology and the purpose of this research along with its motivation. Chapter 2 introduces the detailed balance limit of single junction solar cell, MEG, tandem and intermediate band solar cells to understand and support the novel concept of hybrid solar cells. In chapter 3, the author discusses the thermodynamic limit of MEG solar cells and how low optimum bandgap materials can benefit the multijunction solar cell, and the delayed threshold energy can provide the impact of reducing MEG effect through different light concentration.

In chapter 4, the author will discuss MEG and multijunction hybrid solar cells with assumption of carrier multiplications at each junction where a small number of junctions is achieved with enhanced theoretical conversion efficiencies compared to conventional tandem solar cells. For instance, two or three junctions of MEG and multijunction hybrid solar cells are shown as having better performance than three or four junctions of tandem solar cells.

In chapter 5, based on the theory behind the interaction of MEG and multijunction hybrid solar cells, the author discusses limiting efficiencies of silicon-based MEG solar cells with a concentrator and various threshold energies. Further, silicon-based double junction MEG and multijunction hybrid solar cells are discussed where silicon (with 1.12 eV bandgap) is used at the upper junction materials and the appropriate bottom junction materials are searched based on theoretical efficiency calculations. Chapter 5 also includes the non-ideal quantum yield to calculate the limiting efficiency of silicon-based nanostructured multijunction solar cells.

In chapter 6, experimental results are discussed of electrical and optical properties of a proto-type silicon nanostructured solar cell that that it is defined by electron beam lithography and reactive ion etching technology. The author discusses the importance of silicon nanostructured solar cells for further improvements like carrier multiplications. Its experimental conversion efficiency achieved about 6.4% conversion efficiency including an increased light-generated current, which has an optical resonance near bandgap of amorphous-silicon region.

Chapter 7 will discuss the detailed balance limit of intermediate band and tandem solar cells showing how a double junction in this hybrid solar cell can gain efficiency comparable to the conventional six-junction tandem solar cells. This efficiency gain is due to three carrier transitions in the intermediate band solar cells. After calculating the detailed balance limit, the author discusses the appropriate material needed for above 3eV intermediate band and tandem hybrid solar cells.

Chapter 8 covers intermediate band solar cells of carrier multiplications hybrid solar cells. The intermediate band (IB) has metallic properties which are at half-filling states. The properties of IB for MEG in IB solar cells will be discussed through carrier multiplication of IBSC.

Finally, the author will offer conclusions presenting the overall benefits of hybrid solar cells and discuss future research.

CHAPTER 2

THERMODYNAMIC LIMITS OF SINGLE JUNCTION, TANDEM, MULTIPLE EXCITON GENERATION, INTERMEDIATE BAND SOLAR CELLS

2.1 Background of Detailed Balance Limits

The detailed balance limit is the theoretical approach most typically used to calculate the performance limits for solar cells. It is the primary tool used in this research to calculate the efficiency of the proposed PV approaches. The following chapter presents the detailed balance approach, and applies it to the advanced concepts of multiple exciton generation and intermediate band processes.

. Detailed balance was applied to solar cells by William Shockley and Hans J. Queisser, who showed that a single p-n junction solar cell has a theoretical efficiency limit, also known as the Shockley-Queisser limit or the detailed balance limit [8].

The detailed balance limit is deeply related to thermodynamics, which is based on four fundamental laws:

(1) The zeroth law states that when two systems sit in equilibrium with a third system, they are also in thermal equilibrium with each other;

(2) The first law, also known as Law of Conservation of Energy, states that energy cannot be created or destroyed; it can, however, be redistributed or changed from one form to another.

(3) The second law refers to the increased entropy that occurs in any isolated system, which is not in thermal equilibrium.

(4) The third law states that the entropy of a system approaches a constant value as the temperature approaches zero [17].

Every system in thermal equilibrium physics is satisfied by zeroth and first laws of thermodynamics. When including the second law, the detailed balance limit provides an explanation about the upper limit of an ideal solar cell related to the temperature of both the sun and solar cell.

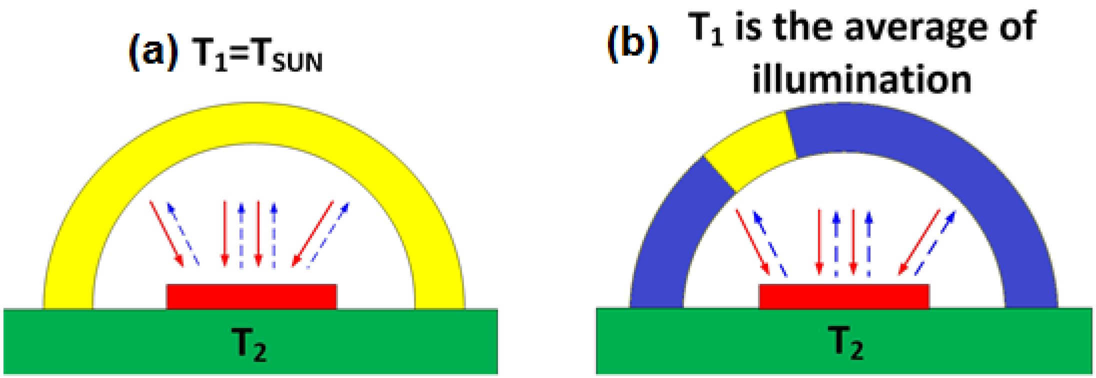

Fig. 2.1. (a) In this solar cell model (a), the detailed balance limit, shows T_1 representing solar radiation as it relates to the temperature of the sun with full exposure. Fig. 2.1b (T_2) also shows temperature radiation angles within the solar cell, but this model is only partially exposed to the sun [7].

Under maximum concentration as shown in Fig. 2.1 (a), the solar cell absorbs incident photons from every direction. The realization of this requires optical approaches. Fig. 2.1 (b) shows a solar cell without concentrated sunlight. In this case, the solar cell emits radiation in all directions, but at any given time only a portion of the sky radiates sunlight on the solar cell. .

After absorbing the incident photons greater than bandgap energy, there is one electron and hole pair (EHP) generated. Shockley and Queisser have presented that there are five carrier processes which can occur: (1) one EHP generation, (2) radiative recombination, (3) non-radiative generation, (4) non-radiative recombination and (5) removing electron from n-contact and hole from p-contact [12]. In the steady state, the sum of these five processes should be zero to calculate the current-voltage characteristics. But, non-radiative processes like (3) and (4) are often not included in efficiency limit calculations and only the radiative recombination process is considered in the detailed balance limit calculations [12].

The detailed balance limit is a purely rate based calculation between (1) solar particle flux and (2) EHP generation and recombination.

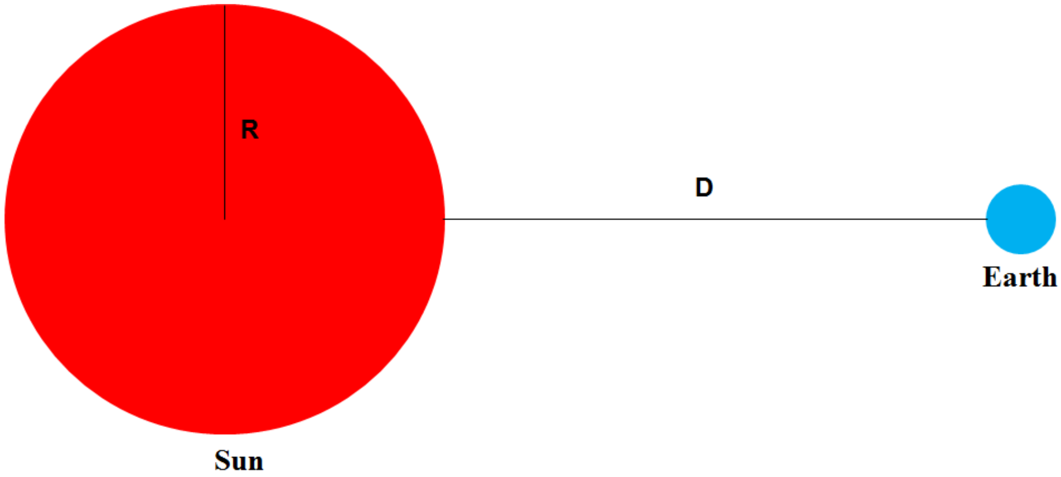

Fig. 2.2. Illustration of solar photon energy distribution between the Sun and the Earth.

To calculate the light-concentration in the solar cells, a geometrical factor is important which is related to the distance between the Sun and the Earth. Fig. 2.2 shows the dilution of sunlight as dependent on the amount of solar radiation reaching the Earth. The sunlight intensity is smaller with increasing distance of an object from the Sun. If a radius of the Sun is R and a radius of the Earth's orbit from the Sun is D, the energy density at the Earth surface is a ratio of $(=4\pi\cdot R(=696\mathrm{M}\cdot\mathrm{m})^2\cdot QS/4\pi\cdot D(=150\mathrm{G}\cdot\mathrm{m})^2=f_S\cdot Q_S)$ where Q_S is the emission energy of Sun. Therefore f_S $(=2.16\times10^{-5}$ or $1/46200)$ is called a geometric factor or dilution factor. And, its factor is related to the incident power and incident angle of solar cell [12],[18].

2.2 The Detailed Balance Limit

The detailed balance limit of solar cells is a tool for calculating the theoretical maximum conversion efficiency of the proposed ideal solar cell model. The first theoretical approach to calculate the efficiency of single junction solar cells was developed and calculated by Shockley and Queisser (SQ) [12]. Its SQ limit has provided the key-directions to develop the solar cells to reach their calculated efficiency. As results, the experimental results are within the SQ limit.

The following assumptions of detailed balance define the ideal solar cell:

(1) one electron and hole pair generation per photon,

(2) the radiative recombination of a photon emission,

(3) infinite mobility, and

(4) the complete absorption of all photons above the bandgap.

Fig. 2.3 describes the process of one EHP generation for single junction solar cell. While photon energy with greater than bandgap energy is incident into solar cells, there is electron and hole pair generation. The excited electron at the conduction band contributes to the production of an electrical current. Due to the infinite mobility of carriers, the quasi-Fermi level is constant in a p-n junction. The general approach of detailed balance is based on the thermodynamic laws where solar energy is exchanged with the ideal photovoltaic devices [12],[18].

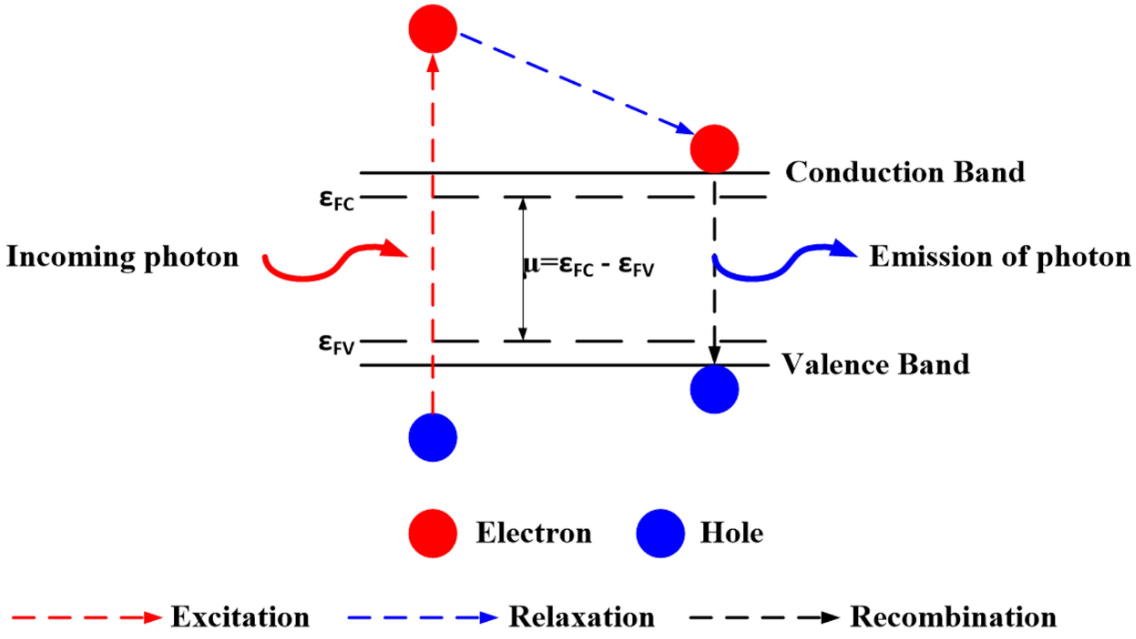

Fig. 2.3. This illustration shows the process of one-electron and hole pair generation of a single junction solar cell where μ is the chemical potential, and ε_{FC} and ε_{FV} are the Fermi level at conduction band and valence band, respectively.

The detailed balance or thermodynamic limit model is based on the particle flux of Plank's equation, which is shown in Equation (2.1). Based on this equation, the general detailed balance equations of solar cells are obtained in equations (2.1), (2.2) and (2.3) ([12], [18]).

The detailed balance or thermodynamic limit model is based on the particle flux of Plank's equation, which is shown in Equation (2.1). In Equation (2.2), the first term is the absorption from the Sun, the second is the absorption from the blackbody radiation of the earth and the last terms is the emission of photon or emission flux. Equation (2.3) is the chemical potential or quasi-Fermi level separation of solar cell.

$$\phi(E_1, E_2, T, \mu) = \frac{2\pi}{h^3c^2} \int_{E_1}^{E_2} \frac{E^2}{e^{(E-\mu)/kT} - 1} dE \tag{2.1}$$

$$J_{BB} = q \cdot [f_S \cdot C \cdot \phi(E_g, \infty, T_S, 0) + (1 - C \cdot f_S) \cdot \phi(E_g, \infty, T_C, 0) - \phi((E_g, \infty, T_C, \mu_g)] \tag{2.2}$$

$$\mu_g = q \cdot V \tag{2.3}$$

where ϕ is the solar photon flux under a given photon energy range between E_1 and E_2, f_S is the geometric factor(= 1/46200) and C is the concentration of sunlight (=1~46200), q is the element of charge ($=1.6\times10^{-19}$ C), k is the Boltzmann constant ($=1.38\times10^{-23}$ J/K), h is Plank's constant ($=6.63\times10^{-34}$ J·s), c is the speed of light (3×10^{8} m/s), f_S is the geometric factor (=1/46200), E_1 is the low energy state and E_2 is the high energy state, T_S is the temperature of the sun (=6000 K), T_C is the solar cell's temperature (=300 K), and $\mu_g(=q\cdot V)$ is the chemical potential of single junction solar cell where V is the operating voltage.

Typically, the full concentration is directly related to a geometric factor, $C=1/f_S$ in equation (2.2), that the solar cells absorbs sunlight from all directions so that the value of C is 46200 suns.

The maximum power of solar cell is calculated by

$$P = \frac{J_m \cdot V_m}{C \cdot f_S \cdot \sigma \cdot T_s^4} \tag{2.4}$$

where J_m and V_m are the current density and operating voltage at the maximum power point; the subscript m stands for maximum power, and σ is the Stefan-Boltzmann constant ($=5.67 \times 10^{-8}$ $Wm^{-2}K^{-4}$)

If the input spectrum is changed to the terrestrial spectrum, Equation (2.2) is replaced by (2.5)

$$J_{AM1.5} = q \cdot [C \cdot \int_{E_g}^{E_{g,max}} \Gamma_{AM1.5} dE + (1 - C \cdot f_S) \cdot \phi(E_g, \infty, T_C, 0) - \phi(E_g, \infty, T_C, \mu_g)] \tag{2.5}$$

where $\Gamma_{AM1.5}$ is the terrestrial spectrum from ASTMG 173-03 and $E_{g,max}$ is the end of photon energy in terrestrial spectrum (=4.428 eV)

Based on these equations, the results were obtained for both blackbody radiation and a terrestrial spectrum as a function of bandgap under one sun and full concentration (=46200). The results are shown in Fig. 2.4 and Table 2.1.

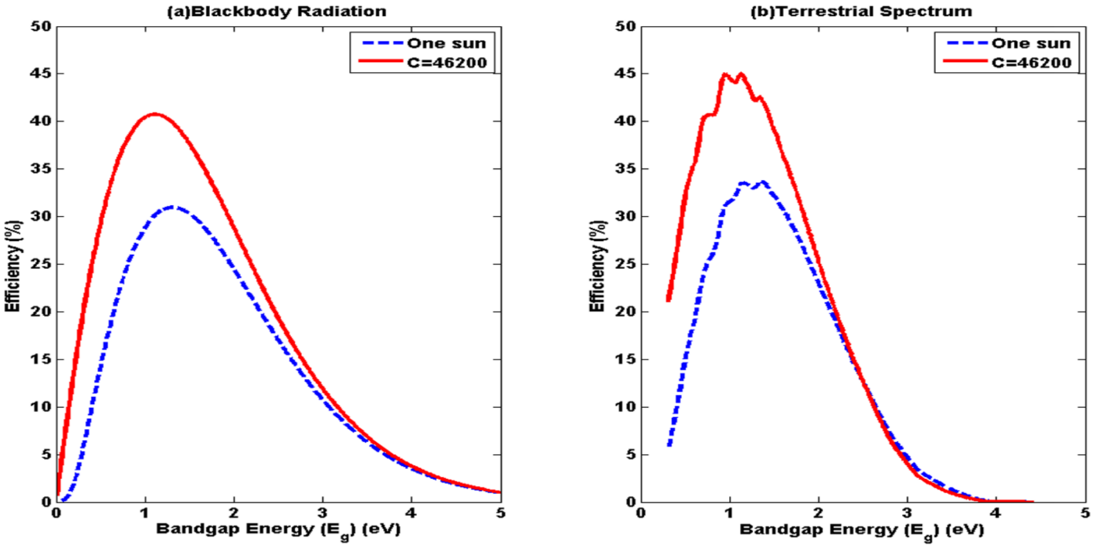

Fig. 2.4. The efficiency with Eg variation of single junction solar cells (Black Body and terrestrial spectrum) where (a) is blackbody radiation with one sun and full concentration (C=46200) and (b) is terrestrial spectrum with one sun and for full concentration (C=46200)

Table 2.1. The maximum efficiency and optimum bandgap of single junction solar cell with different spectrum and concentration.

One Sun	Efficiency	Optimum Bandgap
Black Body	31.0%	1.31 eV
AM1.5G	33.7%	1.34 eV
C=46200	Efficiency	Optimum Bandgap
Black Body	40.7 %	1.11 eV
AM1.5D	45.1 %	1.12 eV

To calculate the theoretical efficiency of a terrestrial spectrum case, the author used the AM1.5G for one sun and AM1.5D for full concentration (C=46200).

The well-known maximum conversion efficiency for blackbody radiation is 31.0% and the remaining 69% value represents a loss for solar cells. Those losses are composed of thermalization of hot carriers, transmission, radiative emissions, contact, etc. Among these losses, the thermalization of hot carriers is dominant, which comprises about 50% of losses. Once excited electrons with excess energy are in the conduction band, these carriers are experienced with lattice scattering (=phonon emission) until the carriers are relaxed to the conduction band edge. The heat loss is defined as the thermalization loss [19].

To minimize the losses of solar cells, the concentration is the first solution. However, the maximum conversion efficiency of single junction solar cell under maximum concentration (C=46200) is 40.7% under blackbody radiation that approximately, 60% of solar energy is not converted. In other words, the minimization of thermalized hot carriers is important for further improvements of single junction solar cell by various ways. Thus, the author would like to discuss three different solar cells which are tandem solar cells, multiple exciton generation and intermediate band solar cell in the next three chapters.

2.3 Tandem Solar Cells

Tandem or multijunction solar cells are composed of multilayers of well-matched different bandgap materials. There are many reports about detailed balance calculations for tandem solar cells, which includes finding the appropriate materials [20],[21].

Tandem solar cells are also the one of most commercialized solar cells. Today's current-matched tandem solar cells have focused on triple junction solar cells, which achieved 43.5% of GaInNAs/GaAs/InGaP (lattice-matched growth) with 500 suns [22] and 44.4% of InGaAs/GaAs/InGaP (inverted metamorphic growth) with 302 suns [6]. The current world record of 4 junction tandem solar cells is 44.7% of wafer bonding approaches with InGaP/GaAs//InGaAsP/InGaAs under 297 suns [11],[23].

The detailed balance of tandem solar cells is based on (1) the model of a single junction solar cell, (2) spectral splitting to find optimum bandgaps and maximum theoretical conversion efficiencies and (3) the perfect mirror between layers where other photon energy greater than bottom junction is not related to other layers.

Two kinds of connections can be used, which are independent and series connections. Optimum conversion efficiency is calculated by (1) adding maximum power at each junction for independent connection tandem solar cells and (2) current-matching of each junction for series connection [20]. Fig. 2.5 shows a schematic of tandem solar cells and two kinds of connections are described for double junction tandem solar cells. Independent or unconstrained connections are not electrically coupled for each sub-cell. The series connection of tandem solar cells is calculated by finding the current-matched conditions for the individual junctions. For instance, Fig. 2.5 (b) is an independently connected double junction solar cell and Fig. 2.5 (c) is the series-connected double junction solar cell; their general mathematical relationships are summarized in Table 2.2

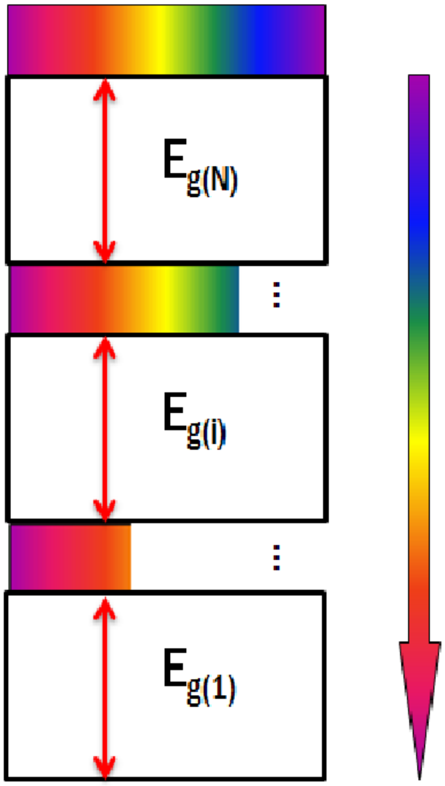

(a) Tandem Solar Cells

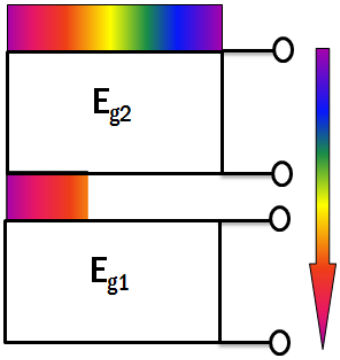

(b) 2J Independent Connection

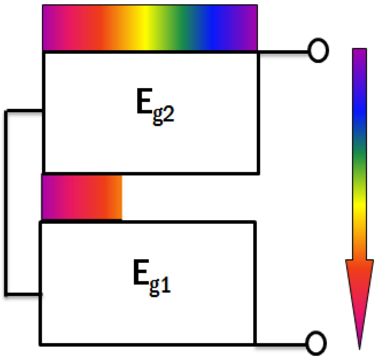

(c) 2J Series Connection

Fig. 2.5. The schematic of tandem solar cells: (a) shows is the general schematic of tandem solar cells, (b) shows a two-junction independent connection, and (c) shows a two-junction series connection where $E_{g(i)}$ stands for bandgap energy of each sub-cell in tandem solar cells, and i=positive integer.

Table 2.2. The relationship of theoretical efficiencies for tandem solar cells between an independent connection and a series-connection. J is the current density and V is the operating voltage, J_m is the current density at maximum power point and V_m is the operating voltage at maximum power point. P_{max} is the maximum power, and i=1,2,3…N.

Connection	Current Density	Operating Voltage	Maximum Power
Independent Connection	$J_{m,i}$	$V_{m,i}$	$P_{max} = \sum_{i=1}^{N} J_{m,i}V_{m,i}$
Series Connection	$J_{Total}=J_1=\cdots=J_N$	$V_{Total}=V_1+\cdots+V_N$	$P_{max}=J_{Total}V_{Total}$

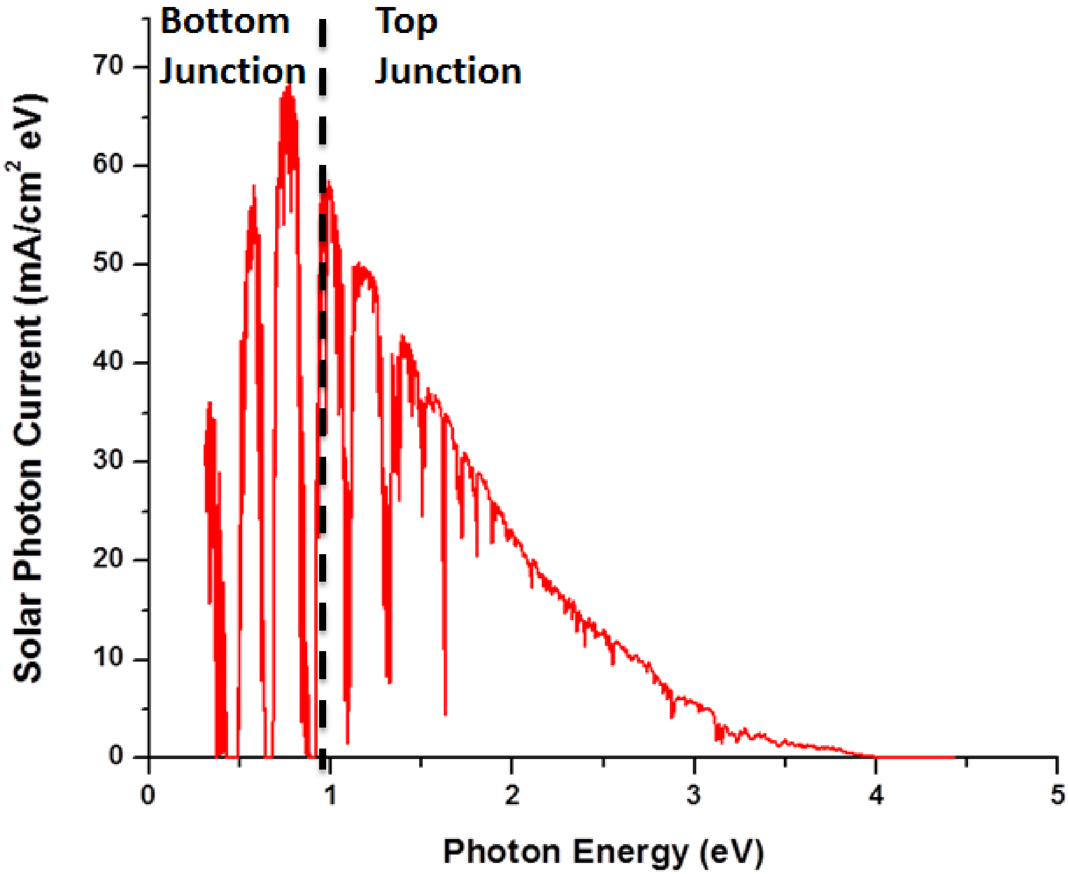

Fig. 2.6. The spectral splitting of double junction tandem solar cells

The spectral splitting is also important to find optimum conditions of tandem solar cells. Fig. 2.6 describes the procedure of spectral splitting in double junction tandem solar cells under terrestrial spectrum. The dotted line in Fig. 2.6 is the boundary of solar spectrum for a double junction tandem solar cell; above this photon energy, photons are absorbed in the top junction and below it they are absorbed in the bottom junction(s)While shifting this boundary point, we can obtain the conversion efficiencies and the corresponding optimum bandgaps. At the boundary, there is a perfect mirror to split the solar spectrum. The overall simulation results of double junction tandem solar cells are shown in Fig. 2.7 and Table 2.3 under one sun illumination.

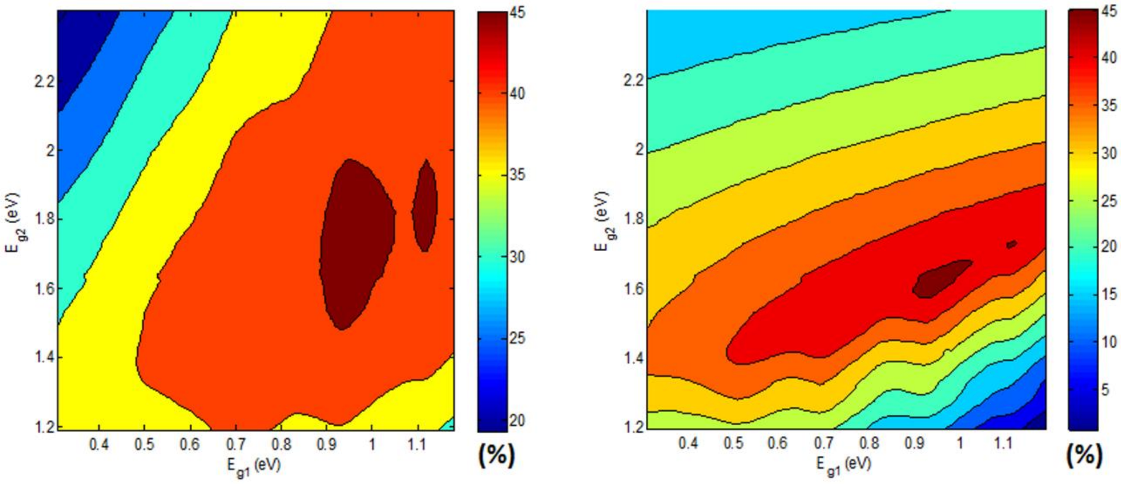

(a) 2J Independent connection **(b) 2J Independent connection**

Fig. 2.7. The efficiency contour of 2 junction tandem solar cells

Table 2.3. The efficiency table of double junction tandem solar cells under one sun illumination with terrestrial spectrum (AM1.5G spectrum).

Number of Junction	E_{g1} (eV)	E_{g2} (eV)	Efficiency (%)
2 (Independent connection)	0.94	1.73	46.1
2 (Series Connection)	0.95	1.61	45.7

The overall results shown in Fig 2.7 are that the contour plots of a 2J independent connection shown in Fig. 2.7 wherein (a) is broader than that of the series-connection and However, the series connection should be matched with the lowest current of a junction, thereby creating its contour region as shown in Fig 2.7 (b), which is narrower than the independent connection.

2.4 The Multiple Exciton Generation Solar Cells

The detailed balance of single junction solar cell is based on one electron-hole pair generation per incident photon giving a maximum theoretical efficiency for photovoltaic (PV) devices of 31 % under one sun illumination with blackbody radiation [12]. As mentioned in section 2.2, the thermalization of hot carriers at the conduction band is the largest amount of losses of single junction solar cells. Thus, if this thermalization loss can be reduced in the solar cell, a higher efficiency can be realized.

When incoming photon energy is greater than bandgap hit is incident on a single junction solar cell, detailed balance calculations assume that there is one EHP. This process is shown in Fig. 2.8 (a).

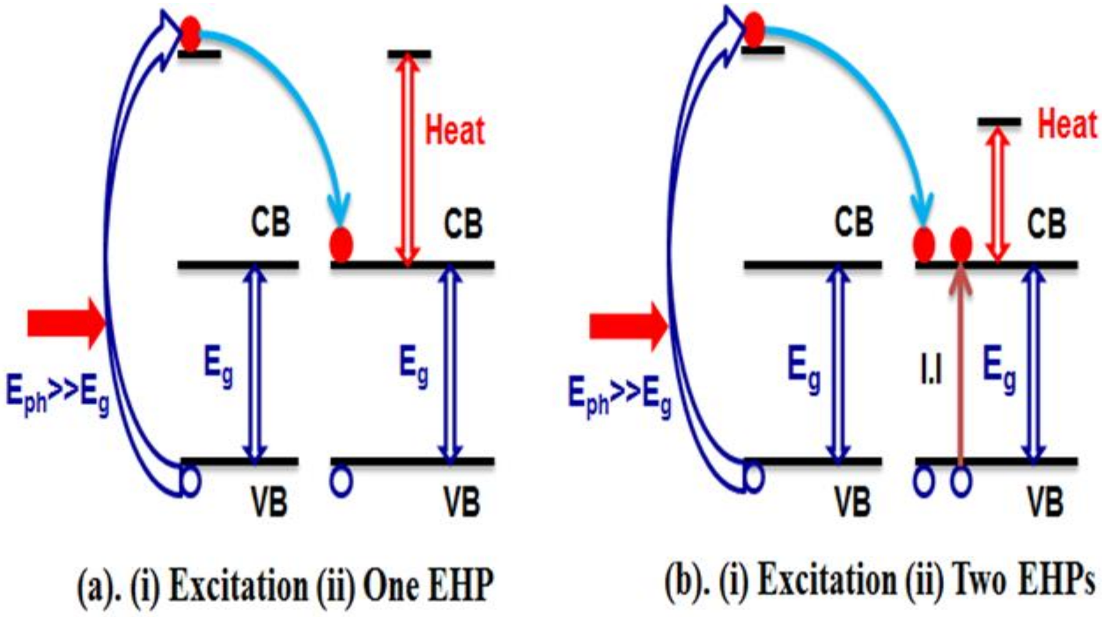

Fig. 2.8. (a) Thermalization of electrons of single junction solar cells results in energy loss and heat generation; (b) MEG has the potential to create more than one EHP per absorbed high energy photon where E_{ph} is the photon energy, CB is the conduction band, VB is the valence band and I.I is the impact ionization © [2013 IEEE] [24]. (see Appendix. B)

The excess energy of the incident photons makes possible the generation of more than two EHPs due to impact ionization. This process is called the carrier multiplication or multiple exciton generation (MEG).

Such processes were first measured in a solar cell device by Kolondinski [13] in 1993, with a quantum efficiency over 100% from a bulk type of silicon solar cell.

Subsequently, Werner published the detailed balance limit of carrier multiplication for the blackbody radiation and terrestrial spectrum under one sun. The optimum bandgaps (E_g) are 43.6% at 0.758 eV and 44.2% and 0.7 eV under blackbody radiation and AM1.5G respectively [14],[25]-[27] The detailed balance limit of MEG includes the quantum yield (QY) which is stair-case step function after threshold energy which is energy over QY over 100% and its value is two times of bandgap energy [26]. It will be discussed in section 3.2 with Fig 3.2.

Compared to single junction solar cell, the assumption of one EHP generation is no longer followed in MEG solar cells, such that a single photon can create more than two EHPs by the impact ionization. The reverse MEG process contributes to emit one photon emission by Auger mechanism [28]. The multi-carries interactions at the conduction band are explained by Auger recombination. In the thermodynamics of MEG, multi-carrier recombination can transfer energy to an electron having the highest energy state to emit a single photon. Thus, it means that voltage is not increased by quantum yield that explains the emitted photon energy. But, it experimentally shows many differences such as a radiative emission, a faster generation rate than bulk Auger mechanism.

Recently, the nano-crystals or quantum dots have demonstrated the MEG effects for high energy photons by using PbSe and PbS colloidal quantum dots over 300% of internal quantum efficiencies with delayed the threshold energy that it is the energy of QY over 100% [29].

A QY measurement by ultra-fast transient absorption spectroscopy shows that the QY linearly increase after the threshold energy and its threshold energy is generally between $2 \cdot E_g$ and $3 \cdot E_g$ [29]. But, the effect of increasing threshold energy provides the huge impacts for maximum conversion efficiency and its optimum bandgap. Therefore, the generalized detailed balance limit of MEG solar cell in the thermodynamic limit will be discussed in the Chapter 3 with different QY (Ideal and non-ideal QY) and the change of threshold energy.

2.5 The Intermediate Band Solar Cells

The intermediate band solar cell (IBSC) was proposed by Marti and Luque in 1997 [15]. The band structure of an intermediate band solar cell is shown in Fig 2.5 [15], where an additional energy level (or band) is introduced into the previously forbidden band gap. Crucially, the band has a separate quasi-Fermi level than either the conduction or valence band.

Conventional assumptions of IBSC are (1) only radiative recombination (2) the infinite mobility to make constant of the quasi-Fermi levels and make three separate quasi-Femi levels (ε_{FC}, ε_{FI} and ε_{FV}) shown in Fig 2.9, (3) no carrier extraction at intermediate band (electrons in conduction band and holes in the valence band can only be extracted to the ohmic contact), (4) absorption of all photon above the band gaps, (5) a perfect mirror at the back of IBSC that the radiation generated can only escapes to the front side of illumination (similar to tandem and single junction solar cells), (6) isotropic illumination of cell for maximum efficiency [15].

The IB level makes it possible to generate three transitions which are (1) from valence band to conduction, (2) valence band to intermediate band and (3) intermediate band to conduction band. Then, two carriers at a conduction band can contribute to generate an electrical current because of assumption (1) and (3). Fig. 2.9 shows about the band structure and carrier transitions in an IBSC. Further, the intermediate band shows a metallic band properties that it is half-filling state which it is electrically isolated [15],[30].

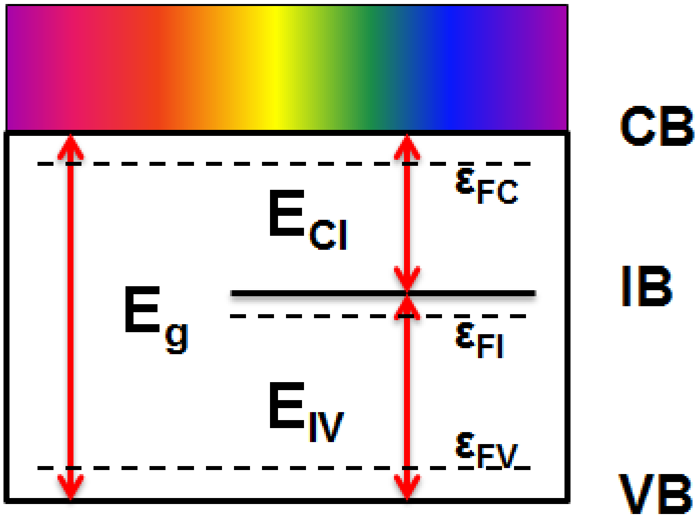

Fig. 2.9. The carrier transitions of intermediate band solar cells, where E_g is the bandgap, E_{CI} is energy between intermediate band and conduction band, E_{IV} is the energy between intermediate band and valence band, subscripts (V, I, C) are valence band, intermediate band and conduction band respectively.

$$\phi(E_1, E_2, T, \mu) = \frac{2\pi}{h^3c^2}\int_{E_1}^{E_2}\frac{E^2}{e^{(E-\mu)/kT}-1}dE \tag{2.6}$$

$$\begin{aligned}J = q\cdot\{&[f_S\cdot C\cdot\phi(E_g,\infty,T_S,0)+(1-f_S\cdot C)\cdot\phi(E_g,\infty,T_C,0)-\phi((E_g,\infty,T_C,\mu_{CV})]\\ &+[f_S\cdot C\cdot\phi(E_{CI},E_{IV},T_S,0)+(1-f_S\cdot C)\cdot\phi(E_{CI},E_{IV},T_C,0)-\phi((E_{CI},E_{IV},T_C,\mu_{CI})]\}\end{aligned} \tag{2.7}$$

$$\begin{aligned}&f_S\cdot C\cdot\phi(E_{CI},E_{IV},T_S,0)+(1-f_S\cdot C)\cdot\phi(E_{CI},E_{IV},T_C,0)-\phi(E_{CI},E_{IV},T_C,\mu_{CI})\\ &=f_S\cdot C\cdot\phi(E_{IV},E_g,T_S,0)+(1-f_S\cdot C)\cdot\phi(E_{IV},E_g,T_C,0)-\phi(E_{IV},E_g,T_C,\mu_{IV})\end{aligned} \tag{2.8}$$

$$\mu_g = \mu_{CI} + \mu_{IV} \tag{2.9}$$

where T_S is the temperature of the sun (=6000 K), T_C is the solar cell's temperature(=300 K), ϕ is the solar photon flux under given photon energy range between

E_1 and E_2, i=1,2,⋯, f_S is the geometric factor(= 1/46200) and C is the concentration of sunlight, q is the element of charge, k is the Boltzmann constant (=1.38×10^{-23} J/K), h is the Plank's constant (=6.63×10^{-34} J·s), c is the speed of light (3×10^{8} m/s), E_1 is the low energy state and E_2 is the high energy state. μ_{CI} is the chemical potential between conduction band and intermediate band, μ_{IV} is the chemical potential between valence band and intermediate band and μ_g is the chemical potential for bandgap.

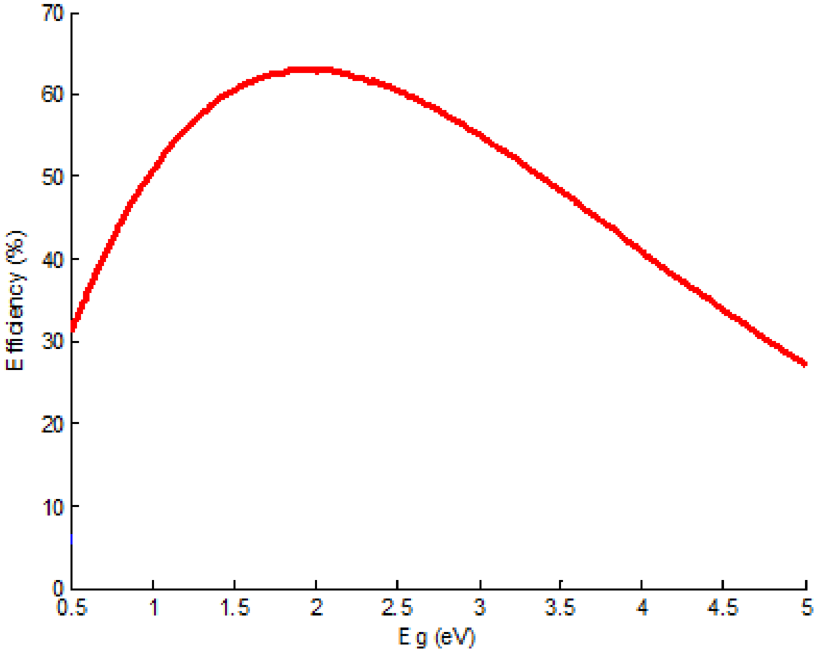

Fig. 2.10. Efficiency vs bandgap of conventional intermediate band solar cells under fully concentrated sunlight (C=46200) accounting for bandgap optimization.

Equations from (2.6) to (2.9) are the detailed balance equations of IBSC. To determine appropriate intermediate band level, the generation rate and recombination rate of between (1) valence band to intermediate band and (2) intermediate band to conductions should be the same and it is shown in Equation (2.8). The simulation results of IBSC are summarized in Fig. 2.10 and Table 2.4.

Table 2.4. The optimum bandgaps and maximum efficiency of full concentration for a single IBSC with blackbody radiation.

	E_{CI} (eV)	E_{IV} (eV)	E_g (eV)	Efficiency (%)
C=46200	0.72	1.25	1.97	63.2

Table 2.5. The optimum bandgaps and maximum efficiency of conventional triple junction solar cells for independent and series connection under full concentration with blackbody radiation.

Tandem	E_{g1} (eV)	E_{g2} (eV)	E_{g3} (eV)	Efficiency (%)
Independent Connection	0.62	1.26	2.10	63.8
Series Connection	0.60	1.14	1.82	63.1

Both Table 2.4 and 2.5 show that the theoretical conversion efficiency of IBSC under full concentration is similar to those of triple junction tandem solar cells under full concentration. In implementing intermediate band solar cells, III-V quantum dot structures provide promising structures of IBSC in which two materials (one is for barrier and the other is for quantum dot) form the IBSC. IBSC with III-V quantum dot provides a higher theoretical efficiency than a single junction solar cell. This advantage will be discussed in the chapter 7 by forming a hybrid with a tandem solar configuration.

CHAPTER 3

IMPACT OF THRESHOLD ENERGY ON LIMITING EFFICIENCIES IN MULTIPLE EXCITON GENERATION SOLAR CELLS

3.1 Introduction

Multiple exciton generation (MEG) [4],[31],[32] solar cells offer an approach to increasing solar cell efficiency above the Schockley-Queisser limit (or single junction solar cell limit) [12] without the need for multiple junctions. Prior to its examination for solar cells, the generation of multiple electrons from high energy processes has been used experimentally in several applications including impact ionization in avalanche photodiodes; the generation of multiple carriers from a high energy electron in EBIC (electron beam induced current measurements); and in radiation detectors [33]-[36]. However, these processes use excitation energies many times the bandgap, making them unsuited for absorption from the solar spectrum. However, experimental measurement of greater than unity quantum efficiency from light with photon energies between two to three times the bandgap shows that multiple electrons can be generated with energies available in the solar spectrum, with one of the first experimental demonstrations in a bulk silicon solar cell [13].

Despite the first demonstration of carrier multiplication in silicon solar cells, experimental results in MEG solar cells focus primarily on nanostructures and smaller bandgaps, due to detailed balance efficiency calculations giving the optimum bandgaps at low values [4],[31],[32]. Quantum dots are of special interest since momentum conservation rules are relaxed, hot carrier cooling rates are potentially slowed, and

Coulomb coupling is greatly enhanced to increase the rate of the Auger process [4],[31],[32]. Because of theoretical efficiency models [4],[25]-[28] which highlight the uantum yield (the ratio of the number of carriers generated to the number of photons of a given energy incident on the solar cell), experiments have focused heavily on the measurement of the quantum yield (QY).

Measurements of QY in quantum dot (QD) nanostructures initially reported QYs in a PbSe system of up to 300% [37], and measurements reported by various groups and materials showed QYs of up to 700% [38] Material systems examined include PbS [29], PbSe [29],[39], CdTe [40], CdSe [40],[41], InAs [42],[43], and Si [19],[44]. The initial high reported values of QY [38] are close to those needed for ideal thermodynamic efficiencies when a solar cell is operating at moderate concentration. However, uncertainties in the measurement of QY due to effects such as surface states and long-lived QD photocharging in the pump-probe measurements [45]-[51] have resulted in accepted values up to 300% [48] in QD systems to 130% for PbSe QDs without using the transient-absorption method [52]. These QY studies also include measurements of the threshold energy. For example, a measurement of Si nanocrystals gives a QY of 260% and a threshold energy of $2.4E_{g,si}$ where $E_{g,si}$ is the effective bandgap of the Si nanocrystals [44]. Threshold energies of other materials range from $2.2E_g$ [53] to $4.2E_g$ [51].

The inclusion of less ideal QYs and concentration consistent with physically realistic levels (i.e., below the maximum concentration of 46200 assumed in detailed balance) changes the theoretical efficiency as well as the optimum bandgaps for the MEG process. While there have been numerous detailed balance studies for MEG processes [14],[25],[26],[54]-[56], including the impact of non-ideal QYs [54]-[56], the impact of the threshold energy has examined under terrestrial spectrum. But, the blackbody radiation has not been well examined with and without light concentration. In this chapter, the author includes the threshold energies in detailed balance calculations, showing that there is no theoretical benefit from MEG processes if the threshold energy is above approximately $3E_g$ (for one sun) to $4E_g$ (for concentrated sunlight).

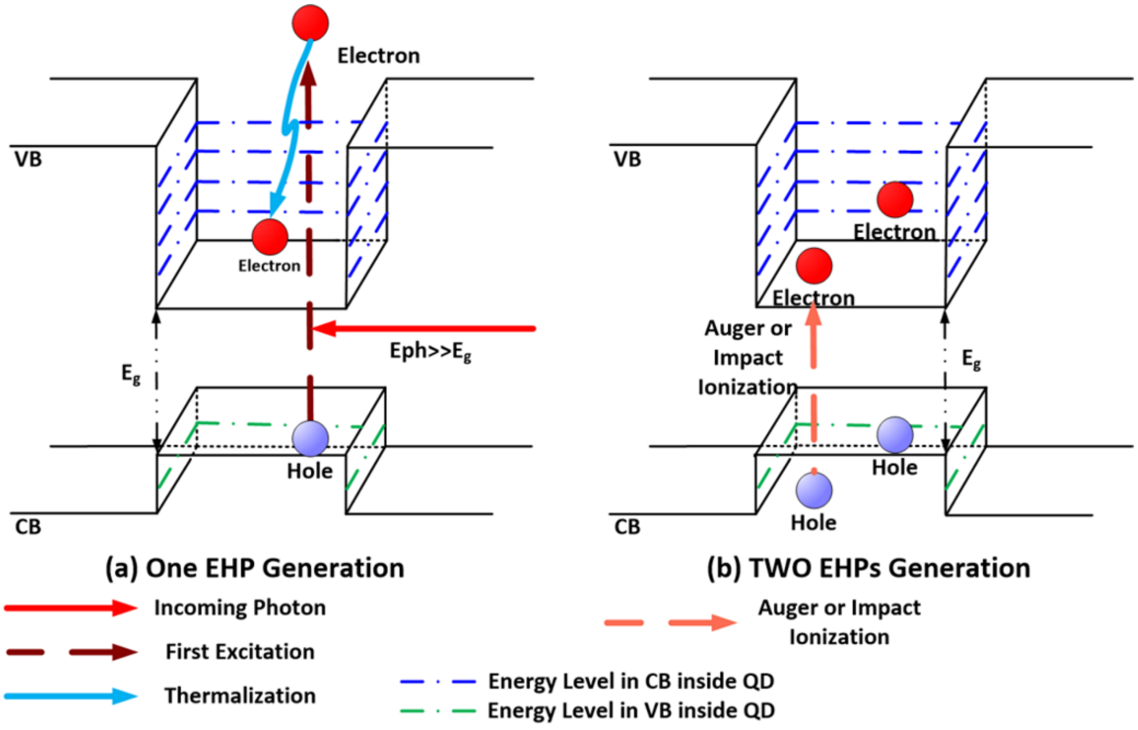

Fig. 3.1. (a) Thermalization of electrons of single junction solar cells results in energy loss and heat generation; (b) Multiple Exciton Generation results in more than one EHP per absorbed high energy photon where E_{ph} is the photon energy, E_g is the bandgap energy, CB is the conduction band, VB is the valence band.

Since measured values of the threshold energy are within this range, it is important to include threshold energies in the detailed balance calculations. Further, the impact of the threshold energy with higher concentration voids the design rule in which lower bandgaps increase the theoretical efficiency of an MEG solar cell.

MEG solar cells increase the theoretical solar cell efficiency compared to a single junction solar cell by using photons with energy at least twice the bandgap to generate two or more electron hole pairs (EHPs). In a conventional solar cell (Fig. 3.1(a)), a high energy excited electron relaxes to the conduction band edge and emits heat. In MEG solar cells as shown in Fig. 3.1(b) the extra energy generates one or more additional EHPs.

3.2 Theory

The detailed balance calculations of MEG solar cells follow general detailed balance approaches, but differ from conventional detailed balance in that the assumption of one electron hole pair (EHP) per incident photon is circumvented. In conventional solar cell detailed balance calculations, the QY is assumed to be unity and the reflection is zero, giving a maximum QY of 100% for photons with energies above the bandgap and below it.

The ideal QY of an MEG cell is step-like, such that photons with energy between E_g and $2E_g$ generate a single EHP, photons with energy between $2E_g$ and $3E_g$ generate two EHPs, and so on, as shown below:

$$\mathrm{QY(E)} = \begin{cases} 0 & 0 < \mathrm{E} < \mathrm{E_g} \\ \mathrm{m} & \mathrm{m} \cdot \mathrm{E_g} < \mathrm{E} < (\mathrm{m}+1) \cdot \mathrm{E_g} \quad \mathrm{m} = 1,\ 2,\ 3,.. \\ \mathrm{M} & \mathrm{E} \geq \mathrm{M} \cdot \mathrm{E_g} \end{cases} \tag{3.1}$$

where m is the number of multiple electron hole pairs generated, M is the maximum number of electron hole pairs which are generated, E_g is the bandgap, and E is the photon energy.

The value of M (the maximum number of EHPs which are generated from a photon or the maximum QY) theoretically depends on the solar spectrum and the bandgap. For a black body (BB) spectrum, M is very large, since the BB spectrum contains photons at arbitrarily high energies, and hence even high bandgaps will encounter photons with energies many multiples of the bandgap. However, for spectra such as AM1.5, where the highest energy photon is at a finite energy (for AM1.5 (ASTMG 173-03 [57]) the highest energy photon is 4.428 eV), the maximum number of EHPs which can be generated depends on the bandgap. Fig. 3.2 (a) shows the ideal QY vs. photon energy for three bandgaps, showing that M=7 at E_g = 0.56 eV, while for a bandgap of E_g=1.68 eV, theoretically M = 2 (i.e., at most two electron hole pairs can be generated).

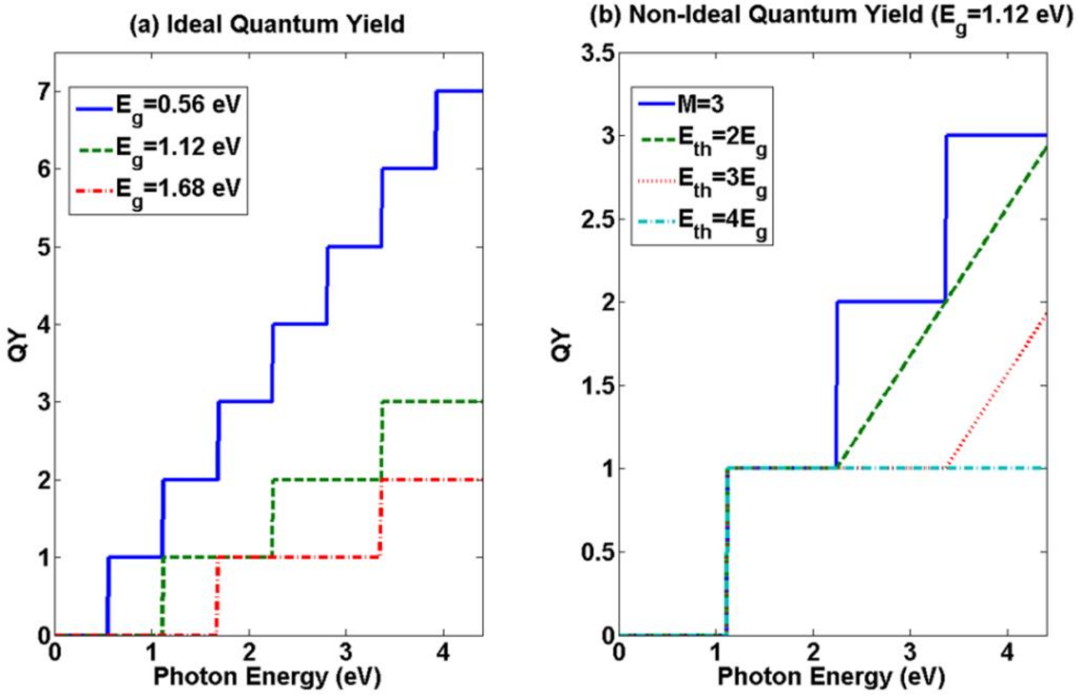

Fig. 3.2. (a) Ideal QY for three different bandgaps under the AM1.5 spectrum and (b) non-ideal QY with A=1 for one value of E_g (=1.12eV) and three different threshold energies.

Experimentally, measured QYs diverge from the ideal QY because: (1) the threshold energy for a multiple exciton generation event is $E_{th} = r \cdot E_g$ where $r \geq 2$ is a real number and (2) rather than displaying a step-function shape, experiments show a linear increase in the QY with energy. The equation for non-ideal QY is given in equation (3.2) [54].

$$QY(E) = \theta(E, E_g) + A\theta(E, E_{th}) \cdot (\frac{E - E_{th}}{E_g}),.. \tag{3.2}$$

where θ is the heaviside step function; A is the slope of the linearized QY (in terms of QY and the photon energy normalized to E_g), E_g is the bandgap; and E_{th} is the threshold energy for a MEG event.

The non-ideal QY in Fig. 3.2 (b) shows that the threshold energy has a large impact on the maximum QY. For example, for the AM1.5 spectrum, and a threshold energy $E_g = 2E_g$, M retains the same value as in the ideal case, but the maximum QY is reduced to 2 with a threshold energy of three times the bandgap (see Fig. 3.2(b) green and red lines). For this bandgap, there is no impact from MEG processes (i.e., M=1) when $E_{th} = 4E_g$.

Further, although the ideal slope A is 1, experimental measurements are best fit using less ideal values [54]. The impact of the slope vs stair-case QY has been examined in detailed balance [54] but not the impact of threshold energy. In this chapter, the author includes the effect of non-ideal threshold energies in detailed balance calculations. Particularly for the case of AM1.5 and under concentration, the threshold energy has a dominant impact on the efficiency and optimum bandgap at A=1.

Using the above non-ideal equations for QY, the theoretical thermodynamic equations for the MEG solar cell are given below, where equation (3.5) is the current density for BB radiation and equation (3.6) is that for a terrestrial spectrum.

$$\phi(E_1, E_2, T, \mu) = \frac{2\pi}{h^3c^2}\int_{E_1}^{E_2}\frac{E^2}{\exp[(E-\mu)/kT]-1}dE \tag{3.3}$$

$$\phi_{MEG}(E_1, E_2, T, \mu_{MEG}) = \frac{2\pi}{h^3c^2}\int_{E_1}^{E_2}\frac{QY(E)\cdot E^2}{\exp[(E-\mu_{MEG})/kT]-1}dE \tag{3.4}$$

$$\begin{aligned} J_{BB} &= q\cdot C\cdot f_S\cdot \phi_{MEG}(E_g,\infty,T_S,0) \\ &+ q\cdot(1-C\cdot f_S)\cdot\phi_{MEG}(E_g,\infty,T_C,0) - q\cdot\phi_{MEG}(E_g,\infty,T_C,\mu_{MEG}) \end{aligned} \tag{3.5}$$

$$\begin{aligned} J_{AM} &= q\cdot C\cdot \int_{E_g}^{E_{max}} QY(E)\cdot\Gamma(E)\ dE \\ &+ q\cdot(1-C\cdot f_S)\cdot\phi_{MEG}(E_g,\infty,T_C,0) - q\cdot\phi_{MEG}(E_g,\infty,T_C,\mu_{MEG}) \end{aligned} \tag{3.6}$$

where ϕ is the particle flux given by Planck's equation for a temperature T with a chemical potential μ in the photon energy range between E_1 and E_2 (from Equation (3.3)); ϕ_{MEG} is the particle flux for MEG solar cell (from Equation (3.4)), h is Planck's constant; c is the speed of light; μ is the chemical potential of a single junction solar cell (=q·V) where V is the operating voltage, μ_{MEG} is the chemical potential of MEG (=q·QY(E)·V); k is the Boltzmann constant; J is the current density of the solar cell; q is the element of charge; C is the optical concentration (C=1~46200); f_S is the geometry factor (=1/46200), T_S is the temperature of the sun (=6000K); T_C is the solar cell's temperature (=300K); E_{max} (=4.428 eV at 280 nm wavelength) is the highest photon energy of the terrestrial spectrum and Γ(E) is the converted terrestrial spectrum from ASTMG 173-03.

3.3 Results

Using the above equations, the well-known ideal efficiencies versus bandgap of MEG solar cells under blackbody radiation for one sun (C=1) and under full concentration

(C=46200) are shown in Fig. 3.3 (a) and (b) respectively as a function of M. Compared to existing literature, the author repeats these plots with an extended number of calculations for M in order to identify the M value after which no further efficiency increase is calculated. For the one-sun BB case, the maximum efficiency is saturated after M=13 (i.e., a total of 13 EHPs generated from the high energy photons) and the conversion efficiency is 44.7% at E_g=0.77 eV. At full concentration, the maximum conversion efficiency is 85.9% at E_g = 0.05 eV at M=200.

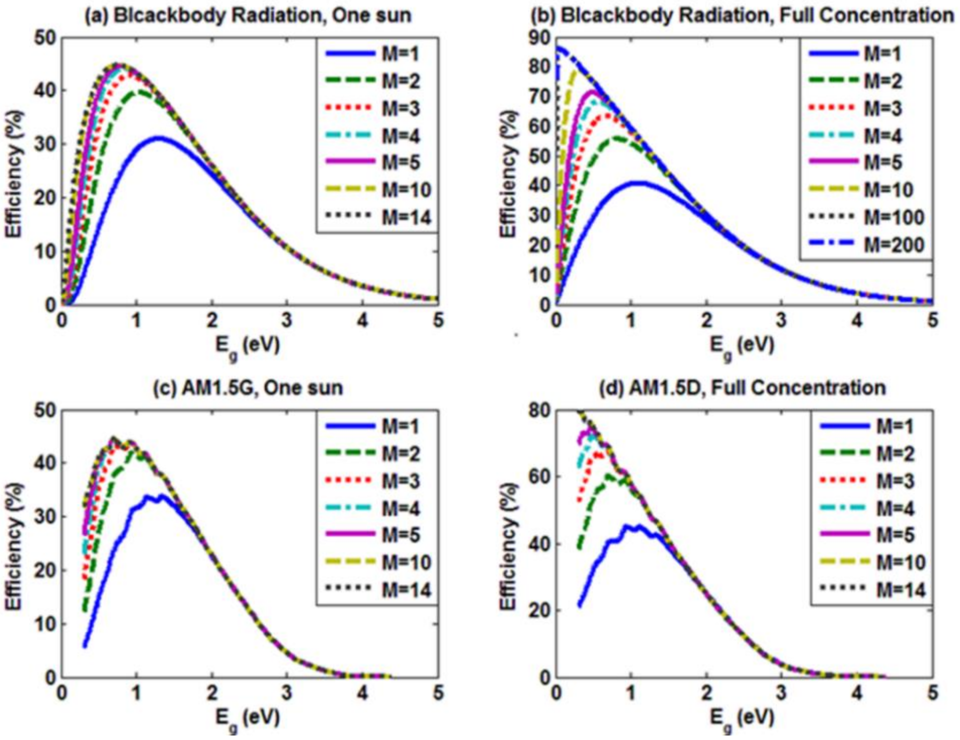

Fig. 3.3. Efficiency vs E_g with ideal QY for one sun and maximum concentration for Blackbody Radiation and terrestrial spectrum where M is the maximum QY.

The ideal MEG solar cells efficiencies for the AM1.5 spectrum under one sun and under maximum concentration are shown in Fig. 3.3 (c) and (d). For one sun illumination, the conversion efficiency is saturated at M=5 for which E_g = 0.7 eV. A QY = 300%

(corresponding to M=3), which is consistent with experimental measurements of QY, should allow close to ideal theoretical efficiencies. At maximum concentration, the conversion maximum efficiency is 79.8% at E_g = 0.31eV and M = 14. In Fig. 3.3 (c) and (d) there are no values plotted below 0.3 eV as there are no photons in the AM1.5 spectrum below this value, and reducing the bandgap below the lowest photon energy only degrades efficiency.

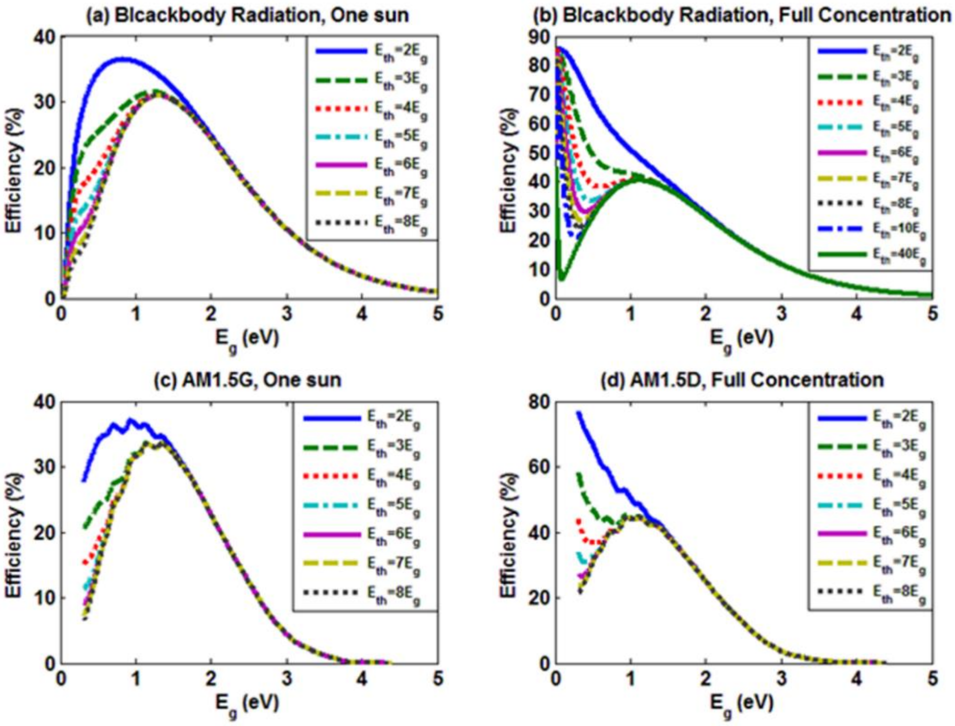
(a) Blcackbody Radiation, One sun

(b) Blcackbody Radiation, Full Concentration

(c) AM1.5G, One sun

(d) AM1.5D, Full Concentration

Fig. 3.4. Efficiency vs E_g for non-ideal QY as a function of threshold energy under both one sun and full concentration (Blackbody radiation and terrestrial spectrum)

Fig. 3.4 shows the theoretical efficiency with non-ideal QYs for BB and AM1.5 spectra. E_{th} = 2E_g corresponds to the ideal threshold energy, and QY is linearly increased (A=1) after 2E_g. For these calculations, there is no limit placed on the maximum ideal QY values as there is for the ideal QY calculations above.

The results for the BB spectrum illustrate a dual peak structure or broadening of the efficiency peak due to non-ideal Eth. Because under concentration the optimum bandgap is smaller, the efficiency curves under maximum concentration with non-ideal Eth display two peaks in the efficiency. This is due to the fact that at low bandgaps, the difference in the number of photons at energies twice the bandgap and at several times the bandgap is insignificant.

Table 3.1. Efficiency vs optimum E_g (eV) for ideal QY and Non-Ideal QY for Blackbody Radiation and ASTMG 173-03 where η (%) is the maximum conversion efficiency, M is the maximum ideal quantum yield and E_{th} is the threshold energy.

Ideal Quantum Yield								
	One sun				Full Concentration			
Black Body Spectrum								
M	1	2	¨	13	1	2	¨	200
E_g	1.31	1.05	¨	0.77	1.11	0.83	¨	0.05
η	30.9	39.6	¨	44.7	40.7	55.6	¨	85.9
Terrestrial Spectrum (ASTMG 173-03)								
M	1	2	¨	5	1	2	¨	14
E_g	1.34	0.95	¨	0.7	1.12	0.7	¨	0.31
η	33.7	41.9	¨	44.4	45.1	60.2	¨	79.8
Non-Ideal Quantum Yield								
	One sun				Full Concentration			
Black Body Spectrum								
E_{th}	$2E_g$	$3E_g$	¨	$8E_g$	$2E_g$	$3E_g$	¨	
E_g	0.84	1.24	¨	1.31	0.07	0.04	¨	
η	36.5	31.5	¨	30.9	85.8	85.7	¨	
Terrestrial Spectrum (ASTMG 173-03)								
E_{th}	$2E_g$	$3E_g$	¨	$8E_g$	$2E_g$	$3E_g$	¨	$8E_g$
E_g	0.93	1.34	¨	1.34	0.31	0.31	¨	1.12
η	37.1	33.7	¨	33.7	76.6	58.3	¨	45.0

However, as the bandgap increases, the threshold energy begins to play a strong role, such that at about $E_g \geq 0.5$ eV with $E_{th} > 4$ or 5Eg, there is essentially no efficiency benefit from MEG processes- in this bandgap range, the MEG solar cell is the same as a conventional device. At moderate threshold energies, the conversion efficiency vs. bandgap corresponds to a combination of the ideal MEG efficiency curve at low bandgaps and the ideal single junction efficiency curve at higher bandgaps. A similar effect is shown for the non-ideal MEG efficiencies at AM1.5, but with the convergence between the MEG and conventional solar cell occurring at lower E_{th}.

The key values of M, E_{th}, E_g, and efficiency are summarized in Table 3.1, and highlight the impact on optimum bandgap and efficiency of including threshold energy in the calculations. First, as expected with the inclusion of non-idealities, the overall efficiency is lower. For example, comparing the ideal M=2 case with that of the linear QY and $E_{th} = 2E_g$ under one sun illumination, the optimum efficiency is 36.5% in BB and 37.1% in AM1.5 instead of 39.6% in BB and 41.9%. Further, there is a substantial drop in the conversion efficiency with threshold energies consistent with experimental values in the range between $2E_g$ and $3E_g$. At $3E_g$, the maximum efficiency under one sun is essentially identical to a single junction solar cell, with no theoretical benefit derived from the MEG process, regardless of what the maximum QY is assumed to be.

Another substantial difference observed with the inclusion of Eth is the value of the optimum bandgap for MEG cells. In ideal QY calculations, an efficiency increase from the MEG process exists even for bandgaps up to about 0.5 eV, but when a higher E_{th} is considered, the efficiency benefits are strongly reduced at higher bandgaps. Ideal BB MEG calculations give an optimum E_g =0.05 eV at maximum concentration. While such low bandgaps are not realistic, in general the results show a slowly increasing optimum bandgap depending on the maximum QY. However, the dual peak (or peak broadening for lower concentration) voids this design rule, with the efficiency decreasing unless E_g <0.5 eV and $E_{th} < 4E_g$ are assumed. At maximum concentration with the terrestrial spectrum, after the threshold energy exceeds 4Eg, the maximum efficiency and optimum E_g is fixed at 45.0 % and E_g = 1.12 eV. Typical measurements of threshold energies are on the order of from $2E_g$ to $3E_g$, which is significant since it leads to a theoretically predicted optimum bandgap range that includes commonly used semiconductors for solar cells, including silicon.

3.4 Conclusion

In summary, the author has applied a generalized detailed balance model to MEG solar cells. For this simulation, using both ideal and non-ideal QYs the author calculates and compares conversion efficiencies under blackbody and terrestrial solar spectrum irradiation with and without concentration. Like the cases with ideal QYs, the optimal parameters (E_g and η) of non-ideal QYs (with ideal threshold energies and maximum concentration) show that the author can choose extremely low bandgap materials for MEG solar cells. However, the conversion efficiency and optimum bandgap are strongly dependent on the threshold energy, and the value of the efficiency for low material bandgaps is particularly sensitive to such non-idealities. For intermediate concentration and values of the threshold energy above $E_{th} = 3E_g$, the efficiencies and the optimum bandgaps are essentially identical to those without MEG processes.

CHAPTER 4

LIMITING EFFICIENCIES OF MULTIJUNCTION SOLAR CELLS WITH MULTIPLE EXCITON GENERATIONS

4.1 Introduction

A number of approaches have been proposed to overcome the detailed balance single junction efficiency limits calculated by Shockley and Queisser [12], including multiple junction solar cells and novel concepts such as multiple exciton generation (MEG) and intermediate band solar cells [15],[21],[58]. Multijunction (MJ) solar cells have been commercialized and demonstrate high efficiencies. However, the realization of efficiencies over 50% via conventional tandem approaches requires increasing the number of junctions in the solar cells from the present three junctions (3J) to at least four junctions (4J), introducing substantial materials challenges [59]. By including MEG processes into MJ solar cells [60], both the number of junctions and materials constraints are relaxed allowing efficiencies over 50% with a 2J and 3J device. © [2014 IEEE] [61](see Appendix. B)

4.2 Multijunction Solar Cells with MEG Process

Since MJ solar cells were first proposed by Jackson [62] in 1955, steady improvements in efficiencies have been achieved, initially through mechanical stacks (e.g., AlGaAs and Si demonstrating 28.5% at AM 1.23 165 suns in 1978 [63]), and later through monolithic structures, with most of the focus on a three junction MJ on a Ge substrate. Two junction tandem photovoltaic devices demonstrated over 30% under 140~180 suns in 1994 [64],[65] and a triple junction tandem solar cell broke the 40% barrier under 240 suns [66] in 2007 using both lattice-matched (LM) and mismatched configurations. Since then, high efficiency device structures have diversified, with a range of approaches realizing over 40% efficiency [67]-[72]. Current triple junction solar cells show 43.5% and 44.4% using dilute nitride (GaInNAsSb/GaAs /InGaP) LM approaches and InGaP/GaAs/InGaAs [6],[22] respectively.

Despite numerous experiments showing MJ devices over 40%, MJ solar cells still face barriers in reaching 50% efficiency, due to a larger required number of junctions (minimum 4J in order to achieve 50%); material defects (due to metamorphic or other growth approaches); and limited material combinations and structures that have appropriate growth technologies [73],[74]. For instance, even though the detailed balance calculations for a triple junction solar cell under one sun show a conversion efficiency over 50% [20],[58],[75],[76], the experimental results are about 10% absolute efficiency points lower. This is largely due to the inability to grow a monolithic structure with the optimum bandgaps using only closely lattice matched materials. The resulting non-optimum bandgaps give rise to current mismatches [77], and since the junctions are series connected, the overall MJ's current is limited to the lowest current. One approach to avoid this combines two solar cells with 2J each mechanically, but this represents a significant departure from existing structures [78].

An fundamental discussion of MEG solar cells have discussed in chapter 3 about the MEG phenomena, detailed balance limit and experimental approaches [13],[14],[25],[26],[79]-[81],[29],[41],[82],[83]. For a multijunction solar cells with MEG, the detailed balance for MJMEG is discussed in section 4.3.

A quantum yield over 100% has been measured in bulk silicon solar cells [13], and nanostructured materials have shown an enhanced MEG effect with quantum yields up to

300% [81]-[83]. An attractive aspect of MEG solar cells is that they allow the use of low bandgap materials. Therefore, it is of interest to integrate MEG concepts with MJ solar cells and recalculate the optimum bandgaps (E_g) to determine if this enables the use of practical materials while improving the theoretical efficiencies [60].

In this chapter, the author analyze the thermodynamic limits for MJ hybrid MEG solar cells (MJMEGs), calculating the theoretical maximum efficiency and finding the optimum bandgaps under both blackbody (BB) radiation and the terrestrial spectrum at both one sun illumination and maximum concentration.

4.3 Theory

4.3.1 Detailed Balance Calculations Including MJMEG

Thermodynamic models of multiple junction solar cells and multiple exciton generation are well documented in literature [14],[20],[25]-[28],[75],[76],[79]-[81]. Thermodynamic models of a single junction solar cell consider absorption of the solar spectrum using one bandgap and one electron and hole pair (EHP) generation per photon [12], whereas MJ solar cells have multiple bandgaps, dividing the solar spectrum among the different junctions in the stack [20],[75],[76]. An example of this spectral splitting is shown in Fig.4.1 (a) for a 4J solar cell, dividing the spectrum into 4 different bandgaps.

In detailed balance calculations for MEG devices, the author typically use ideal assumptions from detailed balance as described in [25]-[28] which state that a MEG solar ell is perfectly ideal photovoltaic device (100% absorption above band gap, recombination at the thermodynamic limit) in which there are multiple EHPs generated for a high energy photon and multi-particle recombination events emit a single photon [25]-[28].

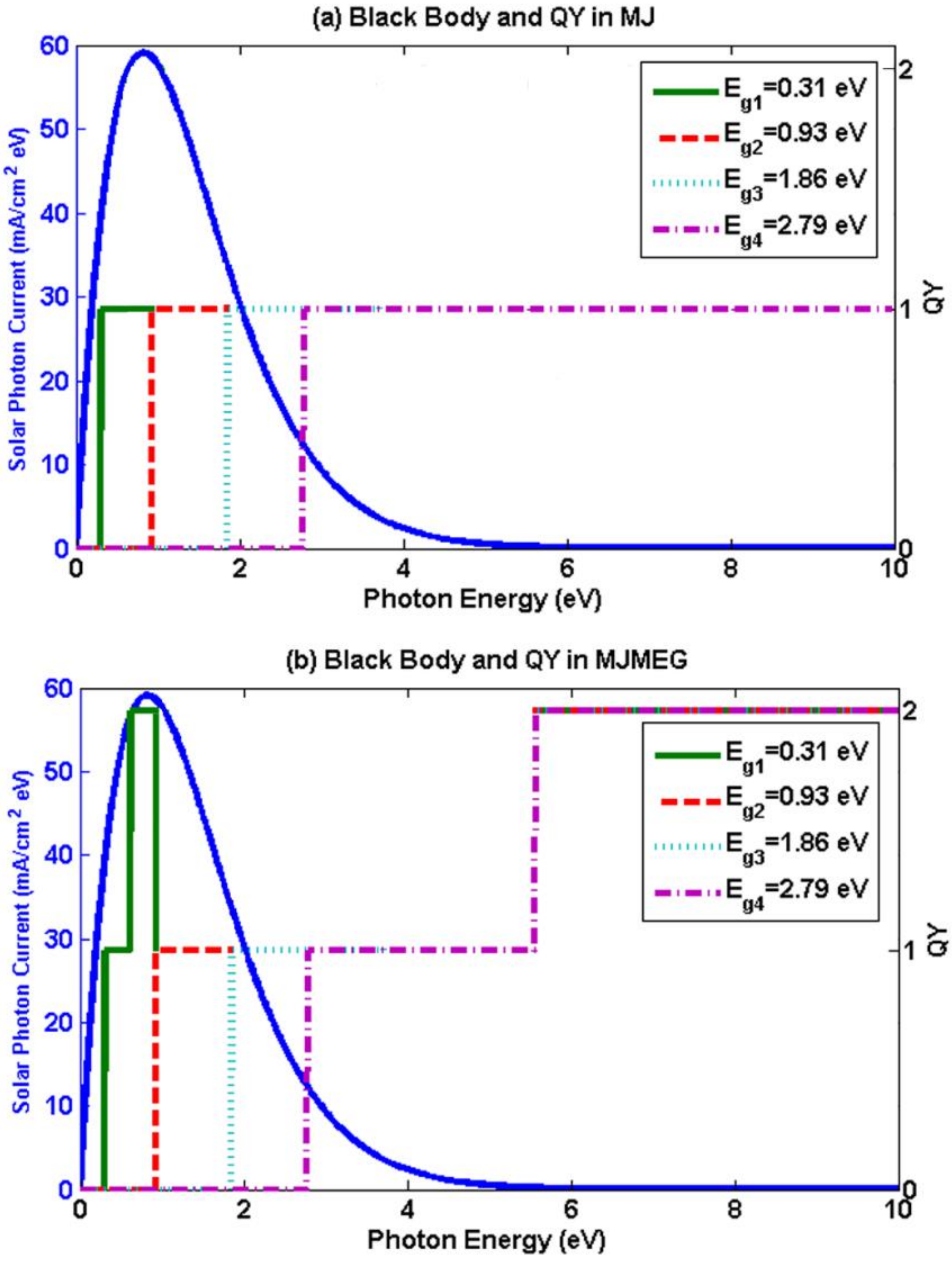

Fig. 4.1. Spectral splitting and QY in conventional MJ and MJMEG solar cells. (a) A four junction MJ solar cell. The QY of each region is 1. (b) Ideal QY for a multijunction device with MEG © [2014 IEEE] [61].

The main difference between conventional single junction or MJ and MEG solar cells is the number of EHPs generated from a particular photon wavelength or energy. The generated number of EHPs is given by the quantum yield (QY). For single junction or conventional MJ cells, QY =1 as shown in Fig.4.1 (a), but for MEG cells QY can exceed one.

In ideal MEG devices, the QY is one for photons with energies between the bandgap and twice the bandgap ($2E_g$), two for photons of energy greater than $2E_g$ but less than $3E_g$, and so on, giving in the ideal case a staircase function for the QY [60]. The equation for the ideal QY of any junction in an MJMEG cell is given by:

$$\mathrm{QY(E)} = \begin{cases} 0 & 0 < \mathrm{E} < \mathrm{E_g} \\ \mathrm{m} & \mathrm{m} \cdot \mathrm{E_g} < \mathrm{E} < (\mathrm{m}+1) \cdot \mathrm{E_g} \\ \mathrm{M} & \mathrm{M} \cdot \mathrm{E_g} < \mathrm{E} < \infty \end{cases} \tag{4.1}$$
$$\text{where } \mathrm{m} = 1,2,3\cdots, \mathrm{M}\,(= \text{Maximum QY})$$

From equation (4.1), the author defines M as the maximum value of m (i.e., the maximum number of generated EHPs) within a junction. The remaining equations in the detailed balance calculations are given in equation (4.2) to (4.5). These equations and their constants have their usual form and definition of constants as in [20],[25]-[28],[60],[75],[76]. The notation J_i, μ_i, E_i etc refers to the "i^{th}" junction, and the "i+1"th unction is the junction with above the "i^{th}" cell in the MJMEG solar cell stack where i=1,2,3…. . For a solar cell with n total junctions, the "n+1" energy in the integral limits is replaced by infinity when using a BB spectrum or the highest photon energy in the AM1.5 spectrum when using this input solar spectrum.

$$\phi(E_{(i)}, E_{(i+1)}, T, \mu) = \frac{2\pi}{h^3 c^2} \int_{E_{(i)}}^{E_{(i+1)}} \frac{QY(E) \cdot E^2}{\exp[(E-\mu)/kT] - 1} dE \tag{4.2}$$

$$\begin{aligned} J_{i,BB} &= q \cdot C \cdot f_S \cdot \phi(E_{g(i)}, E_{g(i+1)}, T_S, 0) \\ &+ q \cdot (1 - C \cdot f_S) \cdot \phi(E_{g(i)}, E_{g(i+1)}, T_C, 0) \\ &- q \cdot \phi(E_{g(i)}, E_{g(i+1)}, T_C, \mu_i) \end{aligned} \tag{4.3}$$

$$\begin{aligned} J_{i,AM1.5} &= q \cdot C \cdot \int_{E_{g(i)}}^{E_{g(i+1)}} QY(E) \cdot \Gamma_{AM1.5} dE \\ &+ q \cdot (1 - C \cdot f_S) \cdot \phi(E_{g(i)}, E_{g(i+1)}, T_C, 0) \\ &- q \cdot \phi(E_{g(i)}, E_{g(i+1)}, T_C, \mu_i) \end{aligned} \tag{4.4}$$

$$\mu_i = q \cdot QY(E) \cdot V_i \tag{4.5}$$

where ϕ is the particle flux of MEG given by Planck's equation for a temperature T with a chemical potential $\mu(=q \cdot QY(E) \cdot V)$ in the photon energy range between $E_{(i)}$ and $E_{(i+1)}$, $\Gamma_{AM1.5}$ is the terrestrial spectrum from ASTMG 173-03, h is the Plank's constant, c is the speed of light, k is Boltzmann's constant, T_S is the temperature of the sun, T_C is the temperature of the solar cell, f_S is the geometry factor (=1/46200), and C is the concentration, V is the operating voltage.

Detailed balance involves the calculation of the current from the solar cell as the difference between the absorbed and emitted photon fluxes. Equation (4.2) is the definition of the either absorbed or emitted photon flux for a MEG solar cell. Equation (4.3) and (4.4) correspond to the current generated by an MEG solar cell for the BB and AM1.5 spectrum respectively for the i^{th} solar cell in the MJMEG. The first two flux terms correspond to photons absorbed from the solar spectrum. If the i^{th} solar cell absorbs photons with more than twice its band gap (which depends on the other solar cell band gaps in the stack), the light generated current is increased compared to a conventional MJ solar cell.

The last term of equation in (4.3) and (4.4) corresponds to the emitted photon flux. The emitted photon flux is changed in an ideal MEG device compared to conventional single junction solar cell, in that the inverse of the MEG process must also occur [25]-[28]. hus, in the calculation of the emitted photon flux, the "μ_i" in equation (4.5) is modified from its definition compared to a conventional single junction or multijunction solar cell. In a conventional single junction or multijunction solar cell, it corresponds to the chemical potential, the quasi-Fermi level separation or the voltage across the device ($\mu' = q \cdot V$). In an MEG process, this is replaced by $m\mu'$, where m depends on the energy as given in (1). Physically, the QY(E) term in the emission process accounts for the use of more than two EHPs in the emission process and equation (4.5) accounts for the increased energy of the emitted photon (e.g., twice or more the bandgap) [25]-[28]. Overall, for MEG devices, the $m\mu'$ term in the emitted flux terms does not mean that the voltage measured from the solar cell is increased m times but rather accounts for the increase in the energy of the emitted photons.

Conventionally, the inclusion of multiple carriers recombination processes as describe above is termed as Auger recombination, and corresponds to the thermodynamic limit for a multiple EHPs interaction in recombination [28]. Because of the similarity to Auger recombination (e.g., multiple electron hole pairs are generated from a single recombination event) or inverse impact ionization, the MEG detailed balance calculations are considered to include Auger recombination. However, there are in practice multiple differences between such a thermodynamic process and measured Auger processes, including radiative emission and faster generation rates from the proposed multiple EHPs process compared to the rate of conventional bulk Auger recombination [82],[84].

Overall, Auger mechanism in equation (4.1) to (4.5) and [25]-[28] is the thermodynamic limit term; conventional Auger coefficients typically include other multiple carrier interaction and would have different Auger coefficients, leading to higher recombination [43],[84]. Further discussion of QY in MJMEG has explained in Appendix C.

4.3.2 Spectral Splitting in MJMEG Solar Cells

A key difference between a conventional MJ and a MJMEG solar cell is that the quantum yield can exceed unity. In a single junction MEG solar cell, the ideal maximum QY can be high, and the highest efficiencies assume QY over 800%. For the case of a BB spectrum, the theoretical QY can be arbitrarily high, as the spectrum contains at least some photons with an energy many times the bandgap. The maximum QY is lower for the terrestrial AM0 or AM1.5 spectra, which have a defined upper energy limit. In this case, the maximum QY is determined by the bandgap of the solar cell. For example, with bandgap of 0.5 eV, the maximum QY for the AM1.5 spectrum (in which the highest energy photon is 4.42 eV) is 800%; for an absorber material bandgap of 1.0 eV, the maximum QY is 400%.

In a MJMEG solar cell, unlike a single junction MEG, the maximum quantum yield is limited by the next higher bandgap. For example, if the lowest bandgap is 0.5 eV and the next bandgap is 0.9 eV, then the maximum QY is 1, and there is no theoretical increase from MEG processes. If the bandgap combinations are 0.5 eV and 1.2 eV, then photons with energies between 1.0 and 1.2 eV can generate two EHPs in the 0.5 eV solar cell. Overall, if there is a wide spacing between the bandgaps of the MJ device, then each solar cell in the stack can absorb photons with energies at least twice its bandgap.

Fig. 4.1 (b) shows this ideal calculated QY for a 4J solar cell with bandgaps of 0.31 eV(=E_{g1}), 0.93 eV(=E_{g2}), 1.86 eV(=E_{g3}) and 2.79 eV(=E_{g4}). Each junction has a possible maximum QY of 200%. In the absence of the higher bandgap junctions, the lowest bandgap junction could generate 3 electron hole pairs at photon energies above 0.93eV; however, no 0.93 eV photons strike the bottom cell since these are all absorbed by the solar cell above it.

The example shown in Fig.4.1 (b) explains why the number of junctions for which MJMEG solar cells demonstrate efficiency advantages is constrained. As the number of junctions increases, the benefit from MEG processes disappears because the maximum QY of any junction is limited by the photon energy resulting from the spectral splitting. Overall, to take advantage of MEG within each junction, the threshold of photon energy is two times greater than the lower photon energy ($E_{g(i+1)}>2E_{g(i)}$) assuming two EHPs per one photon.

4.4 Results

The author have calculated the limiting efficiencies of up to 4 junction MJ and MJMEG solar cells, for BB and AM1.5 spectra with either series or independent connections. For the AM1.5 spectrum, AM1.5G is used for the one-sun calculations and AM1.5D for the concentrated solar calculations. The efficiency contour plots for 2J solar cells are shown in Figs. 4.2-4.4 for BB and Figs. 4.5-4.6 for AM1.5 spectra; Fig. 4.7 gives the plot for 2 J and 3J solar cell at 900 suns. The BB simulation is included as they more clearly highlight the trends due to the absence of local maxima and minima caused by the absorption bands in the AM1.5 spectrum.

Tables 4.1 and 4.2 give the results for the optimum bandgaps for 2J to 4J MJ and MJMEG solar cells for one sun, and Table 4.3 and 4.4 show the results for full concentration. The series-connected case is the most relevant, as this typically implemented for monolithic devices. The optimum bandgap values and efficiency are also given for independent connections, particularly given increasing focus on spectral splitting approaches which can use independently connected solar cells.

Table. 4.1. Independent connection for MJ and MJMEG (BB and AM1.5G, One sun) where BB is the blackbody radiation and AM is the terrestrial spectrum, η is the maximum conversion efficiency © [2014 IEEE] [61].

		E_{g1} (eV)	E_{g2} (eV)	E_{g3} (eV)	E_{g4} (eV)	η (%)
2(MJ)	BB	0.98	1.87			42.9
	AM	0.94	1.73			46.1
2(MJMEG)	BB	0.68	1.76			47.8
	AM	0.70	1.82			48.8
3(MJ)	BB	0.82	1.43	2.25		49.3
	AM	0.93	1.42	2.08		52.0
3(MJMEG)	BB	0.60	1.49	2.13		51.3
	AM	0.69	1.24	2.25		52.8
4(MJ)	BB	0.72	1.21	1.77	2.55	53.3
	AM	0.70	1.13	1.64	2.25	56.0
4(MJMEG)	BB	0.54	1.31	1.81	2.47	54.1
	AM	0.70	1.13	1.64	2.25	56.0

Table 4.2. Series Connection for MJ and MJMEG (BB and AM1.5G, One sun), © [2014 IEEE] [61]

		E_{g1} (eV)	E_{g2} (eV)	E_{g3} (eV)	E_{g4} (eV)	η (%)
2(MJ)	BB	0.98	1.70			42.5
	AM	0.95	1.61			45.7
2(MJMEG)	BB	0.64	1.46			47.3
	AM	0.57	1.38			47.8
3(MJ)	BB	0.83	1.31	1.96		48.6
	AM	0.93	1.36	1.90		51.4
3(MJMEG)	BB	0.75	1.26	1.95		50.6
	AM	0.70	1.20	1.80		51.8
4(MJ)	BB	0.70	1.11	1.53	2.14	52.5
	AM	0.71	1.11	1.49	2.00	55.3
4(MJMEG)	BB	0.71	1.10	1.53	2.16	53.7
	AM	0.71	1.11	1.49	2.00	55.4

Table 4.3. Independent Connection for MJ and MJMEG (BB and AM1.5D, C=46200), © [2014 IEEE] [61]

		E_{g1} (eV)	E_{g2} (eV)	E_{g3} (eV)	E_{g4} (eV)	η (%)
2(MJ)	BB	0.77	1.70			55.8
	AM	0.70	1.53			60.4
2(MJMEG)	BB	0.46	1.42			66.7
	AM	0.47	1.34			68.3
3(MJ)	BB	0.62	1.26	2.10		63.7
	AM	0.70	1.34	1.99		67.9
3(MJMEG)	BB	0.45	1.38	1.95		69.7
	AM	0.49	1.44	2.08		72.2
4(MJ)	BB	0.52	1.03	1.61	2.41	68.7
	AM	0.51	0.95	1.49	2.13	72.6
4(MJMEG)	BB	0.42	1.27	1.95	2.38	72.4
	AM	0.48	1.38	1.82	2.33	75.2

Table 4.4. Series Connection for MJ and MJMEG (BB and AM1.5D, C=46200), © [2014 IEEE] [61]

		E_{g1} (eV)	E_{g2} (eV)	E_{g3} (eV)	E_{g4}(eV)	η (%)
2(MJ)	BB	0.76	1.54			55.5
	AM	0.70	1.44			60.4
2(MJMEG)	BB	0.42	1.25			66.6
	AM	0.46	1.22			67.9
3(MJ)	BB	0.60	1.14	1.82		63.2
	AM	0.69	1.17	1.74		67.7
3(MJMEG)	BB	0.40	0.95	1.72		67.1
	AM	0.35	0.94	1.58		68.7
4(MJ)	BB	0.49	0.93	1.38	2.01	67.8
	AM	0.54	0.98	1.39	1.90	71.8
4(MJMEG)	BB	0.36	0.81	1.30	1.97	69.8
	AM	0.53	0.97	1.37	1.88	71.9

The figures and tables show that in all cases the MJMEG hybrid solar cells have higher efficiencies than the corresponding MJ solar cell. Further, as expected from the QY discussion above, the efficiency benefit is larger when the number of junctions in the stack is smaller and under higher concentration. For example, Table 4.2 shows that for a 4J solar cell, the difference between a MJ and a MJMEG is 0.1% at one sun (AM1.5G), while it is 7.5% absolute for a 2J solar cell under concentration (AM 1.5 D) in Table 4.4.

While MJMEG solar cells have a higher efficiency, two additional advantages are the impact of MEG on the optimum bandgaps and the sensitivity of the efficiency to the bandgaps. The net effect is that it allows higher efficiencies with bandgaps in the range of existing III-V materials.

4.4.1 Impact on Optimum Bandgaps

The inclusion of MEG processes in a MJ solar cell has a relatively large impact on the optimum bandgaps, particularly junctions. The figures and tables show that the lowest optimum bandgap shifts to lower energies. This is best illustrated graphically in Figs 4.2 to 4.6, where in comparing each set of plots, the highest efficiency region illustrated by dark red shifts to lower energies. Similarly, Table 4.2 shows that a conventional 2J series connected solar cell has an optimum lowest bandgap of 0.95 eV under one sun AM1.5 conditions, whereas including MEG effects decreases the optimum bandgap to 0.57 eV. Including concentration further reduces the optimum band gap to 0.46 eV (Table 4.4).

The lower optimum bandgaps and its decreasing value with concentration are caused by two effects. These trends are consistant with single junction MEG results, which also have substantially higher efficiencies under concentration. This can be understood in that the optimum bandgaps for MEG processs are lower than those for a conventional device. However, for lower bandgaps, the difference between the quasi-Fermi level separation and the bandgap is a comparatively large fraction. As this difference is reduced with concentration, the propreties of MEG devices improve strongly with concentration.

A second cause of the reduced bandgaps is that MEG will only provide a benefit if the solar cell absorbs light of energy at least twice its bandgap. This has the effect of increasing the spread of bandgaps, particularly decreasing the lowest bandgap.

Even so, several of the MJMEG devices do not have MEG processes in all of the component solar cells. For example, from Table 4.3, the bandgap of the second junction of a triple junction

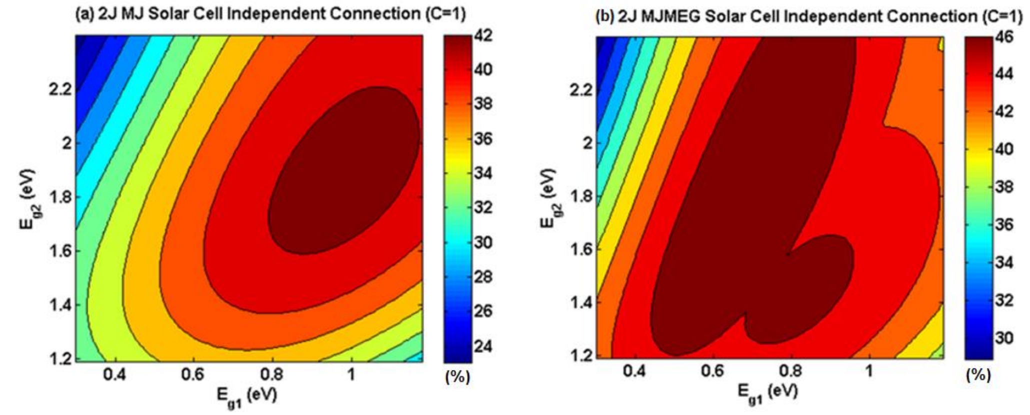

Fig. 4.2. Efficiency contour for a 2J MJ and MJMEG hybrid at one sun, BB spectrum independently connected © [2014 IEEE] [61].

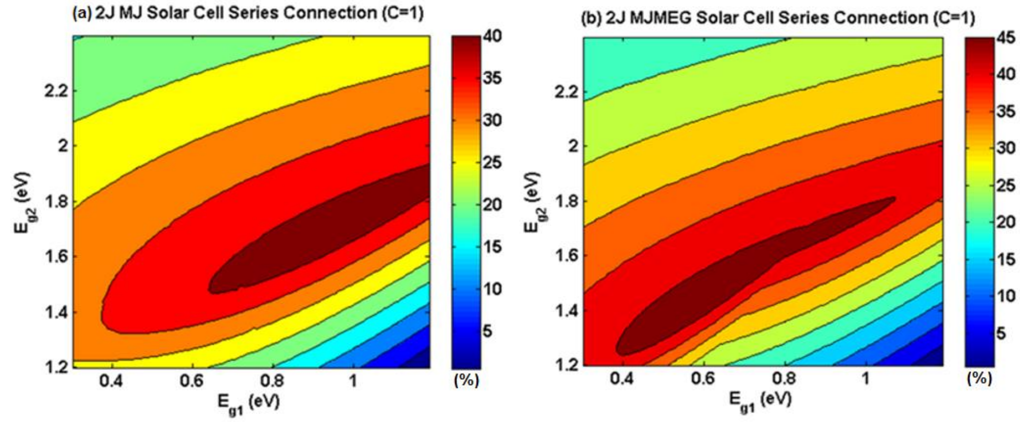

Fig. 4.3. Efficiency contour for a 2J MJ and MJMEG hybrid at one sun, BB spectrum series connected, © [2014 IEEE] [61].

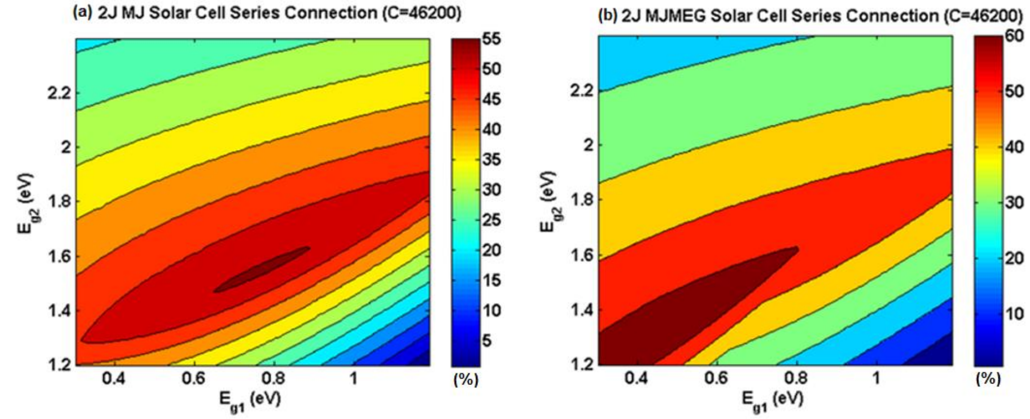

Fig. 4.4. Efficiency contour for a 2J MJ and MJMEG at maximum concentration, BB spectrum series connected, © [2014 IEEE] [61].

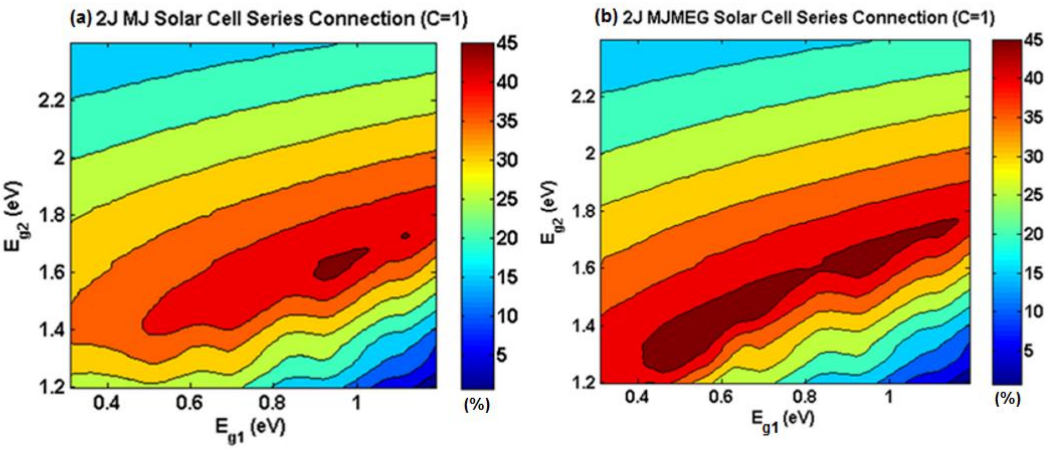

Fig. 4.5. Simulated efficiency contour for a 2J MJ and MJMEG hybrid at one sun, AM1.5G spectrum, series connected, © [2014 IEEE] [61].

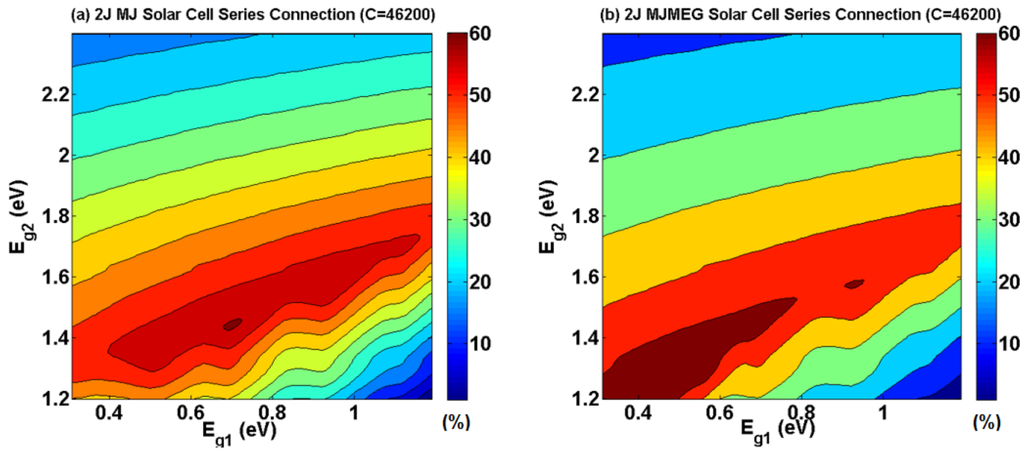

Fig. 4.6. Simulated efficiency contour for a 2J MJ and MJMEG hybrid at maximum concentration, AM1.5D spectrum, series connected, © [2014 IEEE] [61].

MJMEG is E_{g2}=1.38 eV for a BB spectrum. In order to benefit from MEG processes, the highest bandgap should be greater than 2.76 eV; however, this is higher than the optimum bandgap (=1.95 eV) of the third junction so the middle solar cell does not benefit from MEG processes.

4.4.2 Impact on Sensitivity of Efficiency to Bandgap

An important advantage of the MJMEG compared to the MJ solar cell is the increased flexibility in choosing bandgaps. The double junction MJMEG contour plots

(Figs 4.2-4.6) show this effect graphically; a 3J 3-dimensional plot displays similar effects (Fig.4.7). Figs 4.2-4.4 show that the optimum bandgap ranges somewhat to smaller bandgap values) and a second larger "tail" region at substantially lower values, particularly for the lowest band gap. Taken together, these two regions greatly expand the possible bandgaps which give high efficiencies.

Similar effects are seen for 2J solar cells under a AM1.5 spectra, although comparing the MJ and MJMEG the "tail" is less evident due to "ragged" contours resulting from the absorption peaks in the AM1.5 spectra. For example, Fig.4.5 shows that a conventional 2J device has an optimum bottom junction bandgap between 0.9 and 1.0 eV; the MJMEG device has an optimum bottom junction bandgap between 0.4 eV and 1.2 eV. Similar effects are shown in Fig. 4.6 under concentration, with optimum bottom band gaps ranging from 0.3 eV to 0.9 eV.

The contour plots and tables show several important features. The optimum bandgaps (Table 4.2 and 4.4 for series connected one sun and maximum concentration) show lower optimum band gaps. For example, under one-sun, the optimum bandgaps are 0.7 eV, 1.2 eV, and 1.8 eV for the MJMEG device. 0.7 eV fits well with the typically used Ge substrate.

In addition to the increased range of bandgaps, the efficiencies of two or three junction MJMEG solar cells under concentrated sunlight conditions are larger than conventional three or four junction MJ solar cells. For instance, the maximum conversion efficiency of double junction MJMEG solar cells under full concentration is greater than that of conventional triple junction MJ solar cells. From these results, the author expect that better efficiency MJMEG solar cells can be made with fewer junctions compared to conventional MJ solar cells when operated under concentrated conditions.

4.4.3 The Discussion of 2J and 3J MJMEG Devices under 900 Suns

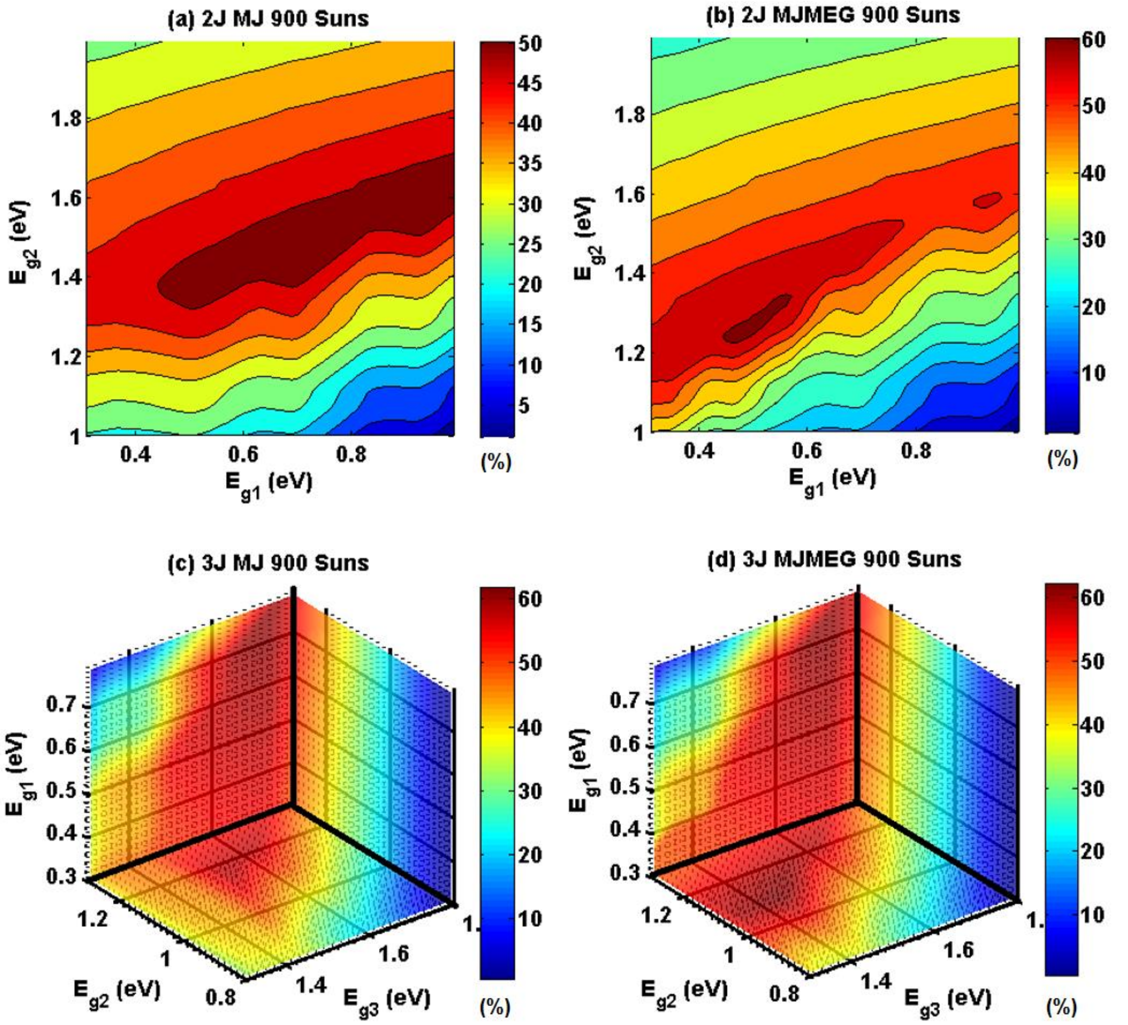

Fig. 4.7. Simulated efficiencies of series-connected 2J(=(a),(b)) and 3J(=(c), (d))MJ and MJMEG solar cells under 900 suns. E_{g1} and E_{g2}, E_{g2} and E_{g3} and E_{g3} and E_{g1} planes are used to plot in Fig.7 (c) and (d) © [2014 IEEE] [61].

As an example with moderate concentration, the author calculate efficiencies for both 2J and 3J MJ and MJMEG devices under 900 suns with the terrestrial spectrum and display the results in Fig. 4.7. Fig. 4.7 (a) and (b) present results for 2J cells. The maximum efficiency is 60.9% with optumum bandgaps of 0.47 eV(=E_{g1}) and 1.24eV (=E_{g2}) in 2J MJMEG devices, changed from the optimum values of 2J MJ cells (0.7(=E_{g1}) and 1.44 eV(=E_{g2})) with 54.3%). These optimum MJMEG bandgaps are well matched with InAs (bottom junction) and Si or InP (top junction).

3J MJ and MJMEG device results are highlighted in Fig. 4.7 (c) and (d). At concentration levels approaching 1000X, the plots in Fig. 4.7 (d) show efficiencies of 60% for cells with bandgaps which are lattice matched to InP; lattice matched device structures for 4J cells can also be fabricated with efficiencies close to optimum. For example, for a 3J MJMEG, potential materials include InAs (=0.36 eV)/ AlGaSb (=1eV)/ and AlAsSb or AlSb (=1.6eV) to give a maximum theoretical efficiency of 59.3%. Another approach using InP can show a good efficiency (54.7%) with InGaAs (=0.65eV)/ InP(1.34 eV)/AlAsSb or InAlAs (=1.9eV). These materials are significant since they allow optimum 3J and 4J monolithically grown solar cells using materials (e.g., InP and InAs) for which MEG phenomenon have been shown by ultrafast transient absorption measurements [83],[84]. The material selection for the bottom junction is especially critical if one is to achieve good carrier confinement in the quantum dots necessary for efficient MEG.

4.5 Conclusion

Hybrid solar cells combining multijunction solar cells with MEG to enhance the entire performance of multijunction solar cells offer higher theoretical efficiencies and a broader material space. Importantly, these efficiencies can be achieved with a maximum MEG QY of 200%, a range which has been experimentally demonstrated. Specific advantages include a broader material optimum bandgap space, allowing the use of lattice matched bandgaps. For example, under maximum concentration a 2J MJMEG solar cell with lattice matched materials has a higher theoretical efficiency than a 3J solar cell either with ideal band gaps. At 900X concentration, a 3J MJMEG on a Ge substrate with lattice matched materials can reach efficiencies over 50%. Furthermore, moving the optimum bandgaps to lower values allows the inclusion of MEG process into 3J and 4J solar cells with lattice matched materials on InP substrates with ideal or close to ideal efficiencies.

CHAPTER 5

LIMITING EFFICIENCY OF SILICON BASED NANOSTRUCTURE SOLAR CELLS FOR THIRD GENERATION SOLAR CELLS

5.1 Introduction

In chapters 3 and 4, the author has discussed the advantages of both MEG and MJMEG solar cells based on detailed balance calculated efficiency limits and has considered optimum material combinations. In this chapter, the author focuses on MEG and MJMEG solar cells with silicon. The theoretical efficiencies of these MEG and MJMEG cells are enhanced given both a smaller threshold energy and an ideal step like quantum yield (QY) [31],[32].

Current research extracting the QY from terahertz pump-probe measurements shows a linearly increasing QY up to 300% [19]. Colloidal PbSe [29], PbS [29], InN [84], InAs [43] or Silicon [44] quantum dots (QD) experimentally demonstrate carrier multiplication.

Nanostructures such as QDs and nanowires provide deep carrier confinement due to both relaxed momentum conservation rules and slow carrier cooling rate in discrete energy levels [31],[32]. Therefore, silicon nanostructures can be regarded as having a direct bandgap even if bulk silicon is an indirect band material [44].

Although the theoretical conversion efficiency of MEG solar cells is improved, there is still a relatively large amount of solar energy that does not convert to an electrical current due to thermalization losses. Thus, tandem or multijunction solar cells are a better alternative to efficiently capture the wide-range of the solar spectrum [85].

Multijunction solar cells are composed of selected bandgap materials to manage the wide range of the solar spectrum [76]. Incorporating silicon MEG into multijunction solar cells will give further great advantages by generating multiple electron and hole pairs (EHP) [60].

However, making a silicon nanostructured MJMEG solar cell has a critical issue with compatibility with other semiconductor materials because, silicon bandgap is 1.12 eV) and a limited maximum QY (=300%) under the terrestrial spectrum. Therefore, silicon nanostructures have to be used as an upper junction within a double junction MJMEG and the materials for the bottom junction that maximize the MEG effect are limited due to lattice mismatch considerations with silicon.

In this chapter, the author will present an efficiency model for Si nanostructured MEG and MJMEG solar cells and will discuss (1) detailed balance limit calculations of silicon MEG solar cells including non-idealities and (2) the thermodynamic limit of double junction MJMEG solar cells (MJMEGSC) with silicon nanostructures. © [2011 IEEE] [86] (see Appendix B)

5.2 Theory

5.2.1 The Importance of Silicon Material**s**

Selecting materials for MEG solar cell can help to improve the nanostructured solar cells. The properties of silicon MEG solar cells experimentally depend on the threshold energy that it will give a guide about how MEG solar cell fabricated well. Its theoretical expectation can be tested by the MEG detailed balance theory including non-idealities such as the variation of threshold energies. Silicon is a represented material due to the fist observation of carrier multiplication materials even in a bulk-type solar cell. Further, silicon still has the highest world record of single junction solar cells. Thus, using nano-structures will provide large benefits to improve entire properties of MEG solar cells due to excellent quantum confinements.

Theoretically, from the non-ideal QY simulation in section 3.3, the variations theoretical efficiency of PbSe (E_g=0.7 eV) with changing threshold energy is larger than silicon (E_g=1.12 eV) under the concentrated-sunlight. Thus, the experimental situation will be the same. Therefore, the silicon nanostructures are better selections of materials for MEG solar cells because of less sensitive to change of threshold energies.

In the near perfect condition, the theoretical approach of Si MEG is important to expect the optimum quantum confinements. Also, the controlling size of nanostructures give great effects such as effective bandgaps or better light absorptions to improve the characteristics of nanostructured solar cells.

5.2.2 The effective bandgap of silicon nanostructure

The size of the QDs affects the performance of MEG solar cells due to the shift in effective bandgap energy. From references [87]-[90], the Delerue model describes the effective bandgap change due to dot size based on a linear combination of atomic orbitals (LCAO) approach. The corresponding equation for silicon as a function of dot diameter, d (nm), is given by reference 88.

$$\text{Effective } E_{g,Si} \ (\text{eV}) = 1.12 + \frac{3.98}{d^{1.36}} - \frac{0.19}{d} \tag{5.1}$$

The corresponding effective bandgap as a function of dot diameter according to equation (5.1) is plotted in Fig. 5.1 below.

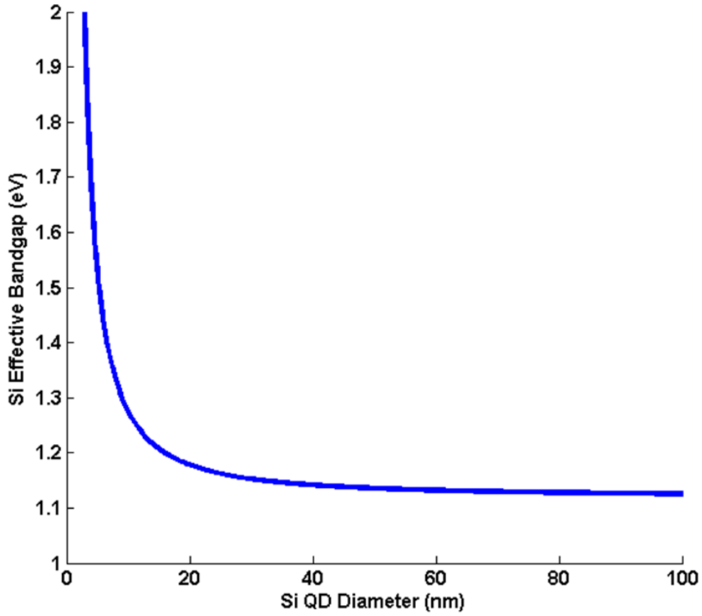

Fig.5.1. The effective bandgap as a function of diameter for Si QDs © [2013 IEEE] [86].

Table 5.1 shows the effective bandgaps for 4 different diameters of silicon QDs considered in the present work. The effective bandgap is inversely proportional to the size of the QD, and its threshold energy will determine the properties of MEG solar cells.

Table 5.1. The effective Si QD bandgap vs diameter © [2013 IEEE] [86].

Diameter (nm)	∞	15.9	8.9	6.5	5.2
Bandgap (eV)	1.12	1.2	1.3	1.4	1.5

From Table 5.1, the author has selected 1.2 eV effective bandgap to maximize the characteristics of Si MEG solar cell and it's the detailed information is discussed in section 5.3.1.

5.2.3 Silicon MEG

The relationship between the effective bandgap of Si nanostructures and size offers the ability to determine the properties of the MEG solar cell. Detailed balance limit equations (5.2) to (5.5) are applied to calculate the theoretical efficiency based on the QY including non-idealities. The relevant equations for MEG are repeated here from the previous chapters. The ideal QY is given by a step function

$$\text{ideal } QY(E) = \begin{cases} 0 & 0 < E < E_g \\ m & m \cdot E_g < E < (m+1) \cdot E_g \quad m = 1,\ 2,\ 3, \ldots \\ M & E \geq M \cdot E_g \end{cases} \tag{5.2}$$

where m is the number of multiple EHPs generated, M is the maximum number of EHPs, E_g is the band gap, and E is the photon energy.

From the experiments of QY extraction, the actual QY is better described by a linear increase after E_{th}. Thus, the modified non-ideal QY is described by

$$\text{non ideal } QY(E) = \theta(E, E_g) + A\theta(E, E_{th}) \cdot \left(\frac{E - E_{th}}{E_g}\right) \tag{5.3}$$

where θ is the heaviside step function, A(=1) is slope of the linearized QY, and E_{th} is the threshold energy.

$$\phi(E_1, E_2, T, \mu) = \frac{2\pi}{h^3 c^2} \int_{E_1}^{E_2} \frac{QY(E) \cdot E^2}{\exp[(E - \mu)/kT] - 1} dE \tag{5.4}$$

$$\begin{aligned} J = {} & q \cdot C \cdot \int_{E_g}^{E_{max}} QY(E) \cdot \Gamma(E)\ dE \\ & + q \cdot (1 - C \cdot f_s) \cdot \phi(E_g, \infty, T_C, 0) - q \cdot \phi(E_g, \infty, T_C, \mu) \end{aligned} \tag{5.5}$$

where ϕ is the particle flux given by Planck’s equation at temperature T with a chemical potential μ(=q·QY(E)·V) in the photon energy range between E_1 and E_2, h is Planck’s constant, c is the speed of light, while μ and μ_{MEG} are the chemical potential of the single junction and MEG solar cell. Here, V is the operating voltage, k is the Boltzmann constant, J is the current density of the solar cell, q is the charge of an electron, C is the optical concentration, f_S is the geometry factor (=1/46200), E_g is the bandgap energy, T_C is the solar cell's temperature (=300K), E_{max} (=4.428 eV at 280 nm wavelength) is the highest photon energy of the terrestrial spectrum, and $\Gamma(E)$ is the converted terrestrial spectrum from ASTMG 173-03.

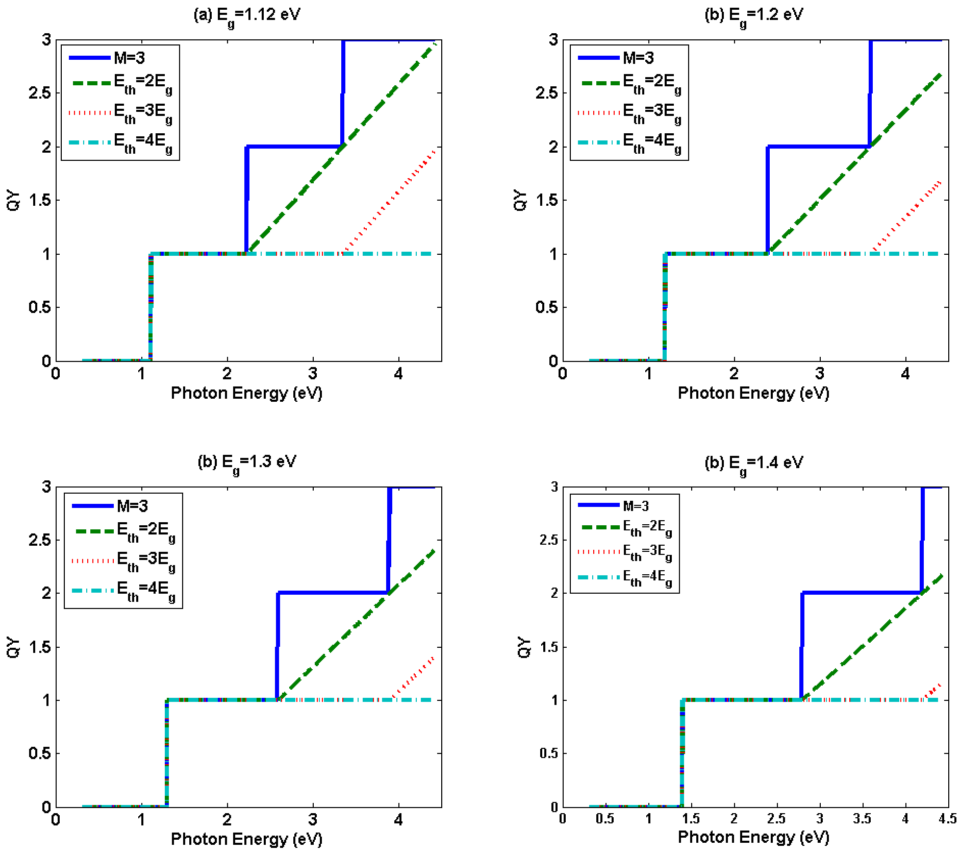

Fig. 5.2. The QY and photon energy of silicon QD, The maximum value of ideal QY is 3 and changes the delayed E_{th} as $2E_g$, $3E_g$ and $4E_g$. (a) E_g=1.12eV, (b) E_g=1.2 eV, (c)E_g=1.3 eV and (d)E_g=1.4 eV © [2013 IEEE] [86].

Fig.5.2 describes the ideal and non-ideal QY of silicon as a function of the effective bandgap and threshold energy. Under ideal QY conditions, even though the QY can increase infinitely, the solar photon flux at high photon energies is negligible so that QY is limited to two or three ($M \leq 3$). On the contrary, the non-ideal maximum QY depends on the threshold energy and reduces with increasing E_{th}. Thus, with increasing effective bandgap of the silicon QDs, the maximum non-ideal QY is decreased. And, Table 5.2 summarizes the simulation results based on Fig. 5.2 in section 5.3.1.

5.2.4 MJMEG Solar Cells with silicon QDs

The efficiency of MEG solar cells with silicon nanostructures is limited by the maximum ideal QY (=3 or 300%) under terrestrial spectrum conditions. A more efficient way to overcome thermalization losses is utilizing multijunction solar cells with concentrators resulting in increased photo-generated current of each cell.

For the MJMEGSCs, one has to consider the relationship between QY and spectral splitting to achieve non-overlapping QY and to maximize the MEG effect of each layer of the MJMEGSCs.

The basic assumption of MJMEGSCs is that every layer has carrier multiplication or MEG [60]. However, the net MEG effect of each layer depends on the QY interacting with spectral splitting. For instance, the top junction of a 2J MJMEGSC shows relatively high QY because there is no blocking layer to absorb the high energy photons [60].

The maximum QY of the bottom junction is limited. Fig. 5.3 describes how the maximum QY depends on the bandgaps of each junction within 2J MJMEGSCs.

First, it presumes that bulk silicon or silicon QDs are used for the top junction material to obtain the appropriate maximum carrier multiplications. Then, choosing possible materials for the bottom junction can be flexible to have the maximum QY. The effective bandgap of Si for the top junction is determined by the size of the QDs or nanostructures. The simulations determine the optimum bandgaps and corresponding QYs under both ideal and non-ideal QY conditions. Fig.5.3 (a) and (c) show QY vs. photon energy for the optimum bandgaps derived from the ideal QY with and without concentration. Also plotted in (a) and (c) are the corresponding non-ideal QYs for these same bandgap materials. Fig.5.3 (b) and (d) show QY vs. photon energy for the optimum bandgaps derived using the non-ideal QYs with and without concentration and again also displays the ideal QYs for comparison. These results are discussed in more detail in section 5.3.2. It is obvious from Fig.5.3 that the more step-like ideal QY will increase the photo-generated current and theoretical efficiencies compared to the non-ideal QY.

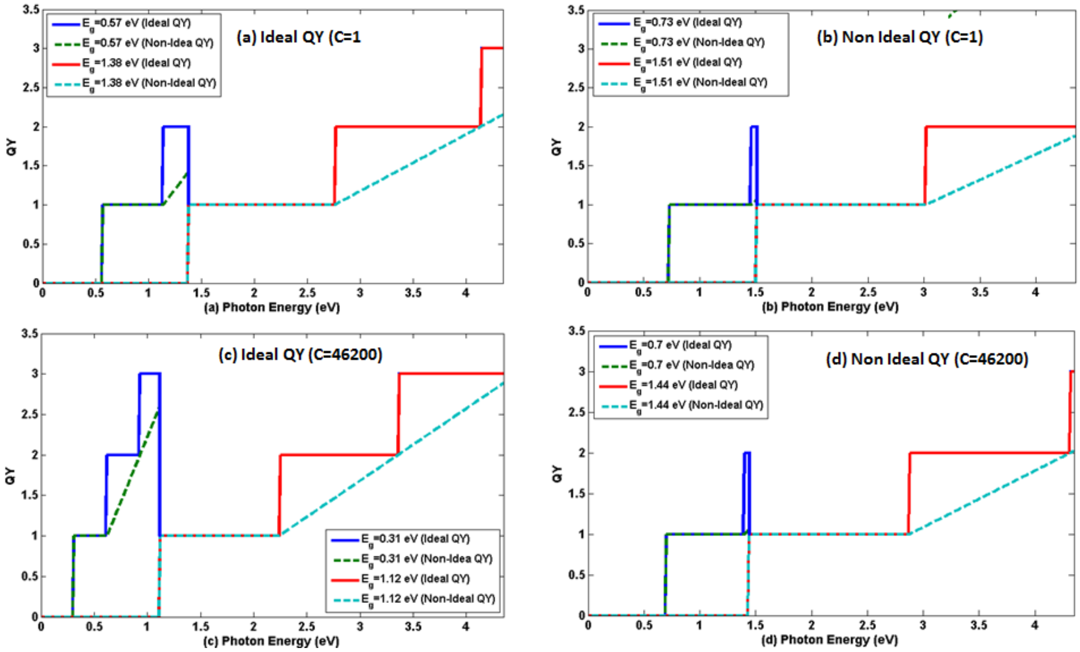

Fig. 5.3. The spectral splitting of double junction-MJMEG solar cells. The maximum QY depends on its bandgaps of each junction (a) and (b) are under one sun illumination, (c) and (d) are under full concentration (C=46200).
© [2013 IEEE] [86].

5.3 Results and discussion

5.3.1 Silicon MEG solar cell

Using the QYs in Fig.5.2, the author obtains the maximum theoretical conversion efficiency under one sun illumination for fixed M=3 and varying threshold energies for four different effective bandgap materials, with the results shown in Table 5.2.

Table 5.2. The efficiency of Si MEG ideal QY and non-ideal QY under one sun (ASTMG 173-03) where is M is the maximum QY and value of E_{th} is for M=3 © [2013 IEEE] [86].

	1.12 eV	1.2 eV	1.3 eV	1.4 eV
M=3	41.8	40.0	37.9	36.6
E_{th}	1.12 eV	1.2 eV	1.3 eV	1.4 eV
$2E_g$	36.6	35.6	34.4	34.2
$3E_g$	33.5	33.3	33.1	33.3
$4E_g$	33.3	33.3	33.1	33.1

For the ideal QY (M=3, E_g=1.2 eV), the theoretical efficiency of the ideal and non-ideal QY cases give quite different results. For the ideal QY (M=3, E_g=1.2 eV), the theoretical efficiency of a Si MEG is over 40.0%, decreasing with increasing effective bandgap. For the non-ideal QY, the maximum conversion efficiency is strongly dependent on both effective bandgap and threshold energies. Table 5.2 shows that the non-ideal QY drops the efficiency from 41.8% (ideal QY) to 36.6% when E_g = 1.12 eV, with a smaller drop for higher effective band gaps. For instance, if the effective bandgap of silicon is 1.4 eV based on a 6.5 nm diameter QD (Table 5.1), its theoretical efficiency with non-ideal QY and its corresponding maximum QY are (1) 34.2% and 2.17 (E_{th}=$2E_g$), (2) 33.3% and 1.16 (E_{th}=$3E_g$) and (3) 33.1% and 1(E_{th}=$4E_g$). Thus, as shown in Table 5.3, the cell efficiency only improves if E_{th} is near $2E_g$. If Eth is increased, the beneficial effects of MEG are greatly reduced. For $E_{g,effective}$=1.12 eV, the efficiency above E_{th} = $3E_g$ essentially saturates, and the difference between E_{th} = $3E_g$ and E_{th} = $4E_g$ is 0.2% absolute regardless of the value of the bandgap. Further, at these threshold energy ranges, the efficiency gains from the MEG process are relatively small compared to an ideal device without the MEG processes.

As shown in Fig. 5.1 and Table 5.1, the size of the QDs determines their effective bandgaps. With increasing Si QD size, the effective bandgap approaches the bulk-bandgap. Based on the detailed balance calculations presented here, the best performance for Si QDs is approached by making the QDs as large as possible while simultaneously preserving the beneficial effects of confinement in terms of lack of momentum conservation and hence an ideal threshold energy approaching energy approaching $2E_g$. Thus for subsequent simulations the author has selected an effective bandgap of 1.2 eV to maximize the effect of MEG.

Further, there are several ways to increase efficiency of MEG solar cells. One way is using concentration which enhances the conversion efficiency of solar cells by increasing both the light-generated current and the quasi-Fermi level separation. Another is realizing a more step-like QY vs. photon energy behavior. The current QY measurements in silicon show this possibility, that the shape of the QY is important in enhancing MEG solar cell performance by producing more light-generated current [91].

For this simulation, the author selects three maximum ideal QYs (M=1, 2, and 3) and one non-ideal QY with $E_{th}=2E_g$ and an effective $E_g=1.2$ eV to calculate theoretical cell efficiencies for a variety of concentration levels. The results are shown in Fig.5.4 and Table 5.3. For the ideal QY case, After M=2 the theoretical efficiencies vs. concentration are saturated since there is no further reduction of the thermalization loss. Therefore, in case of silicon nanostructures, 200% to 300% maximum QY is the critical point to optimize silicon nanostructured MEG solar cells.

Table 5.3. The efficiency of Si MEG with ideal QY and non-ideal QY with changing concentration where C is concentration. (Effective E_g=1.2 eV)

Si	C=1	C=100	C=1000	C=10000	C=46200
M=1	33.4	37.7	40.0	42.3	43.8
M=2	39.8	44.2	46.8	49.4	51.0
M=3	40.0	44.3	47.0	49.6	51.1
E_{th}=2E_g @M=3	35.6	39.7	42.1	44.6	46.2

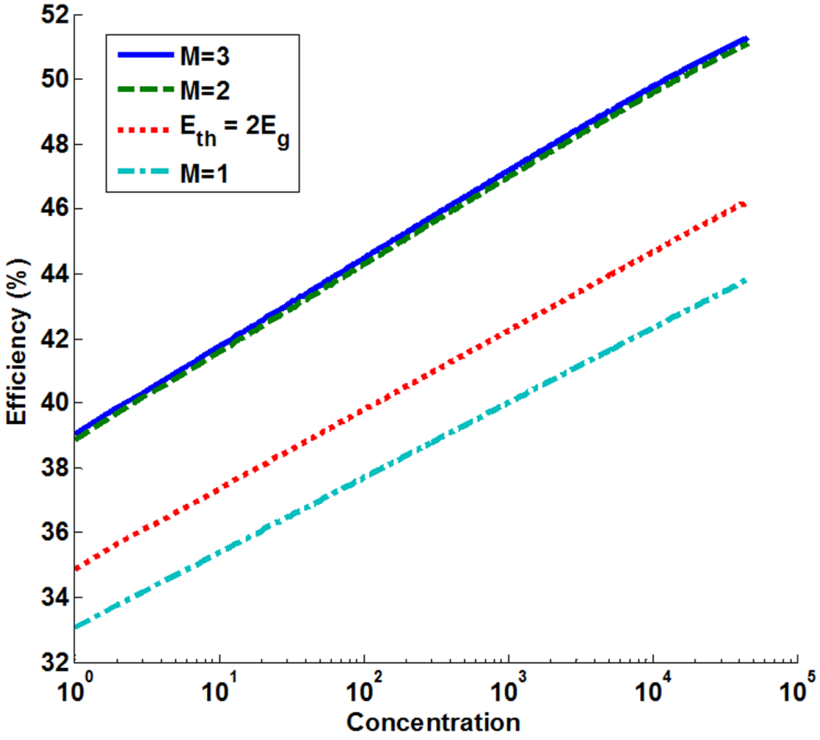

Fig. 5.4. The Efficiency VS Concentration of Si (E_g=1.2 eV) MEG under terrestrial spectrum with concentration. The concentration axis presents as log scale where M is the maximum QY © [2013 IEEE] [86].

As expected, the non-ideal QY results in cell efficiencies consistently below the ideal QY and its maximum conversion efficiency under full concentration is 46.2%. In a realistic concentration like 100 or 1000 suns, the expected efficiencies are 39.8% and 42.2% respectively.

5.3.2 MJMEG hybrid solar cells with Si QDs

In the previous section, MEG solar cells were analyzed theoretically and it was shown that when including either ideal or non-ideal QY, the calculated efficiency under one sun is not greatly improved. Therefore, the author has proposed double junction MJMEG hybrid solar cells as a better approach and has proceeded to determine their detailed balance efficiency limits.

The double junction MJMEG cell is assumed to have a top junction composed of silicon QDs for which the effective bandgap depends on QD size. The bandgap of silicon relative to the solar spectrum dictates that it should be used at the top junction in order to absorb photons that can effectively generate carrier multiplication. The simulations point out the significance of MEG effects within the bottom junction for maximizing QY. To maximize carrier multiplication, the optimum material for the bottom junction should have a small bandgap and a threshold energy close to two times the bandgap to prevent non-overlapping QY and match the solar spectra.

The ideal QY can always satisfy this condition due to its step-like nature. However, the optimum bandgaps calculated using the non-ideal QY are quite different because, in the non-ideal QY case, the maximum QY of the bottom junction is determined by the bandgap of the top junction. Thus, if the threshold energy of bottom junction is close to the top junction bandgap, the maximum QY is approximately 1 and the bottom junction will behave like a conventional multijunction solar cell. In order for the bottom junction to show a clear MEG effect the measured QY should approximate the ideal QY to maximize carrier multiplication.

Table 5.4. The double junction of MJMEG solar cells using Si QDs for upper junction where S is the series connection. H stands for MJMEG Hybrid solar cells. IQY is the ideal QY and NQY is the non-ideal QY © [2013 IEEE] [86]

C=1	E_{g1}(eV)	E_{g2}(eV)	η (%)	
2J (S,C)	0.5	1.12 (Si Bulk)	23.3	
2J (S,C)	0.75	1.52	44.2	
2J (S,H,IQY)	0.57 (InAs)	1.38 (Si QD, 6.9nm)	47.8	Fig 5.3 (a)
2J (S,H,NQY)	0.57 (InAs)	1.38 (Si QD, 6.9nm)	40.9	Fig 5.3 (a)
2J (S,H,IQY)	0.73 (Ge, InN)	1.51 (Si QD, 5.1 nm)	46.9	Fig 5.3 (b)
2J (S,H,NQY)	0.73 (Ge, InN)	1.51 (Si QD, 5.1 nm)	44.6	Fig 5.3 (b)
C=46200	E_{g1}(eV)	E_{g2}(eV),	η (%)	
2J (S,C)	0.5	1.12 (Si Bulk)	37.9	
2J (S,C)	0.7 (Ge)	1.44 (GaAs)	60.4	
2J (S,H,IQY)	0.31 (,InAs)	1.12 (Si Bulk)	69.4	Fig 5.3 (c)
2J (S,H,NQY)	0.31 (InAs)	1.12 (Si Bulk)	58.1	Fig 5.3 (c)
2J (S,H,IQY)	0.7 (Ge, InN)	1.44 (Si QD, 5.9nm)	63.8	Fig 5.3 (d)
2J (S,H,NQY)	0.7 (Ge, InN)	1.44 (Si QD, 5.9nm)	61.0	Fig 5.3 (d)

From Table 5.4, the optimum bandgaps calculated using the non-ideal QY are nearly the same as the conventional double junction MJ solar cells and show only slightly increased efficiencies. Therefore, the QY for MJMEG solar cells has to be similar to the ideal QY to maximize the MJMEG solar cells. For instance, the theoretical efficiency using the ideal QY for E_{g1}=0.58 eV and E_{g2}=1.38 eV is 47.8% under one sun and its efficiency is 6.9% higher than non-ideal QY. The simulated efficiency using the non-ideal QY for

E_{g1}=0.73 eV and E_{g2}=1.51 eV is 44.6%, whereas the calculated efficiency based on the ideal QY with same bandgaps is 46.9%.

Choosing the appropriate materials for silicon based double junction MJMEGs is important. There are various reports of QY extraction experiments for group II-VI, III-V and IV materials such as PbSe [29], PbS [29], InN [84] and InAs [43] and Ge [35] using ultra-fast transient absorption methods, observing impact ionization, and through simulations. Publications describe materials compatible with silicon nanostructures including Si on Ge, III-V nanostructures on silicon substrates and silicon hybrid solar cells [92]-[94].For instance, Ge (for the bottom junction) and Si QDs (for the top junction) can be a good approache. InAs or InN nanostructures on Si substrate have been mentioned for variety of applications for optoelectronic devices due to strain accommodation at the nanostructure surfaces [35],[92]. Finally, all-Si QD layers can tune light-absorption paths [95]. But, the all-Si QD method suffers from the relatively high bandgap of silicon (E_g=1.12 eV, E_{th}=2.24 eV) in the bottom junction preventing MEG and thus these cells display the nearly same theoretical efficiency as conventional multijunction solar cells from detailed balance calculations. For instance, the conversion efficiencies are 49.3% for MJ and 49.4% for MJMEG where E_{g1}=1.12 eV, E_{g2}=1.5 eV and E_{g3}=2.0 eV with one sun under terrestrial spectrum.

Therefore, the most promising way to realize MJMEGSC with silicon nanostructures is the combination with Ge or III-V materials. However, the lattice mismatches between Si and these other materials need to be overcome for optimum current-matched multijunction solar cells.

5.4 Conclusion

In summary, the author has investigated the effect of the threshold energy of Si multiple exciton generation solar cells on conversion efficiency through detailed balance calculations including quantum size effects. In general, a smaller threshold energy and ideal step like QY are important in realizing conversion efficiencies greater than the one junction limit. Quantum dots have a size–dependent effective bandgap. Thus, controlling both QD size for its effective bandgap and threshold energy is very important in maximizing the efficiency of MEG based solar cells, which the author demonstrates through the MEG detailed balance calculations for varying Si QD diameters reported here. MJMEG is an alternative way to effectively manage the thermalization losses of hot carriers. The author has shown how the behavior of the QY of each junction is critical to maximize the effects of MEG and explained why silicon nanostructures for the top junction are ideal due to its maximum QY. The simulations identify a number of possible materials such as Ge, InN and InAs as suitable bottom junction materials.

CHAPTER 6

THE EXPERIMENTS OF SILICON NANOSTRUCTURE SOLAR CELLS

6.1 Introduction

Nanostructured solar cells utilizing quantum confinement effects to boost conversion efficiency are an attractive option to replace the current solar cell technology. Such nanostructure based cells are called "third generation" solar cells and development efforts so far are largely confined to research laboratories.

For last half-century, crystalline silicon solar cells have been at the forefront of the PV industry as a result of the success of commercial and academic research. Crystalline silicon solar cells in the laboratory reached 24.7% conversion efficiency in 1999 [8], and currently, commercial crystalline silicon PV devices show an average 20% conversion efficiency [96],[97]. PV devices with this range of efficiency are called first generation PV devices. The first generation solar cell is based on silicon wafers with texturing for light trapping and screen-printing to make ohmic-contacts [96],[98].

In these first generation PV cells, to obtain high conversion efficiencies, it is necessary to control the surface morphology to reduce the reflectance and improve the electrical performance. Typically, in third generation devices like multiple exciton generation solar cells, it is also significant to consider how to integrate it with appropriate nanostructures for obtaining good quantum confinements that MEG and increasing light-generated current.

In today's manufacturing of silicon solar cells much effort is focused on the processes to texture the silicon surface, the subsequent cleaning of that surface, and the deposition of a silicon nitride film [99]. MEG solar cells also have to focus on these issues to improve the entire properties even if there are carrier multiplications. Therefore, optimizing and controlling these processes is challenging since the final electrical performance depends on both the material qualities and fabrication methods. Certainly, it increases the cost of silicon PV modules due to additional purifications of the surface of the silicon wafers [96]-[98].

Recently, silicon heterojunction with intrinsic thin-layer (HIT) solar cells have appeared as novel structures with high conversion efficiencies (24.7% and 25.6%) [10],[100]. Intrinsic amorphous silicon (α-Si) shows good passivation characteristics on a clean single crystal silicon surface and these cells achieve high open circuit voltages [101]. However, HIT cells still require texturing and cleaning of the single crystal silicon surface and their performance is very sensitive to the nature of that surface upon which the α-Si is deposited.

By depositing amorphous silicon at the silicon nanostructured solar cells, the author will discuss the effects of this approach for the future silicon PV cells.

In this chapter, it will describe the fabrication and measurements of both optical and electrical properties of a future generation silicon nano PV cells. This experiment is an initial attempt at fabricating silicon nanostructured solar cells with electron-beam lithography (EBL) and future work aimed at MEG solar cells. This project was a joint effort with Mr. Green as part of the 2013 National Nanotechnology Infrastructure Network Research Experience for Undergraduates program [Christopher Green, NNIN REU, 2013] [102].(see Appendix. D)

6.2 Silicon Nanostructured Solar Cells

Silicon nanostructured solar cells are recently developed PV cells using quantum dots or nanowires [97],[103],[104] to increase the effective conversion efficiency and to absorb light effectively. The effect of nanostructures is to make it possible to change the material properties such that indirect bandgap materials can behave like direct bandgap materials due to discrete energy levels inside quantum structures [105]. The effective bandgap is influenced by the size of nanostructures; i.e., the effective bandgap is inversely proportional to the size of nanostructures. Typical nanostructures have sub-100nm dimensions, much less than the wavelength of the light illuminating the solar cell making the shape, density, and composition of the nanostructures all factors in determining the optical absorption properties The management of these sub-wavelength dimensions can give a great impact for optimizing reflectance and these structures have unique features of separation of light absorption and carrier transport in the confinement of electrons in the quantum structures.

In general, MEG solar cells have to minimize the optical losses with modifications of processes including both passivation and anti-reflection coating for better quantum yield. In this project, the author focused on electron-beam defined front surface nanostructures only, passivated with a thin deposited amorphous silicon film and with no additional anti-reflection coating. The second benefit of a silicon nanostructured solar cell is the possibility to generate more than one electron and hole pair per one incoming photon by impact ionization, increasing the short circuit current. Even though the quantum yield extractions of nanostructures have proven the quantum yield can be over 100%, experiments do not show a great improvement of conversion efficiency likely due to surface effects and the use of low bandgap materials [52]. In other words, the MEG phenomenon is still controversial due to various different results of quantum yield extraction experiment by ultra-fast time resolved photo-luminescence.

Even if the short current is increased, to date nanostructured solar cells exhibit low conversion efficiencies with low fill factors and small open circuit voltages and it is clear much more research is needed to solve these issues [97]. These characteristics will be discussed in section 6.4.

This work focuses on the fabrication and measurement of both optical and electrical properties of a silicon nanostructured solar cell with an array of vertical nanopillars patterned on the front surface of the silicon chosen as the type of nanostructure to be studied. Using electron beam lithography, the size and pitch of a masking layer is defined and the pattern transferred into the silicon substrate using dry etching. Initially, the diameter of the nanopillars was set at 100nm with 700nm spacing between nanopillars and the etch depth target was approximately 500nm. The cell has a backside diffused emitter and uses shadow mask defined metallization. The process is detailed in section 6.3.

6.3 Experimental Procedure

Fig. 6.1 is the process flow of fabricating silicon nanostructured solar cells. These silicon nanostructure solar cells are fabricated by n+ doped back-side junction of p-type 300 µm thickness of silicon wafers with p-α-Si/i-α-Si and aluminum contacts. The process flow and hence the later results were constrained by the availability of a tool which was delayed in getting up and running.

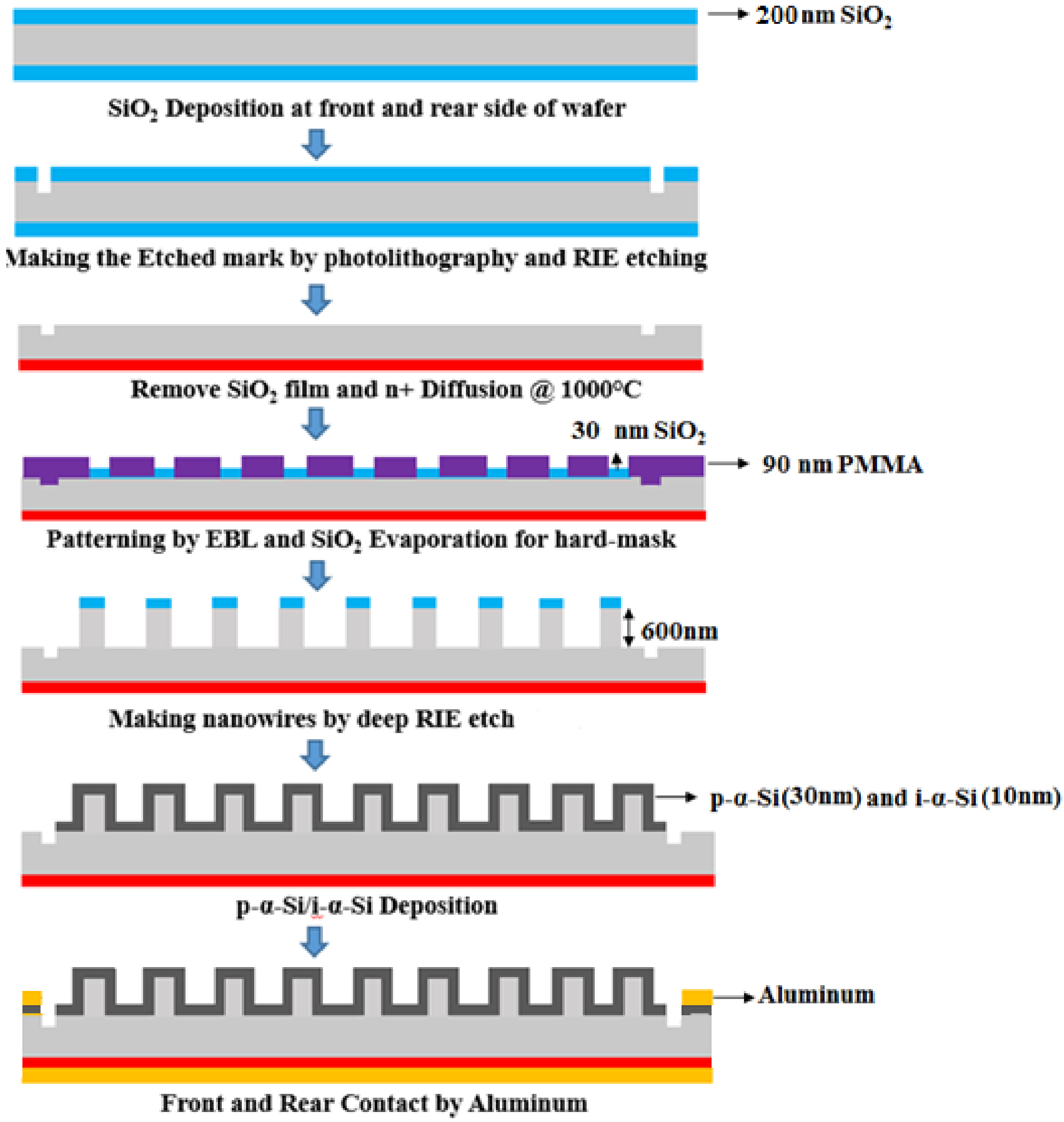

Fig. 6.1. The experiment flows of silicon nanostructured solar cells

First, after 200 nm of SiO_2 deposition of front and back side wafers at PECVD (Oxford Plasma Lab 100), the front-side etched marks were defined by a photolithography process (OAI Aligner). After developing photoresist, 200nm of SiO_2 and the 1µm depth of etched marks on silicon substrate are consecutively formed by reactive ion etching (RIE, Oxford Instrument Plasmalab 80+). These marks are used for next processes of Aligners and electron beam lithography (EBL).

Then, the both side of SiO_2 layers are removed by Buffered Oxide Etchant about 10 min to completely eliminate the remaining oxide film on the silicon wafers. And, to make a diffusion mask, the front side of silicon wafer was coated by SiO_2 by PECVD (Oxford Plasma Lab 100) again.

The next step is n+ diffusion for back-side of wafers at 1000°C for one hour and annealed about 7 hours to make a junction in the rear side of wafers. This process is supported by the diffusion furnace of 'Center for Solid State Electronics Research (CSSER)

90nm thickness of PMMA was coated on the front-side of wafers for EBL process. 100nm diameter openings are patterned by EBL equipment (JEOL 6000F/S) in CSSER. The distance between of nanostructures is about 700nm and the entire die size is small at 1mm × 1mm due to write time limitations. Then, 30nm thickness of SiO_2 is deposited with electron beam evaporation (LESKER #3 at CSSER) followed by liftoff of the PMMA to make oxide hard masks for the silicon etching.

The nanostructures or nanowires are etched by a Surface Technology Systems inductively coupled plasma (STS ICP) system using the SiO_2 hard masks. Highly anisotropic nanowires with 600nm height were formed using the Bosch process, which consists of alternating cycles of etchant using sulfur hexafluoride (SF_6) and polymer deposition from octaflourocyclobutane (C_4F_8). This method inherently creates scalloping on the sides of the nanowires. This nanostructures are displayed in Fig. 6.2.

A passivation and contact layer consisting of 10nm intrinsic i-α-Si and 30nm of p-α-Si was deposited on silicon nanostructures using PECVD (P-5000, Solar Power

Laboratory). The effective diameter of silicon nanostructures is increased to 180nm due to the deposition of these amorphous silicon films.

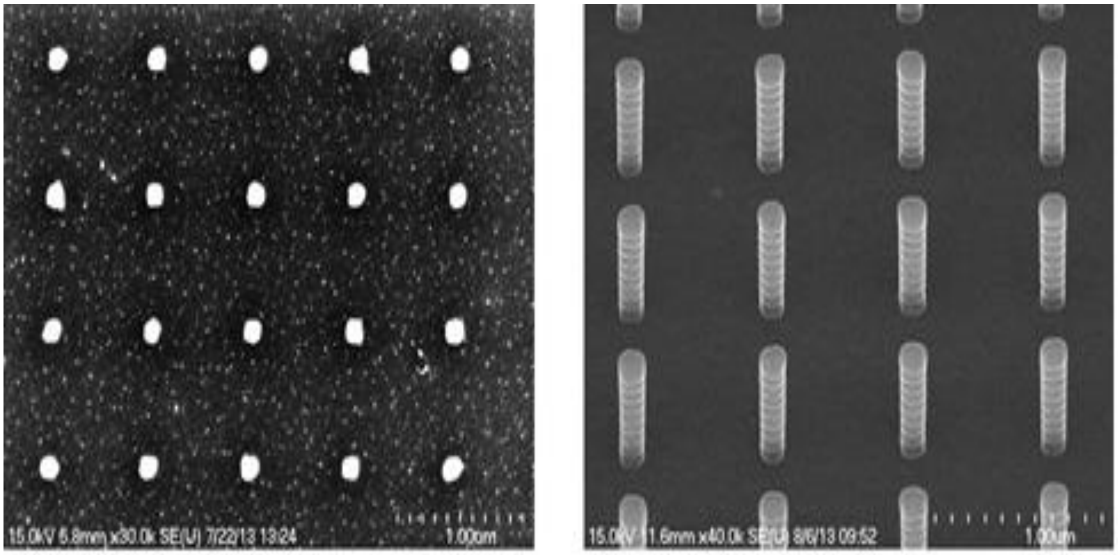

(a) Before etching

(b) Si Nanostrucures

Fig. 6.2. The fabrication of silicon nanostructures where (a) is the SEM image for deposition of 30nm thickness SiO_2 (b) is the image for silicon nanostructures after deep RIE etching [Christopher Green, NNIN REU, 2013] [102].

An electron beam evaporation tool, LESKER III at CSSER, was used to deposit 200nm of aluminum (Al) on the front and back sides of the wafer. A shadow mask was aligned on the front side of the wafer during deposition to prevent the base contact metal from covering the nanowires.

While measuring the electrical properties of this solar cell, non-alloyed Al contact on p-type amorphous silicon layer could not give data. Therefore, the wafers were placed in an oven to allow Al to diffuse through the passivation layer without compromising the amorphous nature of the layer.

6.4 Results

Both the optical reflectance and electrical performance under illumination were measured for the nanostructured cells and comparisons made to control devices processed without nanostructures fabricated on the same substrate. Even though this experiment results cannot provide good information for MEG solar cells, the light-generated current is increased due to properties of nanostructured solar cells and it will have more supplementary works to study of nano-PV cells for MEG.

6.4.1 The Electrical Characteristics

Electrical measurements were made on a probe station with illumination provided by a halogen lamp approximately calibrated to provide AM1.5 illumination. Only the small nanostructured region of the cell (1mm×1mm) is illuminated since the surrounding region is masked by the thick base contact aluminum metal, but the cell electrical area is considerably larger, with obvious negative effects on Voc. The control cell is identically processed, except no nanowires are etched in the illuminated region. Fig. 6.3 and Table 6.1 are the summary of results.

Table 6.1. The electrical characterization results of silicon-nanostructured solar cells [Christopher Green, NNIN REU, 2013] [102].

	J_{SC} (mA/cm^2)	V_{OC} (V)	FF (%)	η (%)
Silicon Nano PV Cell	21.6	0.44	67.7	6.43
Control Device	14.1	0.42	55.5	3.48

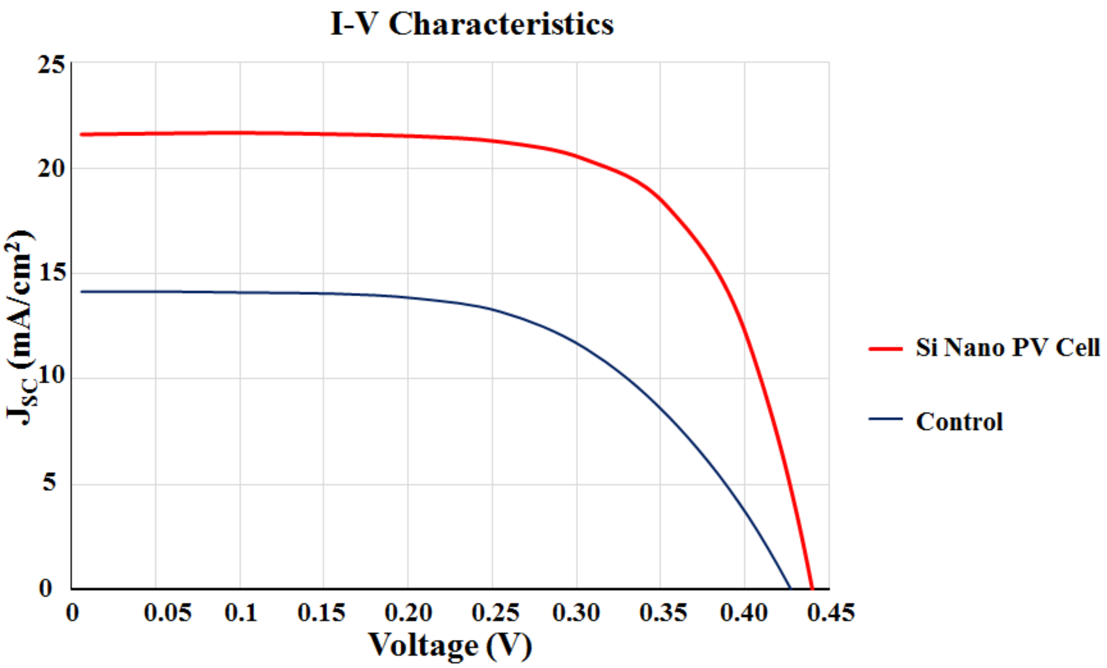

Fig. 6.3. The electrical properties of silicon nanostructured solar cell [Christopher Green, NNIN REU, 2013] [102].

The current-voltage relationships in Fig. 6.2 also show a series-resistance issue from the and low fill factor for both the nano and control cell, which is thought to be due to the lateral resistance between the illuminated area and the front-metal contact. The p-type and intrinsic amorphous silicon passivation layers have very high sheet resistance and typically in the HIT solar cell indium tin oxide (ITO) is deposited on these amorphous silicon layers to reduce the series resistance, something which was not done for these devices. It is also possible that there is an aluminum to p-a-Si high contact resistance problem.

The performance could be further improved through optimization of the passivation technology. The etched nanostructures not only increase the surface area but are also likely to suffer from surface damage induced by plasma etching, both of which lead to rapid surface recombination. As long minority lifetime is needed which requires minimizing all recombination sites and thus one needs to find optimum etch conditions to minimize the surface damage and establish post etch cleans that enable the deposited amorphous silicon films to effectively passivate the surfaces of the nanostructures.

The experimental results of silicon nanostructures have several drawbacks due to low open circuit voltage and its low fill factor. Actual diffusion process has conducted at entire rear side of wafers that even though the size of silicon nanostructures area is 1 mm × 1 mm, the entire diode size is 10 mm × 10 mm so that the current from nanostructures to the junction is laterally flowed instead of vertical flowing. Generally, an open circuit voltage of this solar cell is defined in equation (6.1)

$$V_{OC} = \frac{k \cdot T}{q} \cdot \ln(\frac{J_{SC}}{J_O} + 1) \tag{6.1}$$

Where V_{OC} is an open circuit voltage, k is the Boltzmann constant, T is an solar cell temperature (=300 K), q is the element of charge, J_{SC} is the short circuit current and J_0 is a recombination current

And, J_{SC} is a factor from light generation under 1 mm × 1mm of nanostructure area and J_0 is a recombination current which depends on diode area (=10 mm × 10 mm) of solar cell. Therefore, an asymmetric dimension of solar cell area destroys the entire open circuit voltage.

To resolve this issue, the n+ diffusion should be localized to prevent the lateral flow of current. Thus, even though the actual size of diode is 10 mm × 10 mm, in this dissertation, the experimental results have conducted with an assumption of 1 mm × 1mm area under light illumination where it is shown in Fig 6.4.

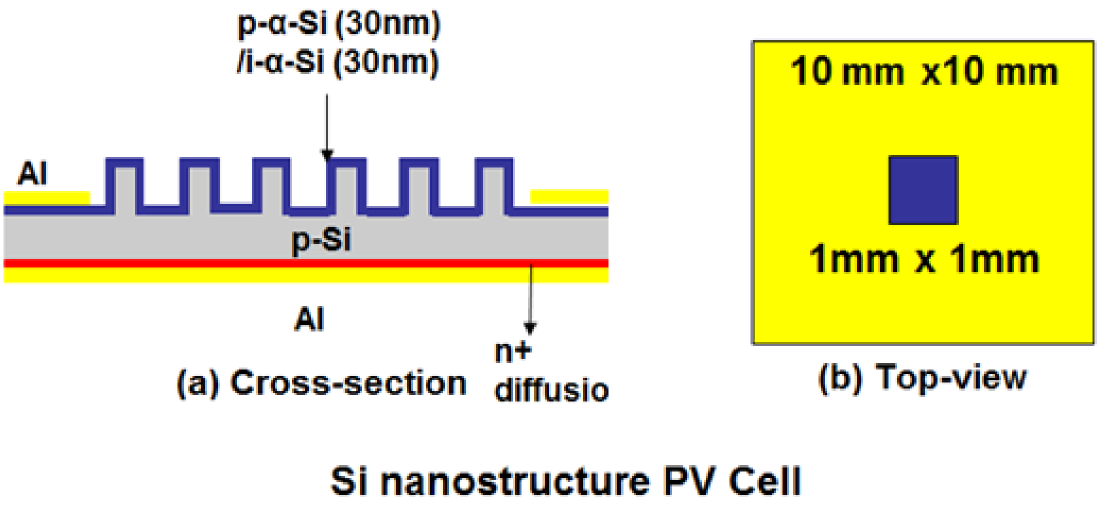

Fig. 6.4. The cross-section and top-view of silicon nanostructured solar cells.

Furthermore, to make better silicon nanostructured PV cells, the front side of nanostructured area and the rear side of should be same. Or, the front-contact with p-α-Si has to remove and should replace to the all rear contact or should deposit ITO for making contact with Al. And, it is also necessary to localize diffusion to directly collect the generated carriers from nanostructures. Thus, the current can flow vertically from nanostructures to the junction of backside wafers.

6.4.2 The Optical Characteristics

Reflectance measurements were taken of silicon nanostructured patterns using the Filmetrics F40 microscope with conventionally textured silicon and bare silicon as a references. The results in Fig. 6.5 plot the reflectance vs. wavelength from 400 to 850 nm.

The reflection characteristics of a conventionally textured silicon solar cell are better than the silicon nano PV cell and a polished silicon surface. The Si nanowire PV cells show an optical resonance from 685nm to 750nm wavelength due to the periodic nanostructures and its minimum reflectance (=2.5%) is lower than the textured silicon solar cell. Other regions show higher reflectance which is not unexpected due to the wide spacing of the periodic structures of silicon nanostructures. In other words, the high-reflection region represents bulk-silicon area and the optical resonance region is the nanostructured area having high-absorption.

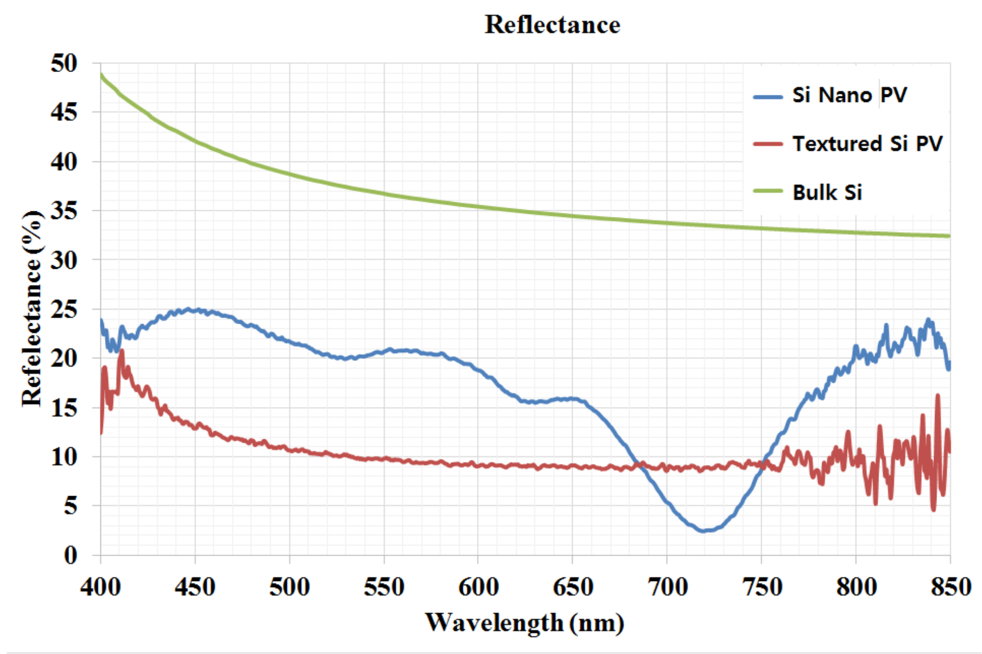

Fig. 6.5. The measurements of reflectance between silicon nanostructures PV cell and textured Si PV and Bulk or bare silicon solar cells [Christopher Green, NNIN REU, 2013] [102].

6.5 Conclusion

Initial experiments fabricating silicon nanostructured solar cells have been conducted. These nanostructured solar cells are fabricated by EBL and deep RIE process with thin amorphous silicon layers for passivation. To investigate light-trapping, the efficiency has measured under AM1.5 spectrum and shown that the short-circuit current of silicon nanostructured solar cell is higher than the reference cell. However, its open-circuit voltage is low due to a large parasitic diode area and the possibly the quality of the surface passivation. Furthermore, the optical reflectivity has been measured comparing polished silicon, a textured silicon solar cell and the nanostructured solar cell. One significant point is that the silicon nanostructured solar cell has an optical resonance at 700 nm where its reflection is lower than the textured solar cell, presumably due to the periodic nature of the nanowire array.

Further research is needed to optimize the fabrication process increasing the number of silicon nanostructures to provide higher absorption and enhance the conversion efficiency for future MEG solar cells. And, studying the physical parameters such as diameter, spacing, and structure on absorbance must be performed to allow for optimization of nanowire structures. Furthermore, a study of passivation would help to improve both optical and electrical characteristics.

CHAPTER 7

LIMITING EFFICIENCIES OF INTERMEDIATE BAND SOLAR CELLS WITH TANDEM CONFIGURATION

7.1 Introduction

Tandem (or multijunction) solar cells present high experimental conversion efficiencies over 40%, and have the highest efficiency record [4], [106]. For instance, the recent champion record of triple junction tandem solar cell is 44.4 percent (InGaP/GaAs/InGaAs, 302 suns) with using inverted metamorphic structures [6]. Furthermore, the conversion efficiency of a four junction tandem solar cell has approached to 44.7% [11]. Thus, the experimental world record of tandem solar cell will approach to near 50%.

However, due to material imperfections in the materials used in tandem solar cell, it is still necessary to minimize defects by using novel growth technologies [107]. Appropriate material selections are also important to enhance the properties of tandem solar cell with acceptable lattice mismatches. Therefore, a key challenge is to find the appropriate trade-offs between number of junctions, materials which allow low defect concentration in order to improve the overall efficiency of tandem solar cells.

Intermediate band solar cells (IBSC) have three optical transitions due to the presence of an intermediate band (IB) by adding another energy level inside the bandgap. The theoretical conversion efficiency is 63.2% with full concentration which it is similar to the value of a triple junction tandem solar cell [15], Currently, InAs/GaAs or InAs/GaSb systems are researched in order to fabricate IBSCs [108] but experimental results show low efficiencies, around 20%, showing there are still challenges and a need for further improvements in quantum dot systems to make IBSC [109].

Integrating the IBSC concept with a tandem solar cell (IBTSC) shows a large impact because of the three carriers transitions in an IBSC [110]-[113]. Theoretical conversion efficiencies of double junction (2J) IBTSC can be similar to the calculated efficiency of 5 or 6 junction tandem solar cells under concentrated sunlight. Thus, 2J IBTSC provides the large improvement in the theoretical efficiency for the same reduced number of junctions. The same efficiency as using large number of junctions in conventional tandem solar cells and be reached in an IBTSC with a smaller number of junctions.

The spectral splitting between the junctions is the key to determining optimized physical parameters for each junction to avoid spectrum overlap between layers. One approach to spectral splitting is to assume that the 6 effective band gaps in the two IBSC structures can take any value, and that light will automatically find its optimum band gap. This is used in [110] and [111]. In this work, the requirements on spectral selectivity are reduced, and it is assumed that the top IBSC contains the top three effective band gaps. While it is still assumed that within each IBSC spectral selectivity occurs, spectral selectivity is not assumed between the two IBSC structures. This is implemented by dividing the incident solar radiation into two regions to clearly define the two bandgaps for barrier materials, and then each bandgap has properly ordered of three sub-bandgaps: E_{CI}, E_{IV}, and E_g.

The advantage of 2J IBTSC is that there is increased flexibility in the choice of optimized materials for the efficient absorption of photon energies and the relaxation of strain due to lattice mismatch. Therefore, the author has searched appropriate materials from group IV, III-V materials. In addition to the constraints placed on the optimum band gap, and additional constraint on material selection is introduced by the band offsets, which give rise to either a Type I or Type II quantum well or QD system. In type I in quantum dot (QD) structures the electrons and holes are confined in the same quantum well systems. But, type II structures show an indirect transition of an electron and hole due to spatially separated with neighbor quantum well or different band alignment. In other words, holes are localized due to the valence band offset, similarly, electrons will have a potential barrier at the same location of valence band offset region. Because of different spatial separation in quantum wells between type I and type II, the wave-function at the conduction band in type II is not directly correlated with valence band offset.

In this chapter, the authors present detailed balance limit calculations for 2J IBTSCs under full concentration (= 46200) under blackbody radiation and examined candidate material combinations. This chapter is based on [113] in which the author has further discussed about the material selection of IBTSC. (see Appendix. E)

7.2 Theory

7.2.1 Detailed Balance Model of IBTSC

First, the author use the most of assumptions in both tandem and IB solar cells in [20],[75],[76]. Each junction uses the ideal perfect mirror to avoid spectral overlapping between neighbor junctions [13].

Due to (1) selectively absorbing photon energy in both IBSC and tandem solar cells and (2) the similar efficiencies between IBSC and 3J tandem solar cells, it is attractive to integrate both concepts to enhance the characteristics of IBSC by tandem configuration. General configurations of 2J IBTSC is shown in Fig.7.1 that 6 transitions of carriers should be spectrally separated.

The detailed balance equations of IBTSC are shown below from equation (7.1) to (7.6). Equation (7.1) and (7.2) are the generation rate and recombination rate of IBSC respectively.

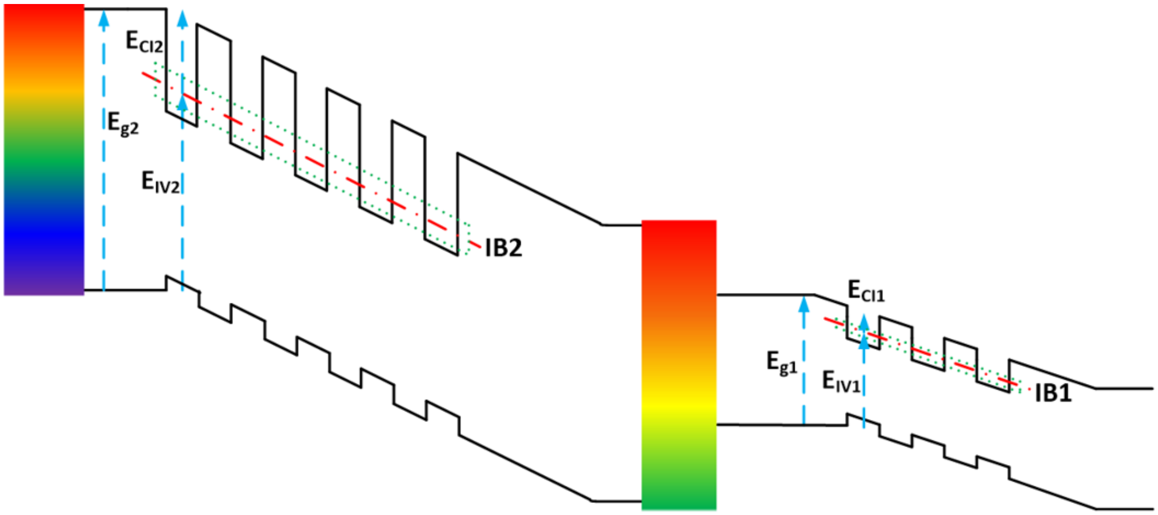

Fig. 7.1. The schematic of a tandem double junction IBTSC.

$$
\begin{aligned}
G_{E2,E1} &= f_S \cdot C \cdot \frac{2\pi}{h^3c^2}\int_{E_1}^{E_2}\frac{E^2}{\exp[E/kT_{SUN}]-1}dE \\
&+ (1-f_S \cdot C)\cdot \frac{2\pi}{h^3c^2}\int_{E_1}^{E_2}\frac{E^2}{\exp[E/kT_C]-1}dE
\end{aligned} \tag{7.1}
$$

$$
R_{E2,E1} = \frac{2\pi}{h^3c^2}\int_{E_1}^{E_2}\frac{E^2}{\exp[(E-\mu)/kT_C]-1}dE \tag{7.2}
$$

where G is generation rate and R is a recombination rate, f_S is a geometric factor (=1/46200) in this case, C is a sun's concentration (=1~46200), h is a plank constant, c is speed of light, E_1 and E_2 are energy states, k is a Boltzmann constant, T_{SUN} is a sun's temperature (=6000K) and T_C is an ambient temperature (=300K), μ is a chemical potential (=q·V) where V is an operating voltage.

The current density (J) of the i^th^ junction in the IBTSC is given by

$$J_{(i)} = q(G_{CV(i)} - R_{CV(i)} + G_{CI(i)} - R_{CI(i)}) \tag{7.3}$$

where subscript "i" is the number of junction (i=1,2,3…), subscript CV indicate the carrier transitions between the valence band (VB) and the conduction band (CB), and subscript CI indicates the carrier transitions between the IB and the CB.

Assuming no carrier extractions from IB can write in equation (7.4):

$$G_{CI(i)} - R_{CI(i)} = G_{IV(i)} - R_{IV(i)} \tag{7.4}$$

where subscript IV indicates the carrier transitions between the valence band (VB) and IB.

The chemical potential of IBTSC is the summation of voltages between (1) the IB to CB and (2) the VB to IB:

$$qV_{CV(i)} = qV_{CI(i)} + qV_{IV(i)} \tag{7.5}$$

Compared to the conventional tandem solar cell, each stack of the IBTSC has three different bandgaps which are $E_{g(i)}$, $E_{IV(i)}$ and $E_{CI(i)}$ as shown in Fig.7.1.

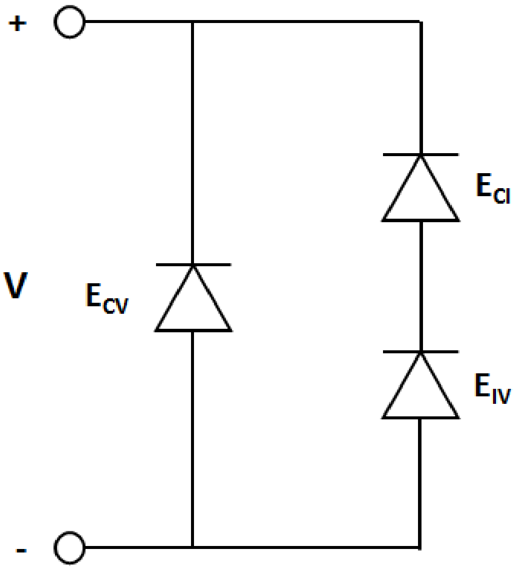

Fig. 7.2. The schematic of electrical circuit model of IBSC. It is composed of three diodes having bandgaps of E_{CI}, E_{IV} and E_{CV}..

Thus, it can show an equivalent electrical circuit model in Fig. 7.2. Two diodes, E_{CI} and E_{IV} are series-connected and these two diodes are parallel-connected with E_{CV}.

The IBTSC model requires careful accounting of the available photon flux vs. energy, as this will be quite different from that of the typical tandem cell. To calculate this, the solar spectrum is divided into two regions. In Fig.7.3 of section 7.2.2, $E_{hi(1)}$ is defined as the boundary point dividing the two regions which IBSC1 and IBSC2 are the spectrum ranges for bottom and top junction of the IBTSC respectively. After selecting $E_{hi(1)}$, it can set the proper order of sub-bandgaps can be set for each junction where $E_{CI1}<E_{IV1}<E_{g1}<E_{CI2}<E_{IV2}<E_{g2}$.

7.2.2 Solar Spectrum Splitting of Double Junction IBTSC

In tandem solar cells, a principle of solar spectrum splitting is that each layer uses an ideal perfect mirror to absorb appropriate incoming photon energy and other photons reflect the outside mirror [20]. Like tandem solar cells, IBTSC uses three light absorption paths of incoming photons for each junction including both a bandgap and two sub-photon energies (E_{CI} and E_{IV}). Further, t also uses an ideal mirror to absorb appropriate energy of light.

Fig.7.3 describes the solar spectrum splitting for both tandem solar cells and IBTSC. Conventional tandem, IBSC, and IBTSC cells all achieve improves conversion efficiencies by selection of optimum bandgaps.

Below $E_{hi(1)}$, we consider the IBSC as the bottom junction of IBTSC. In other words, the incident photon flux will reflect above $E_{hi(1)}$ and the bandgaps of the lower IBSC (E_{CI1},E_{IV1} and Eg1) will have energies below $E_{hi(1)}$.

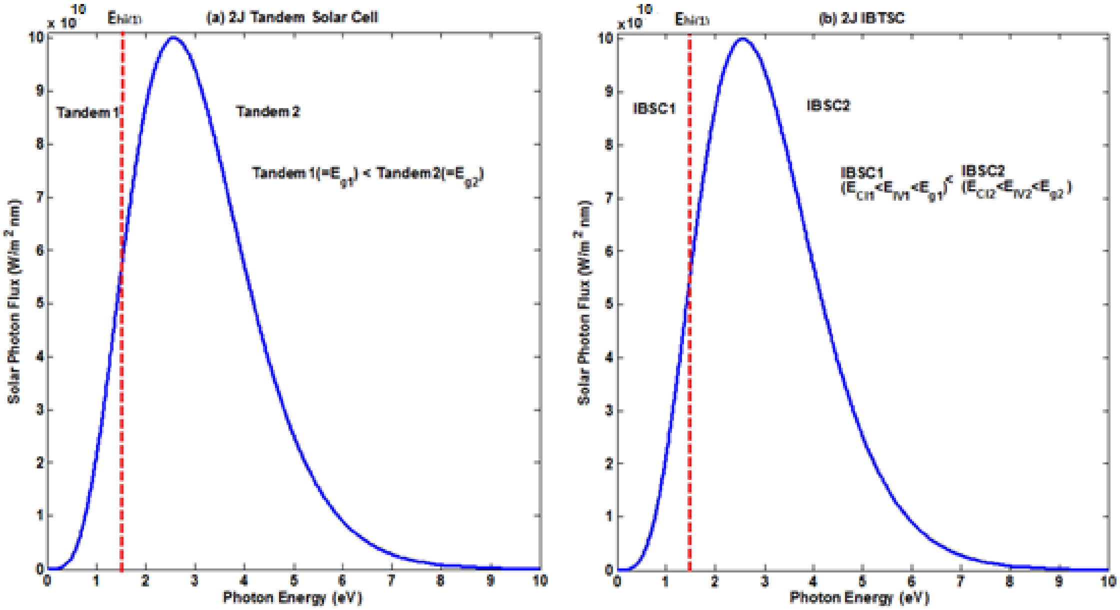

Fig.7.3. The spectral splitting of two regions for 2J IBTSC

For instance, if $E_{hi(1)}$ is 1.5 eV, the upper solar spectrum range can be considered as top junction IBTSC (=IBSC2) and below 1.5 eV range is for the bottom junction (=IBSC1).

The proper values of E_{CI1}, E_{IV1} and E_{g1} will be determined below 1.5 eV based on equation (7.4). In case of the next junction defined by $E_{hi(2)}$ as infinity, the proper range of E_{CI2}, E_{IV2} and E_{g2} will be determined between $E_{hi(1)}$ and $E_{hi(2)}$. The minimum value of E_{CI2} should be the same or higher than $E_{hi(1)}$ to avoid spectrum overlapping and maintain enough margin to extract carriers from the bottom junctions. If E_{CI2} is below $E_{hi(1)}$, there will be a range of spectrum overlapping between E_{CI2} and E_{g1}. Also, if $E_{hi(1)}$ is not properly chosen such that the difference between $E_{hi(1)}$ and E_{g1} can be small, the photo-current component for carrier extraction from VB to CB of bottom junction will be small or negligible. In other words, the dominant contribution is from the IB to CB so the entire effect of bottom junction in the IBTSC will operate as a two-junction series-connected tandem solar cell composed of E_{CI1} and E_{IV1}. Explicit separation of the solar spectrum is significant while designing multiple layers of IBTSC.

7.3 Results

After regarding all suggested parameters for simulations, the author present results of 2J IBTSC's theoretical conversion efficiencies and its optimum bandgaps under full concentration (=46200 suns). The results are compared with six junction tandem solar cells under full concentration. All collected data are displayed in (1) Fig.7.4 and Table 7.1 for double junction IBTSC and (2) Table 7.2 for six junction tandem solar cells.

7.3.1 The thermodynamic Limits of double junction IBTSCs

The maximum theoretical conversion efficiencies under full concentration in the series-connected IBTSC is 0.7% less than 6 junction tandem solar cells. $E_{hi(1)}$ is 1.19 eV and E_{g1} is 0.32 eV below $E_{hi(1)}$. The difference between $E_{hi(1)}$ and E_{g1} is important in determining the properties of the lower ICSC. If the difference between the two is small, then the number of photons in this energy range is also small, and hence the current is also small.

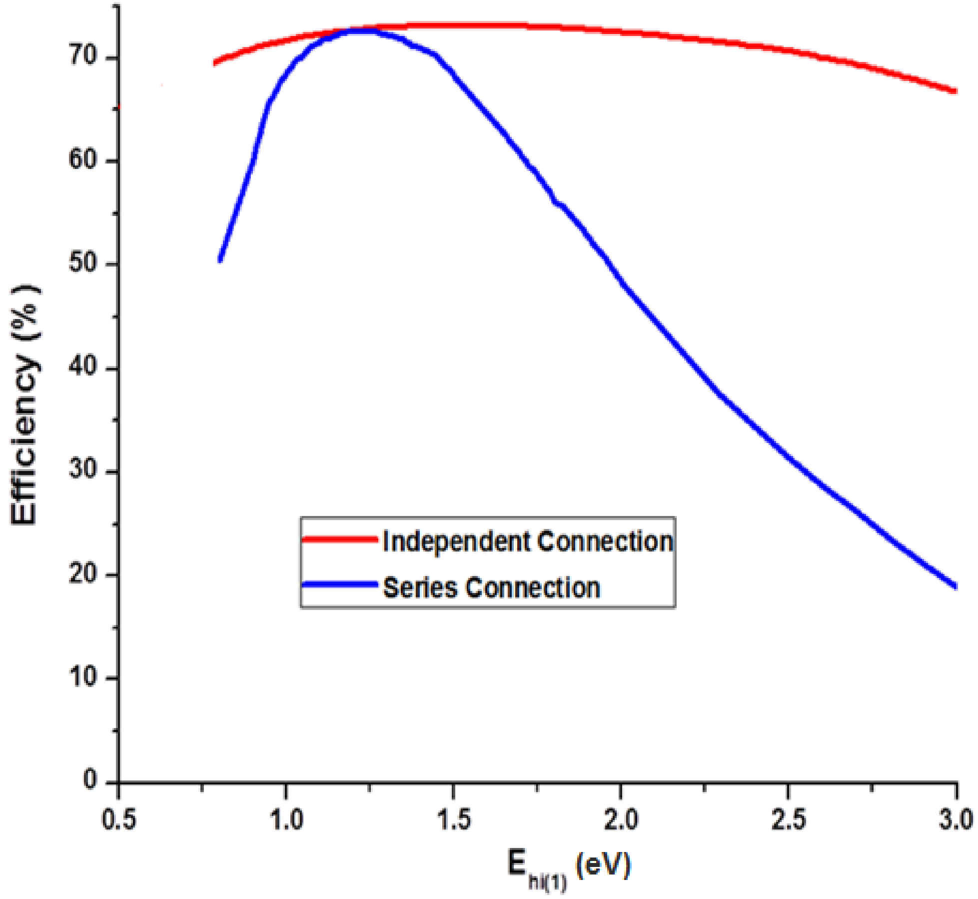

Fig.7.4. Efficiency vs. $E_{hi(1)}$ for double junction with an independent connection (red line) and a series-connection (blue line) under full concentration (J.Lee, [113],2012).

Table 7.1. The optimum bandgaps and maximum efficiency (η) of independent (I) and series (S) connected double junction IBTSCs under blackbody radiation with full concentration [J.Lee, [113],2012].

Conc		E_{CI1} (eV)	E_{IV1} (eV)	E_{g1} (eV)	E_{CI2} (eV)	E_{IV2} (eV)	E_{g2} (eV)	η (%)
46200	I	0.36	0.75	1.11	1.50	2.06	3.56	73.2
	S	0.21	0.66	0.87	1.19	1.75	2.94	72.7

Table 7.2. The optimum bandgaps and maximum efficiency (η) of six junction tandem solar cell under blackbody radiation where concentration (=Conc) is 46200 sun. [J.Lee, [113],2012].

Conc		E_{g1} (eV)	E_{g2} (eV)	E_{g3} (eV)	E_{g4} (eV)	E_{g5} (eV)	E_{g6} (eV)	η (%)
46200	I	0.40	0.78	1.16	1.59	2.11	2.86	74.4
	S	0.37	0.70	1.00	1.32	1.71	2.30	73.4

These results presume that the dominant carrier transition in the bottom junction IBTSC is from IB to CB and it is negligible from VB to CB.

The maximum theoretical efficiency (=73.2%) of independent-connected 2J IBTSC under full concentration is similar to a series-connected six junction tandem solar cells (=73.4%) as shown in from Table 7.1 and Table 7.2.

The material choices for independent connection can be also wide due to large bandgaps to compose QDs. Note that the bottom junction of the series-connected IBTSC requires a lower bandgap, an issue due to limited choices of low bandgap materials suitable for QD formation.

Next, the author discusses the material combinations for 2J IBTSC with the combination between independent and series-connections.

For concentrated sunlight, the results of 2J series-connected IBTSC are shown in Table 7.1. It shows that barrier materials near 0.9 eV are an appropriate choice for monolithic growth with GaN combination for 2J IBTSC. But, in the low bandgap materials with super lattice structure, hot carriers can easily escape at CB of bottom junction that can reduce the electrical properties of 2J IBTSC due to low carrier extraction margin from E_{g1}

to $E_{hi(1)}$, small confined states in QDs and dependence of temperature. Therefore, the light-generated currents are small not preserving the operating voltage of bottom junction IBTSC.

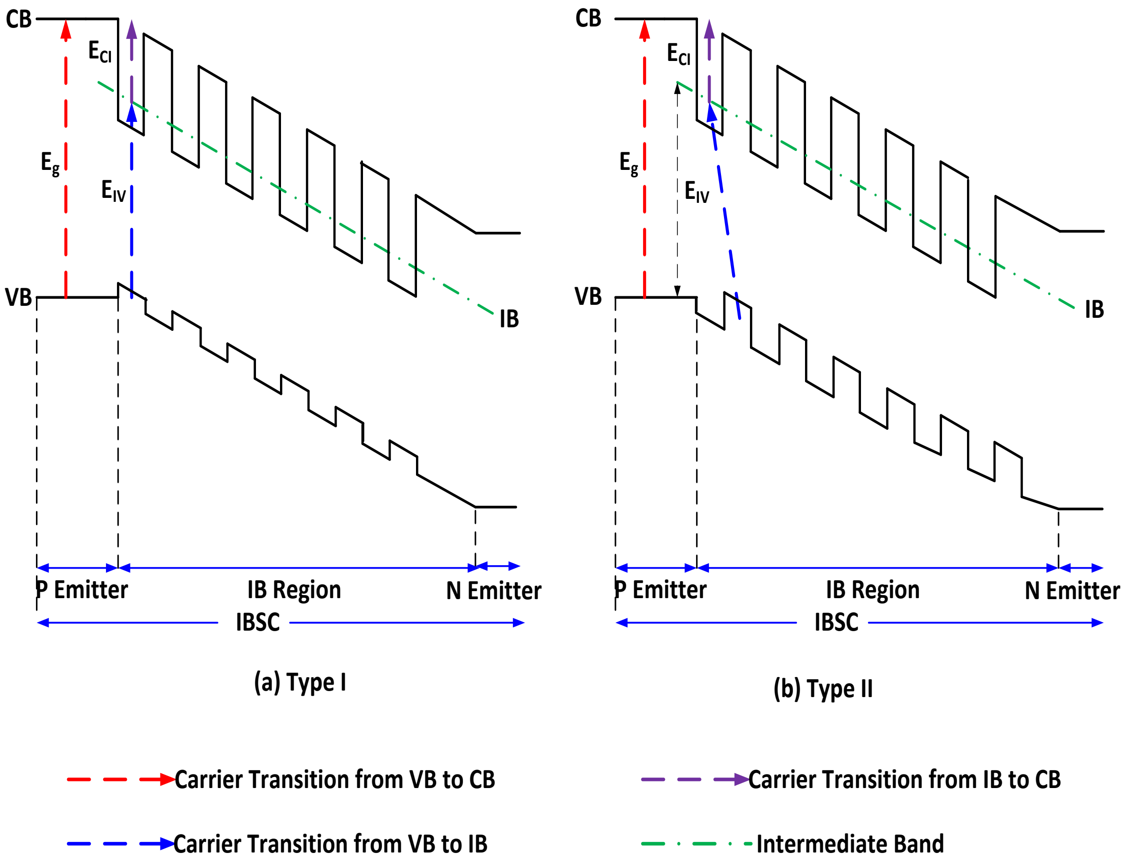
(a) Type I

(b) Type II

Fig.7.5. Two types of band structures for a double junction IBTSC where (a) is type I and (b) is the type II.

Type I or type II structures for IBTSC is displayed in Fig 7.5. The general IBSC band structure is type I structure. However, type I has drawbacks such as reducing photo-current due to different transition rates between (1) VB to IB and (2) IB to CB and decreasing open-circuit voltage because of VB offset due to localized bound states at VB [114].

Therefore, the type II is an alternative due to increasing both carrier life time and photo-current compared to type I structure. But, due to overlapping of wave-functions, the different absorption coefficient should regard between type I and type II.

7.3.2 Material Selection for IBTSC

Fig 7.4 and Table 7.1 show several ways to from 2J IBTSC such as (1) Si/Ge, III-V for bottom most junction and GaN related materials or wide-bandgap of II-VI for top junction of independent connection (IC) and (2) low bandgap III-V (for bottom junction) and high bandgap of III-V or II-VI (for top junction) for a series connection (SC).

III-V combinations are well-established approaches to compose IBSC. As well, II-VI material combinations are also good choices for top junction materials for broad choices.

In case of IC, an optimum bandgap of bottom junction is 1.11 eV which it is similar to Si, InGaAs, AlGaSb and GaAsSb. The author does not discuss the composition of mole fraction for optimum band gaps, since such calculations require assumptions about specific device parameters such as strain. Possible combinations are Si/Ge [115], InGaAs/InAs [116], AlGaSb/InSb [117] and GaAsSb/InAs [118] under the concentrated sunlight. In the top junction of IC, GaN/InGaN [119],[120] and AlGaN/InGaN [121] are good choices. And, II-VI compound semiconductor can give broad materials choices. For instance, ZnS (=3.7 V) [122] is wide bandgap materials and incorporating with Cr to make deep impurity levels photovoltaic devices.

For a 2J IBTSC, the optimum materials have several choices. First, the barrier material for bottom junction is near 0.9eV materials under concentration range. Possible combinations are InGaAs/InAs quantum dot or quantum well systems.

For the top junction materials, it should be matched with near 3 eV so that (1) III-Nitride and (2) II-VI ZnMgSe, ZnSSe [123] and ZnCdS with transition metal or hetero-structures are appropriate choices with considering of lattice mismatches.

7.4 Conclusion

A detailed balance of double junction IBTSCs has been developed to show the advantages of minimizing the number of junctions and to search for appropriate material combinations. The characteristics of two-junction hybrid IBTSC are similar to a theoretical conversion efficiency of six-junction conventional tandem solar cells. Because of the transition of three carriers, a single IBSC can show the properties of triple junction tandem solar cells. The author has discussed the material selections of 2J IBTSC with results of independent-connected and series-connected solar cells. In an independent connection of 2J IBTSC, the material combinations are Si/Ge for bottom junction and GaN/InGaN for top junction. But, in case of series-connection, materials for the bottom junction show 0.9 eV which it should be composed of low bandgap materials. And, due to 3 eV wide-bandgap barrier materials of top junction, there are various options to choose materials such as III-V Nitride and II-VI combinations.

CHAPTER 8

THE THERMODYNAMIC LIMIT OF INTERMEDIATE BAND SOLAR CELLS ASSISTED WITH MULTIPLE EXCITON GENERATION

8.1 Introduction

Intermediate band solar cells (IBSC) with quantum dots (QD) are a promising concept among third generation photovoltaic devices aimed for overcoming the single junction efficiency limit [12],[15]. By inserting another energy level inside the bandgap and assuming strong absorption of light through sub-paths, three carrier transitions are possible: (1) valence band (VB) to conduction band (VB), (2) VB to intermediate band (IB) and (3) IB to CB [15]. In equilibrium, the IB level occupancy is balanced by two transitions which are from VB to IB and from IB to CB [15]. The additional generated carriers in the CB contribute to the electrical current and the IBSC achieves a maximum theoretical efficiency of 63.2% due to absorption of photons with energy less than the bandgap [15].

After the IBSC concept was initially reported [15], subsequent research focused on (1) further developments of detailed balance theory of the IBSC [124],[125] and (2) possible candidate materials to build IBSC based on ab-initio calculations and bandgap engineering. Experiments have been conducted to make IBSC using III-V compound semiconductor materials such as GaAs/InAs or ternary material systems such as GaNAs and other combinations [126]-[131]. These experimental results demonstrate near or less than 20% efficiency cells [16],[132]-[135]. Recent experimental IBSC research proves the existence of two photon carrier generation by photoluminescence or electroluminescence [136],[137].

Theoretically, more advanced IBSC concepts have been proposed including both Auger generation at the IB and multiband cells with IBSC [138]-[144].

Currently, multiple exciton generation (MEG) has appeared as another promising third generation photovoltaic device approaches to minimize thermalization losses. MEG achieves carrier multiplication through impact ionization for while absorbing photons with energy greater than the bandgap energy [31],[32]. Typically MEG relies on the use of quantum dots, since electrons in the QD can remain excited longer than in bulk materials due to relaxed momentum conservation rules and slower carrier cooling processes [31],[32]. Many results show that the threshold energy should be closed to two times the bandgap to maximize the MEG effect and conversion efficiency [37],[45].

Integrating MEG and IBSC provides greater efficiency by reducing the thermalization loss [145],[146] and increasing the number of electron and hole pairs (EHP) generated while widening the range of acceptable semiconductor materials. Also, spectral splitting of IBSC offer to wisely managed input spectrum like tandem solar cells [15],[113],[147]. Thermalization losses in an IBSC with carrier multiplications are further reduced by dividing the solar spectrum and quantum yield with three optimum transitions [133],[139].

Both MEG and IBSC make use of low energy photons such that low bandgap materials offer a wide selection of materials.

In this chapter, the author introduces a thermodynamic limit model of IBSC assisted with MEG. The model calculates maximum theoretical efficiency and optimum bandgaps using novel detailed balance limit equations applied to the IBSC including the effects of QY and considers the possible carrier transitions between bands as determined by quantum yield and spectral splitting. The author will show calculated maximum efficiencies and optimum bandgaps of MEG effect with IBSC (MIBSC) under blackbody radiation and standard AM1.5 spectrum with both one sun and full concentration.

8.2 Theory

8.2.1 Detailed Balance of MIBSC

From the references [141], the Auger effect combined with an IBSC is implemented by the changing carrier multiplication probability and the absorption coefficient. In this chapter, the author here suggest a different way that the increased number of EHPs is determined by QY from three transitions in the IBSC including the definition of carrier multiplication. In MEG solar cells, the remaining photon energy can generate other EHPs by impact ionization or Auger generation is given by the QY.

$$\mathrm{QY(E)} = \begin{cases} 0 & 0 < \mathrm{E} < \mathrm{E_g} \\ \mathrm{m} & \mathrm{mE_g} < \mathrm{E} < (\mathrm{m}+1)\mathrm{E_g} \\ \mathrm{M} & \mathrm{ME_g} < \mathrm{E} < \infty \end{cases} \tag{8.1}$$

where m is the number of multiple electron hole pairs generated, M is the maximum number of electron hole pairs which are generated, E_g is the band gap, and E is the photon energy.

The detailed balance equations for the MIBSC are shown in (8.2), (8.3) and (8.4).

$$\phi(\mathrm{E_1,E_2,T},\mu_{\mathrm{MEG}}) = \frac{2\pi}{h^3c^2}\int_{E_1}^{E_2}\frac{\mathrm{QY(E)}\cdot \mathrm{E}^2}{e^{(\mathrm{E}-\mu_{\mathrm{MEG}})/kT}-1}\mathrm{dE} \tag{8.2}$$

where ϕ is the particle flux given by Planck’s equation for a temperature T with a chemical potential μ_{MEG} in the photon energy range between E_1 and E_2, h is the Plank's constant, c is the speed of light, k is the Boltzmann constant.

Equation (8.2) is a modified photon flux for the MEG solar cell and it depends on the difference between E_1 and E_2 to determine its QY. For instance, if QY of both the barrier and QD region is 1, MIBSCs will behave as conventional IBSC.

Equations (8.3), (8.4) and (8.5) are modified from the conventional IB detailed balance limit. Equation (8.3) is the photo-generated current of an MIBSC.

$$\begin{aligned} J = q \cdot \{ & [f_S \cdot C \cdot \phi(E_g,\infty,T_S,0) + (1 - f_S \cdot C) \cdot \phi(E_g,\infty,T_C,0) - \phi((E_g,\infty,T_C,\mu_{MEG,CV})] \\ & + [f_S \cdot C \cdot \phi(E_{CI},E_{IV},T_S,0) + (1 - f_S \cdot C) \cdot \phi(E_{CI},E_{IV},T_C,0) - \phi((E_{CI},E_{IV},T_C,\mu_{MEG,CI})] \} \end{aligned} \tag{8.3}$$

where f_S is the geometry factor (=1/46200), C is the concentration. E_{CI} is the transition from IB to CB, E_{IV} is the transition from VB to IB and $E_g(=E_{CV}=E_{CI}+E_{IV})$ is the transition from VB to CB, T_S is the temperature of the sun, and T_C is the temperature of the solar cell.

As also described in the previous chapter, from the IBSC theory, the intermediate band is isolated from the contact and there is no carrier extraction. Thus, the optimum intermediate band level is determined by the balance of transitions (1) VB to IB and (2) from IB to CB. Therefore, IB level should be set by equation (8.4).

$$\begin{aligned} & f_S \cdot C \cdot \phi(E_{CI},E_{IV},T_S,0) + (1 - f_S \cdot C) \cdot \phi(E_{CI},E_{IV},T_C,0) - \phi(E_{CI},E_{IV},T_C,\mu_{MEG,CI}) = \\ & f_S \cdot C \cdot \phi(E_{IV},E_g,T_S,0) + (1 - f_S \cdot C) \cdot \phi(E_{IV},E_g,T_C,0) - \phi(E_{IV},E_g,T_C,\mu_{MEG,IV}) \end{aligned} \tag{8.4}$$

And, the chemical potential of MIBSCs is given from equation (8.5) to equation (8.7).

$$\mu_{MEG,CV} = \mu_{MEG,CI} + \mu_{MEG,IV} \tag{8.5}$$

$$\mu_{MEG,CI} = q \cdot QY(E) \cdot V_{CI} \tag{8.6}$$

$$\mu_{MEG,IV} = q \cdot QY(E) \cdot V_{IV} \tag{8.7}$$

8.2.2 Carrier Transitions of MIBSC

IBSCs generate two electrons at the CB based on three transitions. The, IB is electrically isolated and has no carrier extraction. From reference [113], the conversion efficiency of the IBSC is similar to triple junction tandem solar cells.

If there is a MEG effect in the IBSC without the restrictions multiple EHPs (QY=2) and spectral splitting, the generated number of carriers in each transition is 2. For instance, if the QY is 2, (1) two EHPs are excited from VB to CB, (2) and two from VB to IB and (3) two EHPs from IB to CB. The total generated EHPs are four at CB due to relations between QY and spectral splitting. Thus, the procedure of generation of carriers of MIBSC with QY and spectrum splitting is shown in Fig.8.1. To generate carrier multiplication, the threshold energy (E_{th}) for the MEG effect should be two times greater than the bandgap so that the minimum threshold energy of $E_{th,CI}$ is $2E_{CI}$, $E_{th,IV}$ is $2E_{IV}$ and $E_{th,g} = 2E_g$ where $E_{th,CI}$, $E_{th,IV}$ and $E_{th,g}$ are the threshold energies of E_{CI}, E_{IV} and E_g respectively.

The bandgaps should be chosen such that $2E_{CI} < E_{IV} < 2E_{IV}$ and $2E_{IV} < E_g < 2E_g$ to generate two EHPs of each transition, requiring that E_g be greater than two times E_{IV}. However, E_g is the summation of E_{CI} and E_{IV} which forces E_g to be smaller than $2E_{IV}$ and thus the actual QY from VB to IB transitions is 1.

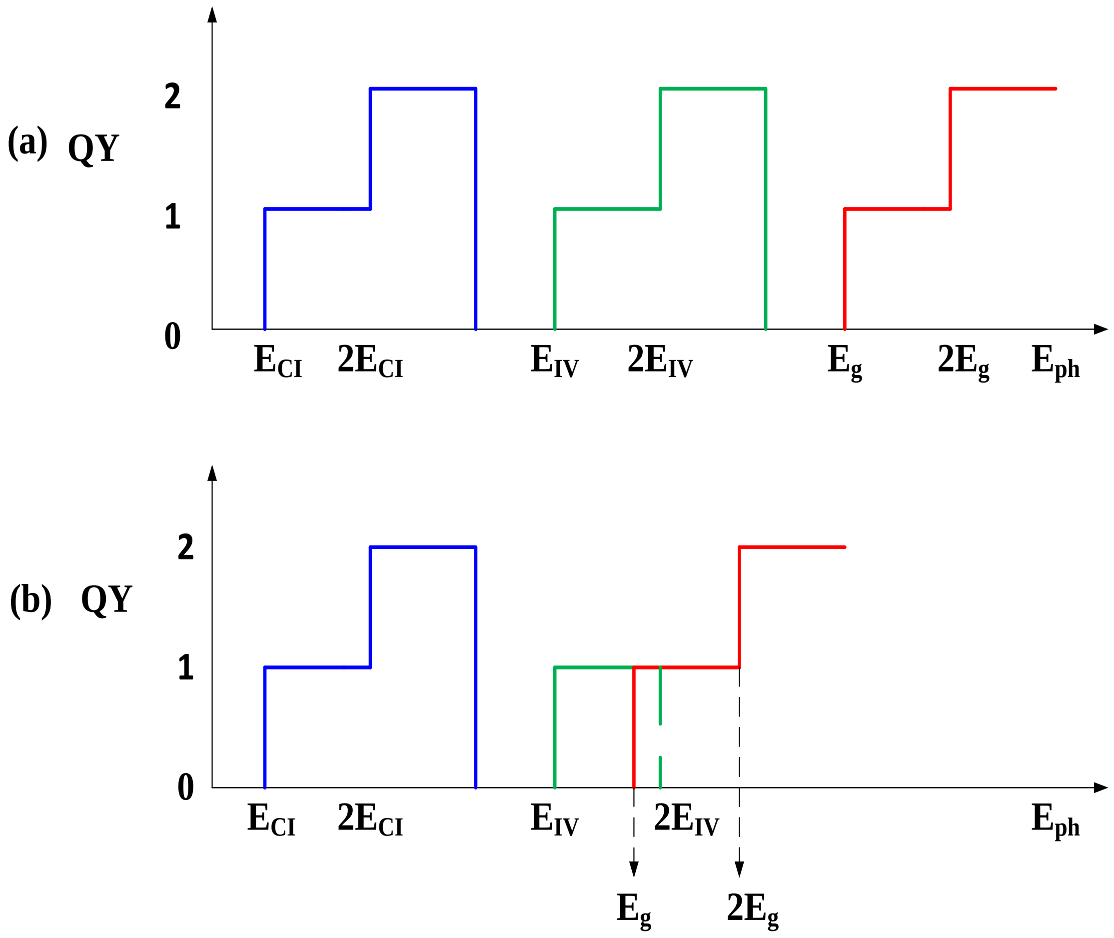

Fig.8.1. The QY of three transitions in the MIBSC, (a) Without restrictions for carrier multiplication, the order of bandgaps is $E_{CI}<2E_{CI}<E_{IV}<2E_{IV}<E_g(=E_{CV})<2E_g$. (b) The modified carrier generations of MIBSC. $E_{CI}<2E_{CI}<E_{IV}<E_g(=E_{CV})<2E_{IV}$.

Therefore, the conditions for bandgap alignment change to $2E_{CI}<E_{IV}<2E_{IV}$ and $E_{IV}<E_g<2E_{IV}$ to avoid spectral overlapping and achieve the maximum QY. The overall bandgap alignment is shown in equation (8.8) and in Fig.8.1 (b).

$$E_{CI}<2\cdot E_{CI}<E_{IV}<E_g(=E_{CV})<2\cdot E_{IV} \tag{8.8}$$

Under this condition, it is possible to generate more than two EHPS in MIBSC as is shown in Fig.8.2.

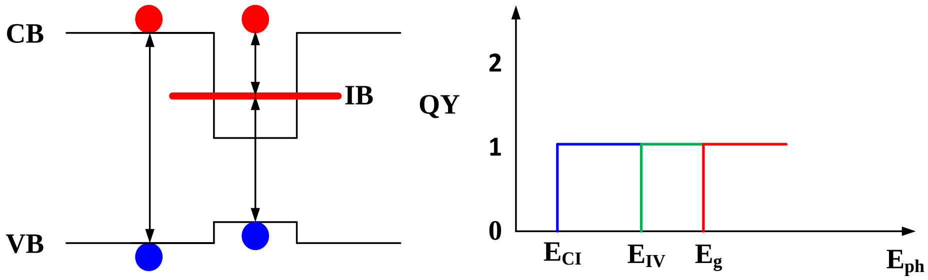

(a) Number of Electrons = 2

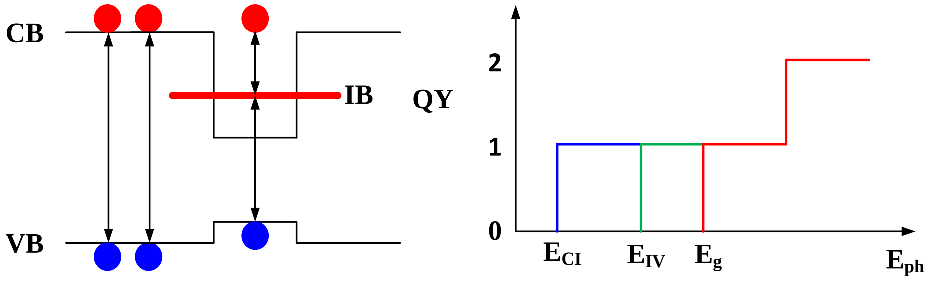

(b) Number of Electrons = 3

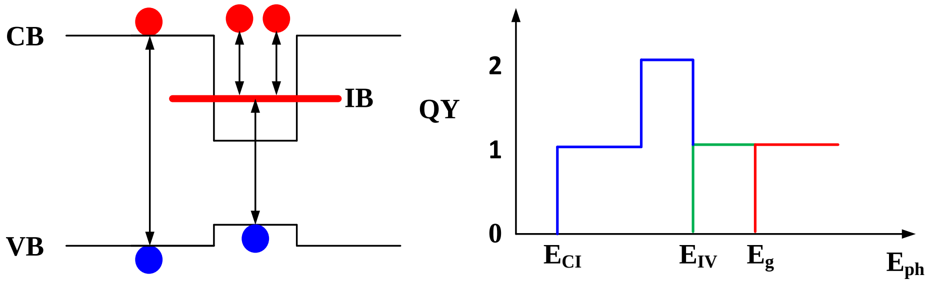

(c) Number of Electrons = 3

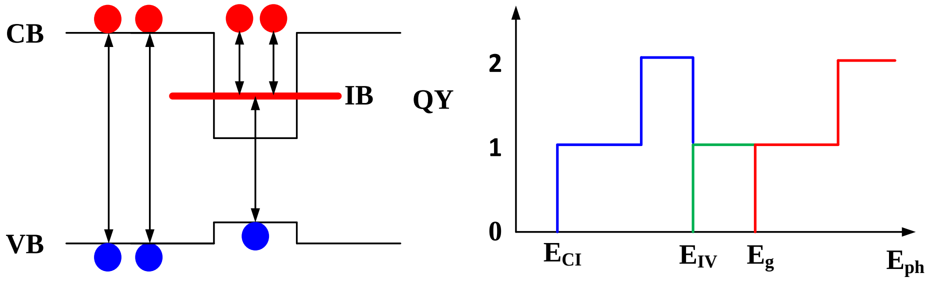

(d) Number of Electrons = 4

Fig. 8.2. The procedure of generation of carriers in the MIBSC, E_{ph} is the photon energy. (a) The number of electrons=2. (b) The number of electrons=3 which 2 is from VB to CB and 1 is IB to CB, (c) The number of electrons=3 which 1 is from VB to CB and 2 is IB to CB and (d) The number of electrons=4. The 4 EHPs are generated that 2 is from VB to CB and 2 is from IB to CB.

Further, regarding both QY and spectral splitting, the non-overlapping of QY from the three transitions is also important to optimize the characteristics of MIBSC. For instance, QY from E_{CI} can be 2 if the spectral splitting region from E_{CI} to E_{IV} is relatively large.

Thus, Fig. 8.2 provides conditions for MEG such that it generates two EHPs and increases current. However, if the difference between $E_{th,CI}$ and E_{IV} is small, the net effect of increasing current and QY can be negligible. In case of E_g, there can be two EHPs with no restrictions of spectrum splitting. But, the amount of solar photon energy at high energy is small so that the increase of light-generated current from E_g to infinity is not large. Therefore, choosing the proper range of the three bandgaps is important to maximize the carrier multiplication effect in the MIBSC.

8.2.3 The Possibility of Carrier Multiplication in MIBSC

In Fig.8.2, the author has presented the possible scenarios for the number of carriers generated in a MIBSC. In this section, the author will discuss which transition is dominant to generate more than two EHPs. First of all, in a QD region, two EHPs from IB to CB are shown in Fig. 8.1. Due to the charge neutrality condition, the carrier multiplication processes in Fig. 8.2 (c) and (d) are impossible without an additional assumption like another absorption path or doped IB. Even though the spectral splitting makes it possible to excite carriers from IB to CB to generate two EHPs, the number of EHPs from VB to IB is 1 which cannot provide another electron to excite from IB to CB by impact ionization.

Here, the author considers Fig 8.2 (a) and (b) in which the generated number of carriers are two from conventional IBSC theory (see Fig. 8.2 (a)) and three by impact ionization in a barrier region (see Fig. 8.2 (b)) and both spectral splitting and charge neutrality conditions can be satisfied.

8.3 Results

In this section, the author will discuss the simulation results and advantages of MIBSC. Fig.8.3 and Fig 8.4, Table 8.1 and 8.2 compares the theoretical maximum efficiency and optimum bandgaps for IBSC and MIBSC under blackbody radiation and terrestrial spectrum conditions.

Table 8.1. The comparison of both conversion efficiencies and optimum bandgaps between IBSC and MIBSC under blackbody radiation with one sun and full concentration where N is the number of electrons and η is the maximum conversion efficiency.

BB	N		E_{CI} (eV)	E_{IV} (eV)	E_g (eV)	η (%)
C=1	2	IBSC	0.92	1.48	2.4	46.8
	3	MIBSC	0.87	1.43	2.3	47.4
C=46200	2	IBSC	0.72	1.25	1.97	63.2
	3	MIBSC	0.47	0.93	1.40	66.7

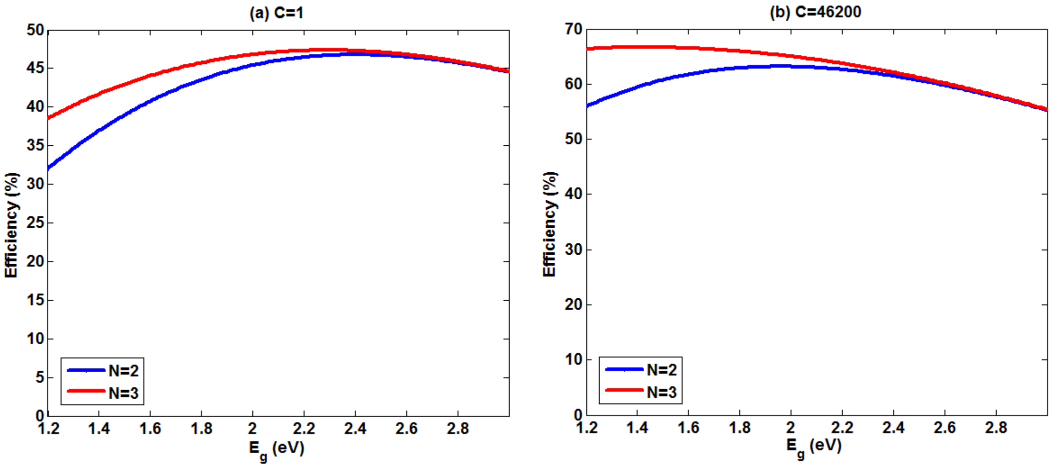

Fig. 8.3. The efficiencies vs optimum E_g where (a) is the one sun illumination (C=1) and (b) is the maximum concentration (C=46200) under blackbody radiation where N is the number of carriers at CB.

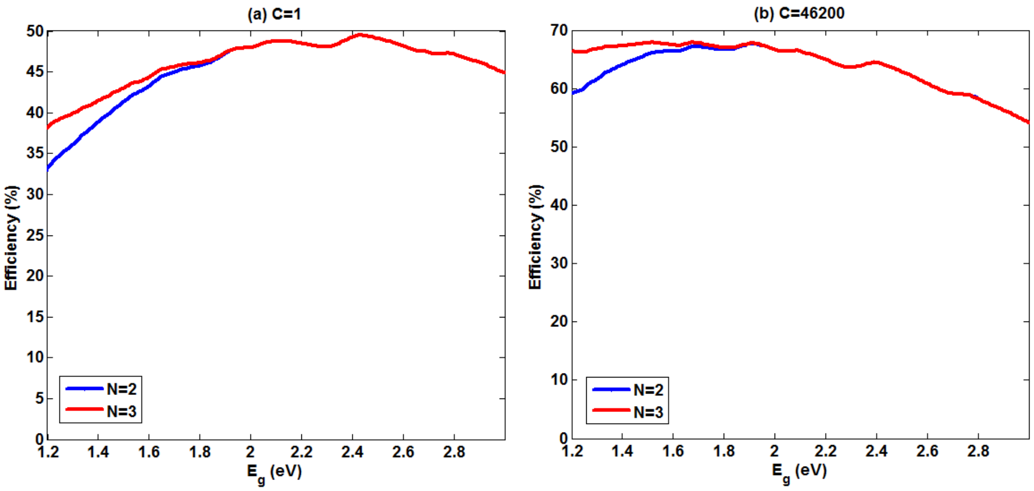

Fig. 8.4. The efficiencies vs optimum E_g where (a) is the one sun illumination (C=1) and (b) is the maximum concentration (C=46200) under terrestrial spectrum.

Table 8.2. The comparison of both conversion efficiencies and optimum bandgaps between IBSC and MIBSC under terrestrial spectrum with one sun and full concentration.

AM1.5	N		E_{CI} (eV)	E_{IV} (eV)	E_g (eV)	η (%)
C=1	2	IBSC	0.93	1.49	2.42	49.5
(AM1.5G)	3	MIBSC	0.93	1.49	2.42	49.5
C=46200	2	IBSC	0.69	1.22	1.91	67.7
(AM1.5D)	3	MIBSC	0.51	1.00	1.50	67.9

Under blackbody radiation with full concentration shown in Table 8.1 and Fig 8.3, the theoretical maximum efficiency is increased by 3.2% and the optimum bandgaps are 0.47 eV (=E_{CI}), 0.93 eV (=E_{IV}) and 1.40 eV (=E_g) for which the corresponding QY is 1, 1, and 2 respectively. Note that the bandgap of the barrier is similar to GaAs (=1.42 eV) and the QD material can be InAs (=0.36 eV).

Generally, the results clearly indicate that with blackbody radiation and under concentration conditions, due to carrier multiplications in the three optical transitions, one can choose low bandgap QD materials and a barrier material with a bandgap up to 2 eV.

For Eg above 2 eV the net effect of MEG in MIBSC disappears and the cell becomes similar to a conventional IBSC.

The bandgap trends for the terrestrial spectrum simulation results for MIBSC in Table 8.2 and Fig 8.4are similar to those found for blackbody radiation. However, a difference of only 0.2 % in the maximum conversion efficiency is found between MIBSC and IBSC under full concentration conditions because of fluctuations of the terrestrial spectrum. The general trends for the optimum three bandgaps are similar and the three optimum bandgaps are 0.51 eV(=E_{CI}), 1.00 eV(=E_{IV}) and 1.51 eV(=E_g) with corresponding QYs of 1, 1, and 2. The overall number of generated carriers is 3 at the maximum conversion efficiency point.

The optimum bandgaps under one sun with blackbody radiation or the terrestrial spectrum is slightly lowered compared to conventional IBSC due to the two carrier generations from E_g. The optimum bandgaps under the one sun terrestrial spectrum is the same as for a conventional IBSC due to the limited spectrum range. Thus, it is absolutely necessary to use the light concentrator to get the benefits.

From all above results, the author considers the possible material candidates of MIBSC where there are similar optimum bandgaps from both blackbody radiation and the terrestrial spectrum under concentration. Currently, there are reports of MEG or carrier multiplication phenomena in III-V materials such as InAs [43], InP [84], InN [85], InSb [148], and GaAs [149],[150]measured by terahertz pump-probe measurements. Among these materials, promising combinations such as InAs/InP, InAs/GaAs, InN/InGaN and InSb/AlInSb are potential candidates for MIBSC.

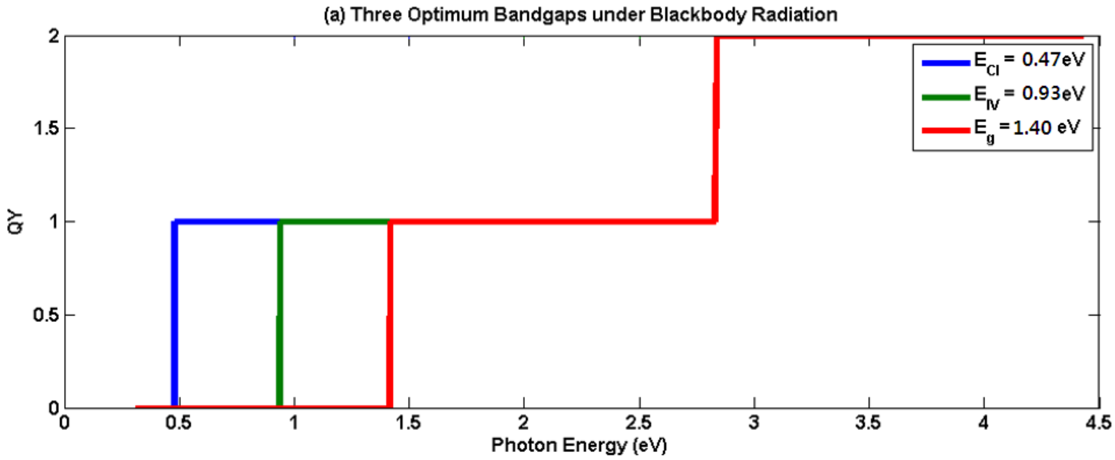
(a) Three Optimum Bandgaps under Blackbody Radiation

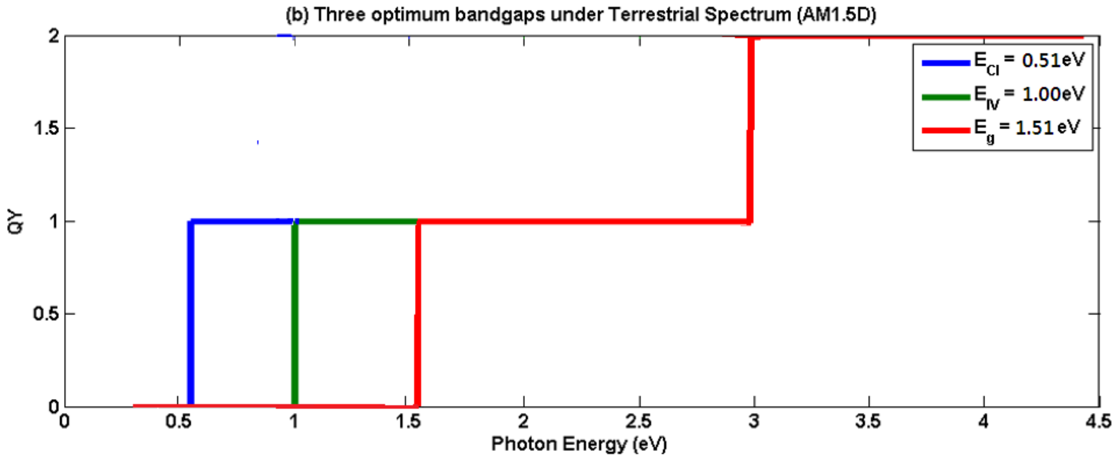
(b) Three optimum bandgaps under Terrestrial Spectrum (AM1.5D)

Fig. 8.5. The three bandgap alignments at the maximum conversion efficiency. (a) The total number of generated electrons is 3 under blackbody radiation. The optimum bandgaps under blackbody radiations are E_{CI}=0.47 eV, E_{IV}=0.93 eV and E_g=1.40 eV. (b) The total number of generated electrons is 3 under terrestrial spectrum. The optimum bandgaps under terrestrial spectrum are E_{CI}=0.51 eV, E_{IV}=1.00 eV and E_g=1.51 eV.

8.4 Conclusion

The author has developed a hybrid thermodynamic model of carrier multiplication integrated with IBSC. A careful consideration of the spectral splitting interactions with the QY shows the possible number of electrons at generated at the conduction band edge can be 2, 3 and 4 which is larger than in a conventional IBSC. But, the larger threshold energy from the valence band to intermediate band does not contribute to MEG (the effective QY of E_{IV} is 1) due to the overlap of QY between E_{CI} and E_{IV}. Other transitions such E_{CI} and E_g can make two EHPs. So, the overall efficiencies with and without concentration are only slightly enhanced. After accounting for solar spectral splitting and QY, the possible additional number of carriers generated is 3 due to transition from VB to CB because of charge neutrality condition and metallic properties of IB. Increasing the concentration of light is the only way to boost the MEG effect in the IBSC. Under these conditions, more incident photon energy into MIBSC has the possibility of increasing the number of carriers.

CHAPTER 9

CONCLUSION

The author has proposed several types of hybrid solar cell models by thermodynamics to overcome existing theoretical limit of PV cells and suggest suitable materials with nanostructures. The potential benefits of novel concept solar cells can have multi-physics effects in one solar cell due to integrating two concepts such as (1) multiple exciton generation (MEG) and tandem, (2) intermediate band (IB) and tandem and (3) MEG and IB while maintaining the properties of conventional solar cells. The development of hybrid concepts uniquely the realization of ultra-high solar cell efficiencies, as even including a single advanced concept approach, efficiencies substantially over 50% at realistic concentration ratios and with non-ideal assumption do not exist.

First, the author investigated the limiting efficiency of multiple exciton generation solar cell with non-ideal effect such as delayed threshold energy under concentration. The ideal quantum yield offers a large improvement of theoretical conversion efficiency to surpass the Shockley and Queisser limit. But, when examining non-ideal quantum yield and its threshold energy above the ideal values, the effect of carrier multiplications of single junction solar cell was reduced. In particular, the benefit disappears for one-sun conditions, so using concentrators is necessary to provide advantages in the theoretical conversion efficiency. Furthermore, the threshold energy should be located at between two and three times of bandgap materials to maximize the generating multiple electron and hole pairs.

Second, the thermodynamic limit of MEG with multijunction (MJMEG) has been proposed and calculated to upgrade the model of current tandem solar cells. General multjunction solar cells are presently leading the efficiency of PV cells. However, disadvantages like defects of interfacial layer cause the limit to monolithic growth and number of junctions. Thus, utilizing MEG with multijunction in nanostructures can contribute to enhance the characteristics of theoretical efficiency and use low bandgap materials. Its calculated efficiency is improved at the low number of junctions to maximize the carrier multilplication. However, the increased number of junction in this hybrid solar cell does not provide such large benefits due to decreasing the possible maximum quantum yield of each junction.

Third, after studying this MJMEG solar cell, the author focused on silicon nanostructure solar cells for MEG and MJMEG applications. Silicon has substantial possibility to use the nano-materials because even if silicon is an indirect bangap material, it can be direct bandgap materials in nanostructures due to excellent quantum confinement. The author has investigated the limiting efficiency of silicon MEG with concentration under terrestrial spectrum. Then, limiting efficiencies of Si MJMEG has also calculated. Silicon cover visible range of photon energy so that silicon nanostructures can use for the upper junction of MJMEG. Based on this, the author has investigated the appropriate materials for bottom junction such as InAs or InN. Furthermore, the compatibility of these material combinations also investigated to improve the quantum confinements.

Forth, the author presented the experiment results of a silicon nanostructured solar cell. The periodic silicon nanowire defined by electron beam lithography shows the improved short-circuit current. But, due to low open-circuit voltages and fill factors, related to the large rear junction area, the overall efficiency was low. Further, the optical resonance at the bandgap of amorphous silicon offer to beneficial effect of low reflectance. However, the number of nanostructures is also important to regard to reduce the reflectance the entire range of wavelength to increase the short-circuit current. With improvements in the rear surface structure, the proposed device offers an approach to realization of a silicon nanostructured solar cell.

Fifth, an alternative to overcoming tandem solar cells' limit is using an intermediate band solar cell. The most important assumption of intermediate band solar cell is three strong light-absorptions in one junction with intermediateband. Thus, it has three carrier transitions and its theoretical efficiency under full concentration is similar to triple junction tandem solar cells. The tandem configuration of double stacked intermediate band solar cells shows the similar theoretical efficiency of five or six junction tandem solar cells. Thus, this configuration reduces the number of junctions compared to tandem solar cells, enabling the efficiency of 5 or 6 junction device with only 4 materials. In material investigations, Si/Ge or III-V for the bottom junction with III-V nitride for the upper junction shows appropriate combinations for in an independent connection. For series-connection, near 0.9 eV material for the bottom junction and a high bandgap of 3eV materials (III-V or II-VI) for the top junction can be used. The materials for quantum dot are still require further materials to searches to optimize the properties and quantum confinement for efficient managing of photons.

The final discussion for novel concept of PV model is carrier multiplication at the intermediate band solar cells. The both concepts of solar cells can use the low bandgap materials to control the incoming photon efficiently. To investigate the possible regions of carrier multiplications, it is necessary to investigate the spectral splitting. The transition between (1) the intermediate band to conduction band and (2) the valence band to conduction band have the largest possibility of realizing carrier multiplication. However, the charge neutrality at the intermediate band must satisfy with valence the number of electron and hole pairs. A doped intermediate band can be considered to replace metallic properties of intermediate band.

Overall, the hybrid concepts of limiting efficiency model provide substantial potential to improve the efficiency of solar cells through developing multi-physical effects in one solar cell. Even if the proposed of third generation PV cells have large benefits to surpass the single junction limit, the suggested detailed balance limit of hybrid solar cells in this dissertation offer multiple advantages to overcoming the existing limits. Moreover, these hybrid model can be achieved by the existing solar cell materials such as silicon by using nanostructures such as quantum dots.

The detailed balance limit or thermodynamic limit can describe only the ideal PV model that it is not considered the real physical parameters of solar cells. Thus, it is also necessary to exploit the realistic hybrid solar cells model including multi-physics parameters and find ways to fabricate with appropriate material and structures.

REFERENCES

[1] "International Energy Outlook 2013," US Energy Information Administration, Department of Energy, published July 2013.

[2] "Annual Energy Review 2010 with projections to 2040," US Energy Information Administration, Department of Energy, published April 2013.

[3] "Renewable energy technologies: cost analysis series," vol.1, no. 4/5, International Renewable Energy Agency published in 2012.

[4] M. A. Green, "Third generation photovoltaics: Ultra-high conversion efficiency at low cost," Progress in Photovoltaics: Research and Applications, vol. 9, no. 2, pp. 123-135, 2001.

[5] "Best Research Cell Efficiency," National Renewable Energy Laboratory, published 2013, (http://www.nrel.gov/ncpv/images/efficiency_chart.jpg)

[6] M. A. Green, K. Emery, Y. Hishikawa, W. Warta, and E. D. Dunlop, "Solar cell efficiency tables (version 42)," Progress in Photovoltaics: Research and Applications, vol. 21, no. 5, pp. 827-837, 2013.

[7] PVCDROM, "http://pveducation.org/pvcdrom"

[8] J. Zhao, A. Wang, and M. A. Green, "24·5% Efficiency silicon PERT cells on MCZ substrates and 24·7% efficiency PERL cells on FZ substrates," Progress in Photovoltaics: Research and Applications, vol. 7, no. 6, pp. 471-474, 1999.

[9] B. M. Kayes, N. Hui, R. Twist, S. G. Spruytte, F. Reinhardt, I. C. Kizilyalli, and G. S. Higashi, "27.6% Conversion efficiency, a new record for single-junction solar cells under 1 sun illumination." In Proc. Of 37th IEEE Phovovoltaic Special Conference, pp. 000004-000008., Seattle, WA, 2011.

[10] http://panasonic.co.jp/corp/news/official.data/data.dir/2014/04/en140410-4/en140410-4.html

[11] S.P. Philipps, E. Essig, S. Heckelmann, R. Kellenbenz, V. Klinger, M. Niemeyer, D. Lackner, F. Dimroth, "Overview about Technology Perspectives for High Efficiency Solar Cells for Space and Terrestrial Applications," Presented in 28th European Photovoltaic Solar Energy Conference and Exhibition 2013 Paris,France, http://www.ise.fraunhofer.de/de/veroeffentlichungen/konferenzbeitraege/konferenzbeitraege-2013/28th-eupvsec/bett.pdf

[12] W. Shockley and H.J. Queisser. "Detailed balance limit of efficiency of p-n junction solar cells", Journal of Applied Physics, vol. 32, no.3, pp. 510-519, 1961.

[13] S. Kolodinski, J. H. Werner, T. Wittchen, and H. J. Queisser, "Quantum efficiencies exceeding unity due to impact ionization in silicon solar cells," Applied Physics Letters, vol. 63, no. 17, pp. 2405-2407, 1993.

[14] J. H. Werner, S. Kolodinski, and H. J. Queisser, "Novel optimization principles and efficiency limits for semiconductor solar cells," Physical Review Letters, vol. 72, no. 24, pp. 3851-3854, 1994.

[15] A. Luque, and A. Martí, "Increasing the efficiency of ideal solar cells by photon induced transitions at intermediate levels," Physical Review Letters, vol. 78, no. 26, pp. 5014-5017, 1997.

[16] S. A. Blokhin, A. V. Sakharov, A. M. Nadtochy, A. S. Pauysov, M. V. Maximov, N. N. Ledentsov, A. R. Kovsh, S. S. Mikhrin, V. M. Lantratov, S. A. Mintairov, N. A. Kaluzhniy, and M. Z. Shvarts, "AlGaAs/GaAs photovoltaic cells with an array of InGaAs QDs," Semiconductors, vol. 43, no. 4, pp. 514-518, 2009.

[17] P. Atkins, "The Laws of Thermodynamics: A very short introduction," Oxford University Press, April, 2010

[18] A. De Vos, "Endoreversible Thermodynamics of Solar Energy Conversion", Oxford University Press, 1992.

[19] M. C. Beard, and R. J. Ellingson, "Multiple exciton generation in semiconductor nanocrystals: Toward efficient solar energy conversion," Laser & Photonics Reviews, vol. 2, no. 5, pp. 377-399, 2008.

[20] S. P. Bremner, M. Y. Levy, and C. B. Honsberg, "Analysis of tandem solar cell efficiencies under AM1.5G spectrum using a rapid flux calculation method," Progress in Photovoltaics: Research and Applications, vol. 16, no. 3, pp. 225-233, 2008.

[21] A. D. Vos, "Detailed balance limit of the efficiency of tandem solar cells," Journal of Physics D: Applied Physics, vol. 13, no. 5, pp. 839-846, 1980.

[22] M. Wiemer, V. Sabnis, and H. Yuen, "43.5% efficient lattice matched solar cells," In Proc. Of SPIE High and low concentrator systems for electric applications VI, San Diego, CA, pp. 810804-810804, 2011.

[23] "World Record Solar Cell with 44.7% Efficiency," press released September, 2013 http://www.ise.fraunhofer.de/en/press-and-media/press-releases/presseinformationen-2013/world-record-solar-cell-with-44.7-efficiency.

[24] J. Lee and and C. B. Honsberg, "Impact of threshold energy of multiple exciton generation solar cells." in Proc. 39th IEEE Photovoltaic Spec. Conf., Tampa, FL, 2013, pp. 1050-1053.

[25] R. Brendel, J. H. Werner, and H. J. Queisser, "Thermodynamic efficiency limits for semiconductor solar cells with carrier multiplication," Solar Energy Materials and Solar Cells, vol. 41–42, no. 0, pp. 419-425, 1996.

[26] A. De Vos, and B. Desoete, "On the ideal performance of solar cells with larger-than-unity quantum efficiency," Solar Energy Materials and Solar Cells, vol. 51, no. 3–4, pp. 413-424, 1998.

[27] J. H. Werner, R. Brendel, and H. J. Queisser, "Radiative efficiency limit of terrestrial solar cells with internal carrier multiplication," Applied Physics Letters, vol. 67, no. 7, pp. 1028-1030, 1995.

[28] J.H. Werner, R. Brendel, H.J. Queisser, "New upper efficiency limits for semiconductor solar cells," in: Proceedings of the IEEE 1st World Conference on Photovoltaic Energy Conversion, Waikoloa, HI, USA, 1994, pp. 1742–1745.

[29] R. J. Ellingson, M. C. Beard, J. C. Johnson, P. Yu, O. I. Micic, A. J. Nozik, A. Shabaev, and A. L. Efros, "Highly efficient multiple exciton generation in colloidal PbSe and PbS Quantum Dots," Nano Letters, vol. 5, no. 5, pp. 865-871, 2005.

[30] A. Luque, and A. Martí, "A metallic intermediate band high efficiency solar cell," Progress in Photovoltaics: Research and Applications, vol. 9, no. 2, pp. 73-86, 2001.

[31] M. A. Green, "Third generation photovoltaics: solar cells for 2020 and beyond," Physica E: Low-dimensional Systems and Nanostructures, vol. 14, no. 1–2, pp. 65-70, 2002.

[32] A. J. Nozik, "Quantum dot solar cells," Physica E: Low-dimensional Systems and Nanostructures, vol. 14, no. 1–2, pp. 115-120, 2002.

[33] J. A. Burton, "Electron emission from avalanche breakdown in silicon," Physical Review, vol. 108, no. 5, pp. 1342-1343, 1957.

[34] V. S. Vavilov, "On photo-ionization by fast electrons in germanium and silicon," Journal of Physics and Chemistry of Solids, vol. 8, no. 0, pp. 223-226, 1959.

[35] O. Christensen, "Quantum efficiency of the internal photoelectric effect in silicon and germanium," Journal of Applied Physics, vol. 47, no. 2, pp. 689-695, 1976.

[36] F. Capasso, P. M. Petroff, W. B. Bonner, and S. Sumski, “Investigation of microplasmas in InP avalanche photodiodes,” Electron Device Letters, IEEE, vol. 1, no. 3, pp. 27-29, 1980.

[37] M. C. Beard, A. G. Midgett, M. C. Hanna, J. M. Luther, B. K. Hughes, and A. J. Nozik, “Comparing multiple exciton generation in quantum dots to impact ionization in bulk semiconductors: Implications for enhancement of solar energy conversion,” Nano Letters, vol. 10, no. 8, pp. 3019-3027, 2010.

[38] R. D. Schaller, M. Sykora, J. M. Pietryga, and V. I. Klimov, “Seven Excitons at a Cost of One: Redefining the limits for conversion efficiency of photons into charge carriers,” Nano Letters, vol. 6, no. 3, pp. 424-429, 2006.

[39] S. J. Kim, W. J. Kim, Y. Sahoo, A. N. Cartwright, and P. N. Prasad, “Multiple exciton generation and electrical extraction from a PbSe quantum dot photoconductor,” Applied Physics Letters, vol. 92, no. 3, pp. 031107 – 031107-3, 2008.

[40] G. Nair, and M. G. Bawendi, “Carrier multiplication yields of CdSe and CdTe nanocrystals by transient photoluminescence spectroscopy,” Physical Review B, vol. 76, no. 8, pp. 081304-1 081304-4, 2007.

[41] R. D. Schaller, M. A. Petruska, and V. I. Klimov, “Effect of electronic structure on carrier multiplication efficiency: Comparative study of PbSe and CdSe nanocrystals,” Applied Physics Letters, vol. 87, no. 25, pp. 253102-1-253102-3, 2005.

[42] J. J. H. Pijpers, E. Hendry, M. T. W. Milder, R. Fanciulli, J. Savolainen, J. L. Herek, D. Vanmaekelbergh, S. Ruhman, D. Mocatta, D. Oron, A. Aharoni, U. Banin, and M. Bonn, “Carrier multiplication and its reduction by photodoping in colloidal InAs quantum dots,” The Journal of Physical Chemistry C, vol. 111, no. 11, pp. 4146-4152, 2007.

[43] R. D. Schaller, J. M. Pietryga, and V. I. Klimov, “Carrier multiplication in InAs nanocrystal quantum dots with an onset defined by the energy conservation limit,” Nano Letters, vol. 7, no. 11, pp. 3469-3476, 2007.

[44] M. C. Beard, K. P. Knutsen, P. Yu, J. M. Luther, Q. Song, W. K. Metzger, R. J. Ellingson, and A. J. Nozik, “Multiple exciton generation in colloidal silicon nanocrystals,” Nano Letters, vol. 7, no. 8, pp. 2506-2512, 2007.

[45] J. A. McGuire, J. Joo, J. M. Pietryga, R. D. Schaller, and V. I. Klimov, “New aspects of carrier multiplication in semiconductor nanocrystals,” Accounts of Chemical Research, vol. 41, no. 12, pp. 1810-1819, 2008.

[46] M. T. Trinh, A. J. Houtepen, J. M. Schins, T. Hanrath, J. Piris, W. Knulst, A. P. L. M. Goossens, and L. D. A. Siebbeles, “In spite of recent doubts carrier multiplication does occur in PbSe nanocrystals,” Nano Letters, vol. 8, no. 6, pp. 1713-1718, 2008.

[47] M. C. Beard, A. G. Midgett, M. Law, O. E. Semonin, R. J. Ellingson, and A. J. Nozik, “Variations in the quantum efficiency of multiple exciton generation for a series of chemically treated PbSe nanocrystal Films,” Nano Letters, vol. 9, no. 2, pp. 836-845, 2009.

[48] J. J. H. Pijpers, R. Ulbricht, K. J. Tielrooij, A. Osherov, Y. Golan, C. Delerue, G. Allan, and M. Bonn, “Assessment of carrier-multiplication efficiency in bulk PbSe and PbS,” Nature Physics, vol. 5, no. 11, pp. 811-814, 2009.

[49] P. Tyagi, and P. Kambhampati, “False multiple exciton recombination and multiple exciton generation signals in semiconductor quantum dots arise from surface charge trapping,” The Journal of Chemical Physics, vol. 134, no. 9, pp. 094706-1-094706-10, 2011.

[50] A. G. Midgett, H. W. Hillhouse, B. K. Hughes, A. J. Nozik, and M. C. Beard, “Flowing versus Static conditions for measuring multiple exciton generation in PbSe quantum dots,” The Journal of Physical Chemistry C, vol. 114, no. 41, pp. 17486-17500, 2010.

[51] M. T. Trinh, L. Polak, J. M. Schins, A. J. Houtepen, R. Vaxenburg, G. I. Maikov, G. Grinbom, A. G. Midgett, J. M. Luther, M. C. Beard, A. J. Nozik, M. Bonn, E. Lifshitz, and L. D. A. Siebbeles, “Anomalous independence of multiple exciton generation on different group IV−VI quantum dot architectures,” Nano Letters, vol. 11, no. 4, pp. 1623-1629, 2011.

[52] O. E. Semonin, J. M. Luther, S. Choi, H.-Y. Chen, J. Gao, A. J. Nozik, and M. C. Beard, “Peak external photocurrent quantum efficiency exceeding 100% via MEG in a quantum dot solar cell,” Science, vol. 334, no. 6062, pp. 1530-1533, 2011.

[53] P. D. Cunningham, J. E. Boercker, E. E. Foos, M. P. Lumb, A. R. Smith, J. G. Tischler, and J. S. Melinger, “Enhanced multiple exciton generation in quasi-one-dimensional semiconductors,” Nano Letters, vol. 11, no. 8, pp. 3476-3481, 2011.

[54] M. C. Hanna, and A. J. Nozik, “Solar conversion efficiency of photovoltaic and photoelectrolysis cells with carrier multiplication absorbers,” Journal of Applied Physics, vol. 100, no. 7, pp. 074510-1-074510-8, 2006.

[55] Y. Takeda, and T. Motohiro, “Requisites to realize high conversion efficiency of solar cells utilizing carrier multiplication,” Solar Energy Materials and Solar Cells, vol. 94, no. 8, pp. 1399-1405, 2010.

[56] M. C. Hanna, M. C. Beard, and A. J. Nozik, “Effect of solar concentration on the thermodynamic power conversion efficiency of quantum-dot solar cells exhibiting multiple exciton generation,” The Journal of Physical Chemistry Letters, vol. 3, no. 19, pp. 2857-2862, 2012.

[57] American Society for Testing and Materials- "Standard tables for reference solar spectral irradiances: Direct normal and hemispherical on 37° Tilted Surface,"

[58] A. De Vos, “Detailed balance limit of the efficiency of tandem solar cells”, Journal of Physics. D: Applied Physics, vol. 13, pp. 839-846, 1980.

[59] M. S. Leite, R. L. Woo, J. N. Munday, W. D. Hong, S. Mesropian, D. C. Law, and H. A. Atwater, “Towards an optimized all lattice-matched InAlAs/InGaAsP/InGaAs multijunction solar cell with efficiency > 50%,” Applied Physics Letters, vol. 102, no. 3, pp. 033901-5-1-033901-5, 2013.

[60] J. Lee and C. B. Honsberg, “Limiting efficiencies over 50% using multijunction solar cells with multiple exciton generation”, in Proc. 38th IEEE Photovoltaic Spec. Conf., Austin, TX, 2012, pp 62-67.

[61] J. Lee, and C. B. Honsberg, “Limiting Efficiencies of Multijunction Solar Cells With Multiple Exciton Generation,” Photovoltaics, IEEE Journal of, vol. 4, no. 3, pp. 874-880, 2014.

[62] E. D. Jackson, “Areas for improvement of the semiconductor solar energy converter”, Trans. Conf. on Use of Solar Energy, Tucson, AZ, Oct.31-Nov.1, 1955, pp 122-126.

[63] R. L. Moon, L. W. James, H. A. VanderPlas, T. O. Yep, G. A. Antypas, and Y. Chai, “ Multigap solar cell requirements and the performance of AlGaAs and Si cells in concentrated sunlight”, in Proc. 13th IEEE Photovoltaic Spec. Conf., 1978, pp 859-867.

[64] D. Friedman, S. Kurtz, K. Bertness, A. Kibbler, C.Kramer, J. Olson, D. King, B. Hansen, and J. Snyder, “GaInP/GaAs monolithic tandem concentrator cells”, in. Proc. 24th IEEE Photovoltaic Spec. Conf. Waikoloa, HI, 1994, pp. 1829–1832.

[65] S. R. Kurtz, D. Myers, and J. M. Olson, “Projected performance of three- and four-junction devices using GaAs and GaInP”, in. Proc. 26th IEEE Photovoltaic Spec. Conf., Anaheim, CA, 1997, pp. 875-878.

[66] R. R. King, D. C. Law, K. M. Edmondson, C. M. Fetzer, G. S. Kinsey, H. Yoon, R. A. Sherif, and N. H. Karam, “40% efficient metamorphihc GaInP/GaInAs/Ge multijunction solar cells”, Applied Physics Letters, vol. 90, no. 18, pp. 183516-1-183516-3, 2007.

[67] R. R. King, R. A. Sherif, D. C. Law, J. T. Yen, M. Haddad, C. M. Fetzer,K. M. Edmondson, G. S. Kinsey, H. Yoon, M. Joshi, S. Mesropian, H. L. Cotal, D. D. Krut, J. H. Ermer, and N. H. Karam, "New horizons in III-V multijunction terrestrial concentrator cell research", in Proc. the 21st Eur. Photovoltaic Solar Energy Conf., Dresden, Germany, pp. 124-128.

[68] R. R. King, D. C. Law, C. M. Fetzer, R. A. Sherif, K. M. Edmondson, S. Kurtz, G. S. Kinsey, H. L. Cotal, D. D. Krut, J. H. Ermer, and N. H. Karam, "Pathways to 40% efficient concentrator photovoltaics", in Proc. 20th Eur. Photovoltaic Solar Energy Conf., Barcelona, Spain, 2005, pp. 118-123.

[69] J. F. Geisz, S. R. Kurtz, M. W. Wanlass, J. S. Ward, A. Duda, D. J. Friedman, J. M. Olson, W. E. McMahon, T. Moriarty, and J. Kiehl, "High-efficiency GaInP/GaAs/InGaAs triple-junction solar cells grown inverted with a metamorphic bottom junction", Applied Physics Letters., vol. 91.no. 2, pp. 023502-1-023502-1, 2007.

[70] J.F. Geisz, D. J. Friedman, J.S. Ward, A. Duda, W. J. Olavarroa, T. E. Moriatry, J.T. Kiehl, M.J. Romero, A.G. Norman and K. M. Jones, "40.8% efficient inverted triple-junction solar cell with two independently metamorphic junctions", Applied Physics Letters, vol. 93., pp. 123505-1- 123505-3, 2008.

[71] R. R. King, A. Boca, W. Hong, X.-Q. Liu, D. Bhusari, D. Larrabee, K. M. Edmondson, D. C. Law, C. M. Fetzer, S. Mesropian, and N. H. Karam, "Band-gap-engineered architectures for high-efficiency multijunction concentrator solar cells", in Proc. 24th Eur. Photovoltaic Solar Energy Conf., 2009, pp. 55-61.

[72] S. Wojtczuk, P. Chiu, X. Zhang, D. Derkacs, C. Harris, D. Pulver, and M. Timmons, "InGaP/GaAs/InGaAs concentrators using Bi-facial epigrowth", in Proc. 35th IEEE Photovoltaic Spec. Conf., Honolulu, HI, 2010, pp. 1259-1264.

[73] M. Yamaguchi, "III-V compound multi-junction solar cells: Present and future", Solar Energy Materials and Solar Cells., vol. 75, no. 1–2,pp. 261-269, 2003

[74] M. Courel, J. C. Rimada, and L. Hernández, "GaAs/GaInNAs quantum well and superlattice solar cell", Applied Physics Letters., vol. 100, no. 7, pp. 073508-1-073508-4, 2012.

[75] A. Martí, and G. L. Araújo, "Limiting efficiencies for photovoltaic energy conversion in multigap systems," Solar Energy Materials and Solar Cells, vol. 43, no. 2, pp. 203-222, 1996.

[76] A. S. Brown, and M. A. Green, “Detailed balance limit for the series constrained two terminal tandem solar cell,” Physica E: Low-dimensional Systems and Nanostructures, vol. 14, no. 1–2, pp. 96-100, 2002

[77] H. Cotal, C. Fetzer, J. Boisvert, G. Kinsey, R. King, P. Hebert, H. Yoon, and N. Karam, “III-V multijunction solar cells for concentrating photovoltaics,” Energy & Environmental Science, vol. 2, no. 2, pp. 174-192, 2009.

[78] B. Beaumont, P. Garabedian, G. Nataf, J. C. Guillaume, P. Gilbart, and C. Verie, "Mechanically stacked two-tandem concentrator solar cell concept.", in Proc. 21st IEEE Photovoltaic Spec. Conf., 1990, pp. 47-52.

[79] P. T. Landsberg and V. Badescu, “Solar cell thermodynamics including multiple impact ionization and concentration of radiation”, Journal of Physics D.: Applied Physics., vol. 35, pp. 1236-1240, 2002.

[80] P. Würfel, “Solar energy conversion with hot electrons from impact ionisation,” Solar Energy Materials and Solar Cells, vol. 46, no. 1, pp. 43-52, 1997.

[81] R. D. Schaller, and V. I. Klimov, “High efficiency carrier multiplication in PbSe nanocrystals: Implications for Solar Energy Conversion,” Physical Review Letters, vol. 92, no. 18, pp. 186601-1-186601-4, 2004.

[82] A.J. Nozik, “Multiiple exciton generation in semiconductor quantum dots”, Chemical Physics Letters, vol. 457, pp. 3-11, 2008.

[83] S. K. Stubbs, S. J. O. Hardman, D. M. Graham, B. F. Spencer, W. R. Flavell, P. Glarvey, O. Masala, N. L. Pickett, and D. J. Binks, “Efficient carrier multiplication in InP nanoparticles,” Physical Review B, vol. 81, no. 8, pp. 081303-1-081303-4, 2010.

[84] S. A. Jensen, J. Versluis, E. Canovas, J. J. H. Pijpers, I. R. Sellers, and M. Bonn, “Carrier multiplication in bulk indium nitride,” Applied Physics Letters, vol. 101, no. 22, pp. 222113-1-222113-4, 2012.

[85] F. Dimroth, “High-efficiency solar cells from III-V compound semiconductors,” physica status solidi (c), vol. 3, no. 3, pp. 373-379, 2006.

[86] J. Lee, S. M. Goodnick, and C. B. Honsberg, "Limiting efficiency of silicon based nanostructure solar cells for multiple exciton generation." In Proc. Of 39th IEEE Phovovoltaic Special Conference, pp. 1046-1049, Tampa, MI, 2013.

[87] C. Delerue, G. Allan, and M. Lannoo, “Theoretical aspects of the luminescence of porous silicon,” Physical Review B, vol. 48, no. 15, pp. 11024-11036, 1993.

[88] W. A. Su, and W. Z. Shen, “A statistical exploration of multiple exciton generation in silicon quantum dots and optoelectronic application,” Applied Physics Letters, vol. 100, no. 7, pp. 071111-1-071111-5, 2012.

[89] C. Meier, A. Gondorf, S. Lüttjohann, A. Lorke, and H. Wiggers, “Silicon nanoparticles: Absorption, emission, and the nature of the electronic bandgap,” Journal of Applied Physics, vol. 101, no. 10, pp. 103112-1-103112-7, 2007.

[90] S. Baskoutas, and A. F. Terzis, “Size-dependent band gap of colloidal quantum dots,” Journal of Applied Physics, vol. 99, no. 1, pp. 013708-1-013708-4, 2006.

[91] D. Timmerman, J. ValentaJ, K. Dohnalova, W.D.A.M. de Boer, and T. Gregorkiewicz, “Step-like enhancement of luminescence quantum yield of silicon nanocrystals,” Nature Nanotechnology, vol. 6, no. 11, pp. 710-713, 2011.

[92] W. Wei, X.-Y. Bao, C. Soci, Y. Ding, Z.-L. Wang, and D. Wang, “Direct Heteroepitaxy of Vertical InAs Nanowires on Si Substrates for Broad Band Photovoltaics and Photodetection,” Nano Letters, vol. 9, no. 8, pp. 2926-2934, 2009.

[93] K. Tomioka, J. Motohisa, S. Hara, and T. Fukui, “Control of InAs Nanowire Growth Directions on Si,” Nano Letters, vol. 8, no. 10, pp. 3475-3480, 2008.

[94] B. Ehrler, K. P. Musselman, M. L. Bohm, R. H. Friend, and N. C. Greenham, “Hybrid pentacene/a-silicon solar cells utilizing multiple carrier generation via singlet exciton fission,” Applied Physics Letters, vol. 101, no. 15, pp. 153507-1-153507-3, 2012.

[95] H. Shujuan, and C. Gavin, “Sputter-grown Si quantum dot nanostructures for tandem solar cells,” Journal of Physics D: Applied Physics, vol. 46, no. 2, pp. 024003-1-024003-8, 2013.

[96] M. A. Green, “Recent developments in photovoltaics,” Solar Energy, vol. 76, no. 1–3, pp. 3-8, 2004.

[97] E. Garnett, and P. Yang, “Light trapping in silicon nanowire solar cells,” Nano Letters, vol. 10, no. 3, pp. 1082-1087, 2010.

[98] E. A. Alsema, “Energy pay-back time and CO2 emissions of PV systems,” Progress in Photovoltaics: Research and Applications, vol. 8, no. 1, pp. 17-25, 2000.

[99] B. Dale B, H. G. Rudenberg “High efficiency silicon solar cells,” In: Proceedings of the 14th Annual Power Sources Conference. Proceedings of the 14th Annual Power Sources Conference. U.S. Army Signal Research and Development Lab; 1960. p. 22.

[100] M. Taguchi, A. Yano, S. Tohoda, K. Matsuyama, and Y. Nakamura, paper, presented at the Thirty-ninth IEEE Photovoltaic Specialists Conference, 2013

[101] S. Y. Herasimenka, W. J. Dauksher, and S. G. Bowden, “>750 mV open circuit voltage measured on 50 μm thick silicon heterojunction solar cell,” Applied Physics Letters, vol. 103, no. 5, pp. 053511-1-053511-4, 2013.

[102] C. Green, “Silicon Nanowires for Optical Light Trapping in Solar Cells” , on 2013 Research Accomplishments, National Nanotechnology Intrastructure Network Research Experience for Undergraduates Program, pp. 178-179, 2013 “http://nnin.org/sites/default/files/2013_reu_ra/2013nninRA_1Book_0.pdf”

[103] G. Conibeer, M. Green, R. Corkish, Y. Cho, E.-C. Cho, C.-W. Jiang, T. Fangsuwannarak, E. Pink, Y. Huang, T. Puzzer, T. Trupke, B. Richards, A. Shalav, and K.-l. Lin, “Silicon nanostructures for third generation photovoltaic solar cells,” Thin Solid Films, vol. 511–512, no. 0, pp. 654-662, 2006.

[104] S. Mokkapati, and K. R. Catchpole, “Nanophotonic light trapping in solar cells,” Journal of Applied Physics, vol. 112, no. 10, pp. 101101-1- 101101-19, 2012.

[105] F. Priolo, T. Gregorkiewicz, M. Galli, and T. F. Krauss, “Silicon nanostructures for photonics and photovoltaics,” Nature Nanotechnology, vol. 9, no. 1, pp. 19-32, 2014.

[106] M. Yamaguchi, T. Takamoto, K. Araki, M. Imaizumi, N. Kojima, and Y. Ohshita, "Present and future of high efficiency multi-junction solar cells," Lasers and Electro-Optics, OSA Technical Digest (CD). p. CMT5. pp.1-3, 2011.

[107] M. Yamaguchi, T. Takamoto, K. Araki, and N. Ekins-Daukes, “Multi-junction III–V solar cells: current status and future potential,” Solar Energy, vol. 79, no. 1, pp. 78-85, 2005.

[108] K.-Y. Ban, S. P. Bremner, G. Liu, S. N. Dahal, P. C. Dippo, A. G. Norman, and C. B. Honsberg, “Use of a GaAsSb buffer layer for the formation of small, uniform, and dense InAs quantum dots,” Applied Physics Letters, vol. 96, no. 18, pp. 183101-1-183101-3, 2010.

[109] S. N. Dahal, S. P. Bremner, and C. B. Honsberg, “Identification of candidate material systems for quantum dot solar cells including the effect of strain,” Progress in Photovoltaics: Research and Applications, vol. 18, no. 4, pp. 233-239, 2010.

[110] E. Antolín E, A. Marti, and A. Luque, “Energy conversion efficiency limit of series connected intermediate band solar cells”. In Proc. of the 21st European Photovoltaic Solar Energy Conference, Barcelona, Spain, pp. 412-415, 2006.

[111] E. Antolín, A. Martí, P.G. Linares, I. Ramiro, E. Hernández, and A. Luque, “Raising the efficiency limit of the GaAs – Based intermediate band solar cells through the implementation of a monolithic tandem with an AlGaAs top cell,” In Proc. of 5th World Conference on Photovoltaic Energy Conversion, Valencia, Spain, pp. 65-68, 2010.

[112] A. Luque, “Will we exceed 50% efficiency in photovoltaics?,” Journal of Applied Physics, vol. 110, no. 3, pp. 031301-1- 031301-19, 2011.

[113] J. Lee J and C.B. Honsberg. “The thermodynamic limits of tandem photovoltaic devices with intermediate band,” In Proceedings of the SPIE Physics, Simulation, and Photonic Engineering of Photovoltaic Devices, San Francisco, USA, volume 8256, pages 82560Q-1-82560Q-12, 2012.

[114] A. Luque, P. G. Linares, A. Mellor, V. Andreev, and A. Marti, “Some advantages of intermediate band solar cells based on type II quantum dots,” Applied Physics Letters, vol. 103, no. 12, pp. 123901-1-123901-4, 2013.

[115] K. Brunner, “Si/Ge nanostructures,” Reports on Progress in Physics, vol. 65, no. 1, pp. 27-27- 72, 2002.

[116] S. Kaiser, T. Mensing, L. Worschech, F. Klopf, J. P. Reithmaier, and A. Forchel, “Optical spectroscopy of single InAs/InGaAs quantum dots in a quantum well,” Applied Physics Letters, vol. 81, no. 26, pp. 4898-4900, 2002.

[117] Y. Mitsuaki, S. Yoshitaka, O. Hiroyuki, K. Kazuto, S. Shigehiko, I. Masataka, “Characteristics of self-assembled InSb dots grown on (100) AlGaSb by molecular beam epitaxy,” Japanese Journal of Applied Physics, vol. 37, pp. 2455-2459, 1998.

[118] P. Klenovský, V. Křápek, D. Munzar, and J. Humlíček, “Electronic structure of InAs quantum dots with GaAsSb strain reducing layer: Localization of holes and its effect on the optical properties,” Applied Physics Letters, vol. 97, no. 20, pp. 203107-1-203107-3, 2010.

[119] A. Martí, C. Tablero, E. Antolín, A. Luque, R. P. Campion, S. V. Novikov, and C. T. Foxon, “Potential of Mn doped $In_{1-x}Ga_{x}N$ for implementing intermediate band solar cells,” Solar Energy Materials and Solar Cells, vol. 93, no. 5, pp. 641-644, 2009.

[120] P. G. Moses, and C. G. Van de Walle, “Band bowing and band alignment in InGaN alloys,” Applied Physics Letters, vol. 96, no. 2, pp. 021908-1-021908-3, 2010.

[121] Z. Hongping, R. A. Arif, Y. K. Ee, and N. Tansu, “Self-consistent analysis of strain-compensated InGaN-AlGaN quantum wells for lasers and light-emitting diodes,” Quantum Electronics, IEEE Journal of, vol. 45, no. 1, pp. 66-78, 2009.

[122] C. Tablero, “Electronic and magnetic properties of ZnS doped with Cr,” Physical Review B, vol. 74, no. 19, pp. 195203-1-195203-9, 2006.

[123] O. V. Koplak, A. I. Dmitriev, A. D. Talantsev, S. V. Zaitsev, and R. B. Morgunov, “Ferromagnetism of nanoclusters of chromium alloys and luminescence quenching in ZnSe/ZnMgSSe/ZnSSe: Cr heterostructures,” Physics of the Solid State, vol. 55, no. 9, pp. 1870-1877, 2013.

[124] S. P. Bremner, M. Y. Levy, and C. B. Honsberg, “Limiting efficiency of an intermediate band solar cell under a terrestrial spectrum,” Applied Physics Letters, vol. 92, no. 17, pp. 171110-1 - 171110-3, 2008.

[125] Q. Shao, A. A. Balandin, A. I. Fedoseyev, and M. Turowski, “Intermediate-band solar cells based on quantum dot superacrystals,” Applied Physics Letters, vol. 91, no. 16, pp. 163503-1 - 163503-3, 2007.

[126] V. Popescu, G. Bester, M. C. Hanna, A. G. Norman, and A. Zunger, “Theoretical and experimental examination of the intermediate-band concept for strain-balanced (In,Ga)As/Ga(As,P) quantum dot solar cells,” Physical Review B, vol. 78, no. 20, pp. 205321-1 - 205321-7, 2008.

[127] M. Y. Levy, C. Honsberg, A. Marti, and A. Luque, "Quantum dot intermediate band solar cell material systems with negligible valence band offsets." In Proc. of 31th Photovoltaic Specialists Conference, pp. 90-93, 2005.

[128] P. Wahnón, and C. Tablero, “*Ab initio* electronic structure calculations for metallic intermediate band formation in photovoltaic materials,” Physical Review B, vol. 65, no. 16, pp. 165115-1 - 165115-10, 2002.

[129] P. Palacios, P. Wahnón, S. Pizzinato, and J. C. Conesa, “Energetics of formation of TiGa3As4 and TiGa3P4 intermediate band materials,” The Journal of Chemical Physics, vol. 124, no. 1, pp. 014711-1–014711-5, 2006.

[130] P. Palacios, I. Aguilera, K. Sánchez, J. C. Conesa, and P. Wahnón, “Transition-metal-substituted indium thiospinels as novel intermediate-band materials: prediction and understanding of their electronic properties,” Physical Review Letters, vol. 101, no. 4, pp. 046403-1-046403-4, 2008.

[131] K. Sánchez, I. Aguilera, P. Palacios, and P. Wahnón, “Assessment through first-principles calculations of an intermediate-band photovoltaic material based on Ti-implanted silicon: Interstitial versus substitutional origin,” Physical Review B, vol. 79, no. 16, pp. 165203-1 - 165203-7, 2009.

[132] A. Luque, A. Martí, C. Stanley, N. López, L. Cuadra, D. Zhou, J. L. Pearson, and A. McKee, “General equivalent circuit for intermediate band devices: Potentials, currents and electroluminescence,” Journal of Applied Physics, vol. 96, no. 1, pp. 903-909, 2004.

[133] S. M. Hubbard, C. D. Cress, C. G. Bailey, R. P. Raffaelle, S. G. Bailey, and D. M. Wilt, “Effect of strain compensation on quantum dot enhanced GaAs solar cells,” Applied Physics Letters, vol. 92, no. 12, pp. 123512-1 - 123512-3, 2008.

[134] R. Oshima, A. Takata, and Y. Okada, “Strain-compensated InAs/GaNAs quantum dots for use in high-efficiency solar cells,” Applied Physics Letters, vol. 93, no. 8, pp. 083111-1 - 083111-3, 2008.

[135] C. G. Bailey, D. V. Forbes, R. P. Raffaelle, and S. M. Hubbard, “Near 1 V open circuit voltage InAs/GaAs quantum dot solar cells,” Applied Physics Letters, vol. 98, no. 16, pp. 163105-1 - 163105-3, 2011.

[136] A. Marti, E. Antolin, P. G. Linares, and A. Luque, “Understanding experimental characterization of intermediate band solar cells,” Journal of Materials Chemistry, vol. 22, no. 43, pp. 22832-22839, 2012.

[137] N. Ahsan, N. Miyashita, M. Monirul Islam, K. Man Yu, W. Walukiewicz, and Y. Okada, “Two-photon excitation in an intermediate band solar cell structure,” Applied Physics Letters, vol. 100, no. 17, pp. 172111-1 - 172111-4, 2012.

[138] A. Luque, A. Marti, and L. Cuadra, “Impact-ionization-assisted intermediate band solar cell,” Electron Devices, IEEE Transactions on, vol. 50, no. 2, pp. 447-454, 2003.

[139] M. Ley, J. Boudaden, and Z. T. Kuznicki, “Thermodynamic efficiency of an intermediate band photovoltaic cell with low threshold Auger generation,” Journal of Applied Physics, vol. 98, no. 4, pp. 044905-1 - 044905-5, 2005.

[140] A. Luque, P. G. Linares, E. Antolín, E. Cánovas, C. D. Farmer, C. R. Stanley, and A. Martí, “Multiple levels in intermediate band solar cells,” Applied Physics Letters, vol. 96, no. 1, pp. 013501-1 - 013501-3, 2010.

[141] T. S. Navruz, and M. Saritas, “The detailed analysis of auger effect on the efficiency of intermediate band solar cells,” Solar Energy Materials and Solar Cells, vol. 93, no. 11, pp. 1913-1922, 2009.

[142] A. S. Brown, M. A. Green, and R. P. Corkish, “Limiting efficiency for a multi-band solar cell containing three and four bands,” Physica E: Low-dimensional Systems and Nanostructures, vol. 14, no. 1–2, pp. 121-125, 2002.

[143] M. A. Green, “Multiple band and impurity photovoltaic solar cells: General theory and comparison to tandem cells,” Progress in Photovoltaics: Research and Applications, vol. 9, no. 2, pp. 137-144, 2001.

[144] T. Nozawa, and Y. Arakawa, “Detailed balance limit of the efficiency of multilevel intermediate band solar cells,” Applied Physics Letters, vol. 98, no. 17, pp. 171108-1 - 171108-2, 2011.

[145] M.A Green, Third Generation Photovoltaics: Ultra-High Efficiency at Low Cost (Springer-Verlag, Berlin, 2003)

[146] G. Conibeer, “Third-generation photovoltaics,” Materials Today, vol. 10, no. 11, pp. 42-50, 2007.

[147] A. Polman, and H. A. Atwater, “Photonic design principles for ultrahigh-efficiency photovoltaics,” Nature Materials, vol. 11, no. 3, pp. 174-177, 2012.

[148] M. C. Hoffmann, J. Hebling, H. Y. Hwang, K. Yeh, and K. A. Nelson, “ Impact ionization in InSb probed by THz-pump THz-probe spectroscopy”, Phys. Rev. B. vol. 79, pp. 161201-1-161201-4 , 2009.

[149] H. Hirori, K. Shinokita, M. Shirai, S. Tani, Y. Kadoya, and K. Tanaka, "Extraordinary carrier multiplication in GaAs MQWs induced by intense terahertz pulse." pp. 1-2. Infrared, Millimeter and Terahertz Waves (IRMMW-THz), 2011 36th International Conference on

[150] H. Hirori, K. Shinokita, M. Shirai, S. Tani, Y. Kadoya, and K. Tanaka, “Extraordinary carrier multiplication gated by a picosecond electric field pulse,” Nature Communication, vol. 2, pp. 594-1-594-7, 2011.

APPENDIX A

COPYRIGHT OF CHAPTER 1

A.1. Public domain and use of EIA content for reference [1] and [2]

U.S. Government publications are in the public domain and are not subject to copyright protection. You may use and/or distribute any of our data, files, databases, reports, graphs, charts, and other information products that are on our website or that you receive through our email distribution service. However, if you use or reproduce any of our information products, you should use an acknowledgment, which includes the publication date, such as: "Source: U.S. Energy Information Administration (Oct 2008)."

A.2. The copyright from National Renewable Energy Laboratory (NREL) for Fig. 1.3

The chart "Best Research-Cell Efficiencies" is reprinted with permission by the National Renewable Energy Laboratory, http://www.nrel.gov/ncpv/images/efficiency_chart.jpg, Accessed March 14, 2014.

The NREL developed chart is not to be used to imply an endorsement by NREL, the Alliance for Sustainable Energy, LLC, the operator of NREL, or the U.S. Department of Energy.

APPENDIX B

COPYRIGHT OF IEEE IN CHAPTER 2, 4, 5

In reference to IEEE copyrighted material which is used with permission in this thesis, the IEEE does not endorse any of Arizona State University's products or services. Internal or personal use of this material is permitted. If interested in reprinting/republishing IEEE copyrighted material for advertising or promotional purposes or for creating new collective works for resale or redistribution, please go to http://www.ieee.org/publications_standards/publications/rights/rights_link.html to learn how to obtain a License from RightsLink.

The copy right format of IEEE is © [Year IEEE] and Citation

APPENDIX C

THE QUANTUM YIELD OF MJMEG SOLAR CELL

In chapter 4, the author briefly introduces the quantum yield variations for 4 junction MJMEG solar cells. In this section, the author would like to explain it in detail. First, in Figs. C.1 (a), (b), and (c), the author considers the QY distributions for the cases of two, three, and four junctions. For the two junction case (Fig. C.1 (a)), considering just the bottom two junctions (E_{g1} is 0.31eV and E_{g2}=0.93 eV) of the previous 4J case as a double junction MJMEG cell, there is no overlap of QY and for a part of the spectrum, the QY of each junction is 2 (see Fig. C.1(a)) which there is enough “room” in the spectrum for MEG to occur in both junctions.

Including the third layer (E_{g3}=1.86 eV) as a triple junction cell, the possible QY for the middle junction(E_{g2}) of MJMEG is only 1 and QYs for bottom and top most junctions (E_{g1}, E_{g3}) is again 2 for a portion of the spectrum (see Fig.C.1 (b)). The threshold energy of the middle junction bandgap(=0.93 eV) at two times its bandgap (=1.86 eV) is the same as the bandgap of the top junction. Thus the maximum QY of the middle cell overlaps the top junction cell and for these band gaps, the middle solar cell does not have MEG generation and behaves as a conventional MJ cell, even if the MEG process where to theoretically be able to occur in the material.

Finally, for the full 4 junction MJMEG solar cell including E_{g4} (=2.79 eV), the QYs of the second (=0.93 eV) and third (=1.86 eV) junction are 1 and the QYs in the bottom (=0.31 eV) and top (=2.79 eV) most junctions are 2 for a part of the spectrum (see Figure C.1(c)). The 2nd and 3rd junctions behave as conventional MJ junctions. The effect of the increased QY in the high photon energy region at the top junction is negligible due to the small amount of solar photon current therein.

Overall, the MEG effect of the top most junction in the MJMEG is nearly the same as in conventional MJ solar cells with increasing number of junctions. For instance, if the bandgap of the top junction is 2.79 eV and, the threshold energy for MEG is 5.58 eV where the photon flux in this region is nearly zero.

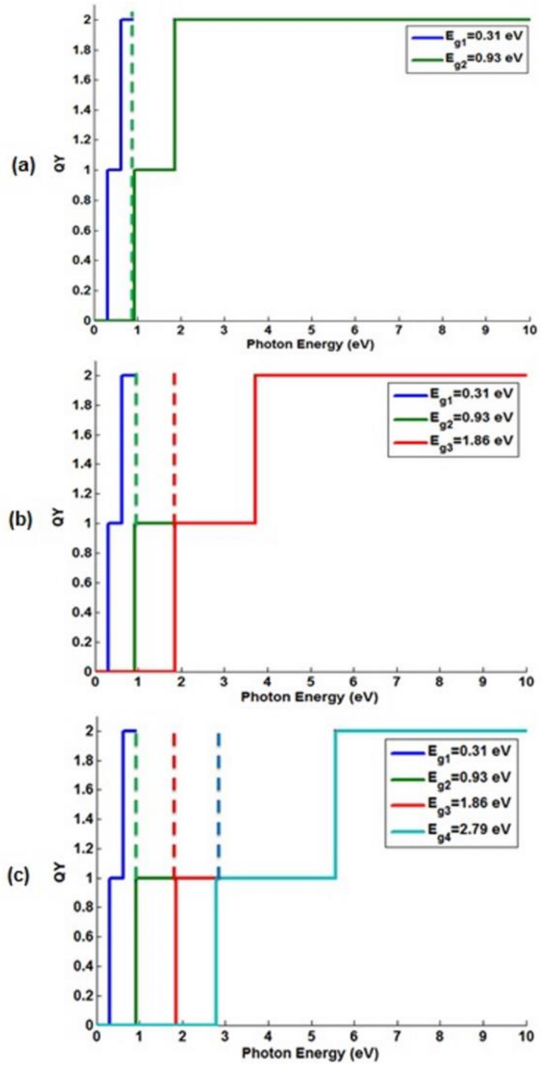

Fig. C.1. The QY distributions of MJMEG solar cells. With increasing number of junction, the bottom most and top most junction will have the highest possibility of MEG effect. But, the MEG effect of top most junction will be negligible due to low amount of solar photon flux at high photon energy region with increasing number of junction. (a) is the double junction MJMEG, (b) is the triple junction MJMEG and (c) is the four junction MJMEG solar cells

Based on this, the number of junctions for MJMEG solar cells is restrained because of the limitation of maximum QY and amount of photon energy of each junction through dividing photon energy region. To take advantage of MEG within each cell, the threshold of photon energy is two times greater than the lower photon energy ($E_{g2}>2E_{g1}$) assuming two EHPs per one photon. Otherwise, the MEG effect will not occur and the generated carriers in each cell will be one. However, with increasing photon energy and number of junctions, there are difficulties achieving the MEG effect within each junction. In other words, QY of mid-junctions in MJMEG solar cells will have QY=1e if the spectral region is narrow. Thus, it is important to consider the relationship between the number of EHPs and junctions. As shown in the example above, the bottom junction and top cell in MJMEG have the highest possibilities for benefiting from MEG and middle cells may or may not experience the MEG effect. Therefore, the choice of spectral splitting for MJMEG cells is important in order to give a reasonable range of solar spectrum of each junction and result in the maximum efficiency and optimized bandgaps.

APPENDIX D

COPYRIGHT OF CHAPTER 6

The copyright of chapter 4 is endorsed by Mr. Christopher Green (Lock Heaven University), Dr. Stephen Goodnick (Arizona State University) and Ms. Melanie-Claire Mallison (N-REU Program Assistant)

1. Christopher Green

“You have my permission to use any of the results of my research in your doctoral thesis. Hope everything is going well.

Good luck on your thesis

Chris”

2. Dr. Stephen Goodnick in Arizona State University

“It is okay to reproduce as long as Chris Green’s contribution is appropriately acknowledged”

3. Melanie-Claire Mallison in N-REU Program Assistant

“As long as you acknowledge Christopher and the 2013 NNIN REU Program in your paper, you are free to use whatever research results you wish. If you use an actual graph or image that Christopher took, then of course that image needs to be specifically credited to him in the caption. But essentially, the research Christopher performed belongs to Prof. Goodnick. So as I say, as long as Christopher and the program are properly acknowledged, the research and results are yours to discuss.

Melanie-Claire”

APPENDIX E

COPYRIGHT OF SPIE IN CHAPTER 7

As author, SPIE shares the copyright with you, so you retain the right to reproduce your paper in part or in whole.

Publisher's permission is hereby granted under the following conditions:

(1) the material to be used has appeared in our publication without credit or acknowledgment to another source; and

(2) you credit the original SPIE publication. Include the authors' names, title of paper, volume title, SPIE volume number, and year of publication in your credit statement. “Jongwon Lee and Christiana B. Honsberg, “The thermodynamic limits of tandem photovoltaic devices with intermediate band,” Physics, Simulation, and Photonic Engineering of Photovoltaic Devices, Physics, Simulation, and Photonic Engineering of Photovoltaic Devices, Alexandre Freundlich; Jean-Francois F. Guillemoles, Proc. SPIE 8256, 82560Q (February 9, 2012); doi:10.1117/12.910813.”

Copyright 2012 Society of Photo Optical Instrumentation Engineers. One print or electronic copy may be made for personal use only. Systematic electronic or print reproduction and distribution, duplication of any material in this paper for a fee or for commercial purposes, or modification of the content of the paper are prohibited.